THE ROLE OF MAGMATISM IN THE EVOLUTION OF THE CAMBRIAN SOUTHERN OKLAHOMA RIFT ZONE: GEOCHEMICAL CONSTRAINTS ON THE MAFIC-INTERMEDIATE ROCKS IN THE ARBUCKLE MOUNTAINS, OK

by

CASEY L. BULEN

B.S., NORTHWEST MISSOURI STATE UNIVERSITY, 2010

A THESIS

submitted in partial fulfillment of the requirements for the degree

MASTER OF SCIENCE

Department of Geology
College of Arts and Sciences

KANSAS STATE UNIVERSITY
Manhattan, Kansas

2012

Approved by:

Major Professor
Matthew E. Brueseke

Abstract

The Southern Oklahoma rift zone (SOA), which stretches from southern Oklahoma through the Texas panhandle and into Colorado and New Mexico, contains extensive bimodal mafic-silicic magmatism related to the opening of the Iapetus Ocean during the late Precambrian and early Cambrian. Within the SOA, the subsurface in and adjacent to the Arbuckle Mountains in southern Oklahoma contains thick packages of mafic to intermediate lava flows interlayered with thick, extensive rhyolite lava flows and lesser silicic intrusive bodies, which were first described during a 1982 drill test (Hamilton Brothers Turner Falls well) in the region. Well cuttings of these units were collected from that well and three others (Pan-Am Williams D-2, Pan-Am Jarman, Pan-Am Newberry). This study is focused on these mafic-intermediate lava flows, which represent an important stage in the evolution of the SOA and provide insights into the formation and tectonomagmatic evolution of the rift zone. The estimated 210,000 km^3 of mafic rocks in the SOA were extruded as a result of the break-up of Pannotia and the formation of the failed arm of a three-armed radial rift system. Samples analyzed from the wells plot as basalts to andesites on the TAS diagram of Le Bas et al (1986) and as subalkaline-alkaline basalts to andesite-trachyandesites on the Zr/TiO_2 vs. Nb/Y diagram of Winchester and Floyd (1977). They are dominantly tholeiitic on multiple discrimination diagrams including those of Miyashiro (1974) and Irvine and Baragar (1971). The lava flows contain traits common with EMI OIB coupled with upper crustal contamination, such as Zr/Nb values ranging from 8 to 10, Ba/Nb values ranging from 10 to 20, and K/Nb values ranging from 300 to 600. Chemostratigraphic comparisons between each well reveal up to five lava flow packages within the larger mafic-intermediate sequence, at least in the vicinity of the sampled wells. When compared with intrusive mafic rocks outcropped in the Wichita Mountains, the SOA lava flows display geochemical traits most similar to those of the Roosevelt Gabbros, suggesting a possible co-genetic relationship. Overall, the whole rock chemical characteristics coupled with comparisons with other large igneous provinces (Columbia River and Oregon Plateaus, East African Rift System) indicate that the SOA lava flows are the result of flood basalt volcanism.

Table of Contents

List of Figures

List of Tables

Acknowledgements

Thanks to Dr. Matthew Brueseke, for his discussions and lessons in igneous petrology and geochemistry, funding and assistance for this project, and guidance for my current and future plans in geology. Dr. Saugata Datta and Dr. Sambhudas Chaudhuri, for lessons in geochemistry in the classroom and serving as committee members for my thesis. To the American Association of Petroleum Geologists, for providing funding for this project through the Barrett Family Named Grant. Dr. Richard Hanson at Texas Christian University, Bob Puckett of Oklahoma City, and Dr. Neil Suneson and Vyetta Jordan at the Oklahoma Geological Survey, for sharing their knowledge of Oklahoma geology and assisting with sample collection. Dr. Richard Hanson and Bob Puckett also facilitated the writing of the Lithos paper cited in this thesis. Dr. Stanley Mertzman at Franklin & Marshall College, for completing geochemical analyses on the samples and providing his insights into their results. Ashley Leger, Nathan and Kathryn Schmitz, Molly Ramsey, Kate Amrhein, and Andrea Leggett, for helping me discover and explore my love of geology and providing the best friendships a person can have, and also keeping me sane throughout this process. Finally, to my family and other close friends, for showing the love and support that only you can give. Thank you!

Chapter 1 - **Introduction**

The Laurentian subcontinent, which includes much of North America, was a component of two supercontinents, Rodinia and Pannotia (or Greater Gondwanaland), present throughout the Mid to Late Neoproterozoic (Scotese, 2009). The supercontinent of Rodinia was assembled between 1200-1050 Ma, containing Laurentia near its core (Scotese, 2009). Following its completion, Rodinia remained intact for near 300 million years. Around 800 Ma, Rodinia split into two large continents, North Rodinia and South Rodinia (Scotese, 2009).

Following the break-up of the Rodinian supercontinent, North Rodinia and South Rodinia collided over a 100 Ma time period with the Congo to form the core of Pannotia (Scotese, 2009). The assembly of Pannotia repositioned Laurentia in the southeastern portion of the supercontinent. Pannotia was a relatively short-lived supercontinent, lasting only about 30 million years (Scotese, 2009). By the Late Precambrian (560 Ma), Pannotia was rifted into four separate continents. Laurentia and Baltica rifted away from Pannotia to form the Iatepus Ocean and Tornquist Sea during the Late Precambrian and Early Cambrian (Scotese, 2009). The Siberian continent also rifted away from Pannotia during the Early Cambrian, leaving behind the core of the supercontinent, Gondwana (Scotese, 2009).

These rifting events were accompanied by intraplate magmatism along the eastern margin of the Laurentian craton. The only evidence of these events along the southeastern margin of Laurentia is in southern Oklahoma and northern Texas as part of the Southern Oklahoma rift zone (Hanson et al, 2012). The rift zone (Figure 1) contains extensive bimodal (basalt-rhyolite) igneous rocks that are exposed in the Wichita and in the subsurface near the Arbuckle Mountains of southern Oklahoma. These exposures represent the largest magmatic episodes related to the opening of the Iapetus Ocean and the break-up of Pannotia.

Thomas (2011) proposed an alternative hypothesis for the origin of the Southern Oklahoma rift zone. The similar trend of the Southern Oklahoma rift zone with the Alabama-Oklahoma transform and its intersection with the Ouachita thrust front is used to argue that the Southern Oklahoma rift zone may have formed as an intracratonic leaky transform fault system (Thomas, 2011). The geometry and composition of magmatism in the Southern Oklahoma rift zone indicates crust-penetrating near-vertical fractures as conduits for magma eruption, which is consistent with a leaky transform fault system. This system, according to Thomas (2006),

parallels a bend in the Grenville front, which also aligns with Precambrian mafic dikes present in the Arbuckle Mountains.

This research focuses on the subsurface mafic suite present in the Arbuckle Mountains and first described by Puckett (2011). Major and trace element geochemistry is used to better understand the character and significance of these lava flows, as well as provide a more constrained description of them. Chemostratigraphic variations are used to describe the vertical extent of lava flow packages present in three wells drilled in the area adjacent to the Arbuckle Mountains, which contain these mafic lava flows. Comparisons have also been made to other well-studied flood basalt provinces to better constrain the tectonomagmatic environment in which the mafic rocks in the Arbuckle Mountains were formed.

Regional Geology of Southern Oklahoma

The Southern Oklahoma rift zone stretches over 500 kilometers along a northwest trend into the Laurentian craton from the Ouachita thrust front in southeastern Oklahoma through the Texas panhandle, New Mexico and Colorado into Utah (Powell and Phelps, 1977; Larson et al, 1985; Thomas, 2011). The rift zone has been described as the failed arm of a three-armed radial rift system, with the remaining arms extending into the Iapetus Ocean. The Southern Oklahoma rift zone began as a graben underlain by Precambrian granitic rocks (Hoffman et al, 1974).

Geophysical evidence also supports the hypothesis that the Southern Oklahoma rift zone represents the failed arm of a three-armed radial rift system formed during the break-up of the supercontinent Pannotia. Large linear gravity anomalies depict rift structures stretching from the Ouachita orogenic belt in southeastern Oklahoma across the southern portion of the state and into the panhandle of Texas (Keller and Stephenson, 2007; Hanson et al, 2012). Keller and Stephenson (2007) estimated that the Southern Oklahoma rift zone extends at least 1,000 km from the Ouachita orogenic belt in the Laurentian craton and may be as wide as 150 km. The rift zone also extends to a depth of at least 10 km (Keller and Stephenson, 2007; Hanson et al, 2012). Many locations throughout the rift zone contain anomalies that exceed 100 mGal, caused by the presence of extensive mafic volcanism in the subsurface (Keller and Stephenson, 2007).

Rifting in Southern Oklahoma began with the extrusion of a mafic layered complex, known as the Glen Mountains Layered Complex at ~577 Ma that crops out in the Wichita Mountains. This complex extends over 1,000 km^2 and is 3-5 km thick. It consists of anorthositic

gabbros and troctolites (Scofield, 1975; McConnell and Gilbert, 1990). The Glen Mountains Layered Complex was intruded by a series of gabbroic plutons at ~ 552 Ma, known collectively as the Roosevelt Gabbros (Sandy Creek, Glen Creek, Mount Sheridan, and Mount Scott). The Roosevelt Gabbros consists of hydrous, olivine tholeiite that differentiated from a separate magma than the Glen Mountains Layered Complex, which is anhydrous and composed of alumina-rich tholeiites (Cameron et al, 1986; McConnell and Gilbert, 1990).

Following the intrusion of the Roosevelt Gabbros, erosion occurred on the surface of the region during a period of extended exposure. This erosional surface was covered by the eruption of extensive subalkaline rhyolitic lava flows and ash-flow tuffs, known as the Carlton Rhyolite that occurred concurrently with the intrusion of a series of granitic sills, referred to as the Wichita Granite Group at 500-525 Ma. The Carlton Rhyolite covers an area of 40,000 km^2 in the subsurface and is at least 1.4 km thick (Keller and Stephenson, 2007). The eruption of the Carlton Rhyolite was controlled by the presence of faults in the region (Meers fault in the Wichita Mountains and the Washita Valley fault in the Arbuckle Mountains); these units have erupted along linear fissures related to the faults (Ham et al, 1965; Hanson and Al-Shaieb, 1980; McConnell and Gilbert, 1990). The Wichita Granite Group contains a series of granites that show an increase in alkalinity from older subalkaline granites (Mount Scott Granite) to younger peralkaline granites (Quanah Granite). These silicic magmas were likely formed from the differentiation of a large mass of basaltic magma underlying the rift zone or partial melting of continental crust (Hanson and Al-Shaieb, 1980; Cameron et al, 1986).

The subsurface in the Wichita Mountain region also contains basalt and altered basalt a few hundred meters thick, referred to as the Navajoe Mountain Basalt-Spilite Group. These may represent the extrusive equivalent of the Mount Sheridan Gabbro. They represent an earlier phase of magmatism than the Carlton Rhyolite and Wichita Granites (Hanson and Al-Shaieb, 1980; Cameron et al, 1986).

The final phases of volcanism in the Wichita Mountains are represented by a regional swarm of mafic dikes. These dikes are composed of microgabbro, microdiorite, basalt, and diabase, and have been collectively referred to as the Late Diabase Dikes. They also appear to be related to a small body of gabbro, known as the Kimbell Gabbro, which is located north of the main portion of the Wichita Mountains. They exhibit tholeiitic to transitional geochemical

affinities and display geochemical traits that represent an intraplate extensional environment (Gilbert and Hughes, 1986; McConnell and Gilbert, 1990; DeGroat et al, 1995).

Following the conclusion of Cambrian magmatism, the Southern Oklahoma rift zone experienced a period of regional subsidence to form deep basins accompanied by the deposition of Paleozoic sediments. From the remainder of the Cambrian through the Devonian, sedimentation was restricted to carbonates deposited along continental margins. This was followed by Carboniferous to Permian deposition of clastic sediments. The region was compressed in the Late Paleozoic and truncated by a series of faults (Ham et al, 1965; Hoffman et al, 1974).

The presence of Cambrian igneous rocks in the Southern Oklahoma rift zone was a major control on the future geology of the region. These rocks and the rift setting influenced the depth and location of future sedimentation in the region, as well as the magnitude and intensity of deformation that would occur during Pennsylvanian orogenies in the region (Ham et al, 1965). Cambrian magmatism provided a heat source that weakened the crust causing extension to occur, which coupled with subsequent faulting, became the site of Pennsylvanian deformation (Powell and Phelps, 1977; McConnell and Gilbert, 1990). This deformation and sedimentation created deep basins (e.g., Anadarko Basin) that became the site of major petroleum accumulations that have made southern Oklahoma one of the most important petroleum-producing regions in North America, as well as the Arbuckle Mountains.

Local Geology of the Arbuckle Mountains

While the geology of the Wichita Mountains is well-constrained, the geology of the Arbuckle Mountains during the Cambrian is less understood, due to lack of surficial exposures of volcanic and plutonic rocks in the region. The Eastern Arbuckle Province is characterized by the presence of four units of Precambrian rocks that are 1300-1400 Ma (Bickford and Lewis, 1979). These units were likely the basement that the Southern Oklahoma rift zone formed in, during the Early Cambrian in the Arbuckle Mountains region. These units are cut by mafic dikes from two time periods. Older Precambrian dikes in the region are near the age of the host granitic rocks (~1300-1400 Ma) and indicate a zone and direction of weakness trending N 60° W, which was reactivated in the Cambrian, during the opening of the Southern Oklahoma rift zone. The opening of the Southern Oklahoma rift zone was accompanied by the intrusion of a second set of

dike swarms that cut through the granitic rocks in the Arbuckle Mountains (Denison, 1995). These dikes are the only surficial exposures of mafic rocks in the Arbuckle Mountains.

The Western Arbuckle Mountains contain surficial exposures of the Carlton Rhyolite, which represent the latest major phase of volcanism in the region (Hanson et al, 2012). While these exposures are limited, they provide additional evidence for the extent of the Carlton Rhyolite throughout the Southern Oklahoma rift zone.

Recently, Puckett (2011) completed petrographic analyses on extensive mafic lava flows present in the subsurface of the Western Arbuckle Mountains. These mafic lava flows were first described in the Hamilton Brothers #1-18 Turner Falls test well drilled in 1981-1982, to a depth of 18,500 feet (Figure 2). The Turner Falls test revealed a suite of igneous rocks present in the subsurface of the Arbuckle Mountains. Previous appearances of mafic rocks in the subsurface were believed to be dikes and sills based on the apparent thickness of those units. However, the mafic rocks revealed in the Turner Falls well exhibited a total apparent thickness of 9,740 feet, intercalated with granitic sills (Puckett, 2011; Hanson et al, 2012). Significant evidence of extensive mafic lava flows in the Arbuckle Mountains is present in other wells drilled in the region. Recent estimates suggest that mafic rocks present at depth throughout the Southern Oklahoma rift zone may exceed 210,000 km^3 (Hanson et al, 2012).

The mafic lava flows were described by Puckett (2011), and later examined in a preliminary manner by Hanson et al (2012), as dominantly basalt to andesite with a varying range of textures. These textures include glassy with small phenocrysts and trachytic texture, ranging to coarsely porphyritic with larger plagioclase crystals. These rocks are partially altered, based on petrographic examination, throughout the well through multiple processes, including sericitization, carbonate replacement of plagioclase, chloritization of matrix minerals, and epidotization of mafic minerals. Primary minerals present within the basalts include olivine, augite and <15% opaque minerals, which are mainly magnetite. Puckett (2011) used gamma ray logs as an indicator of the appearance and thickness of separate lava flows. These lava flows are, on average, 30-40 feet thick with a maximum thickness of 50 feet.

Note: The term ‘mafic’ is used in this thesis to describe the well cuttings analyzed in the context of their visual appearance, which appear to be mafic in composition, not to describe their

geochemical traits, which classifies these samples as mafic to intermediate in composition (as discussed later).

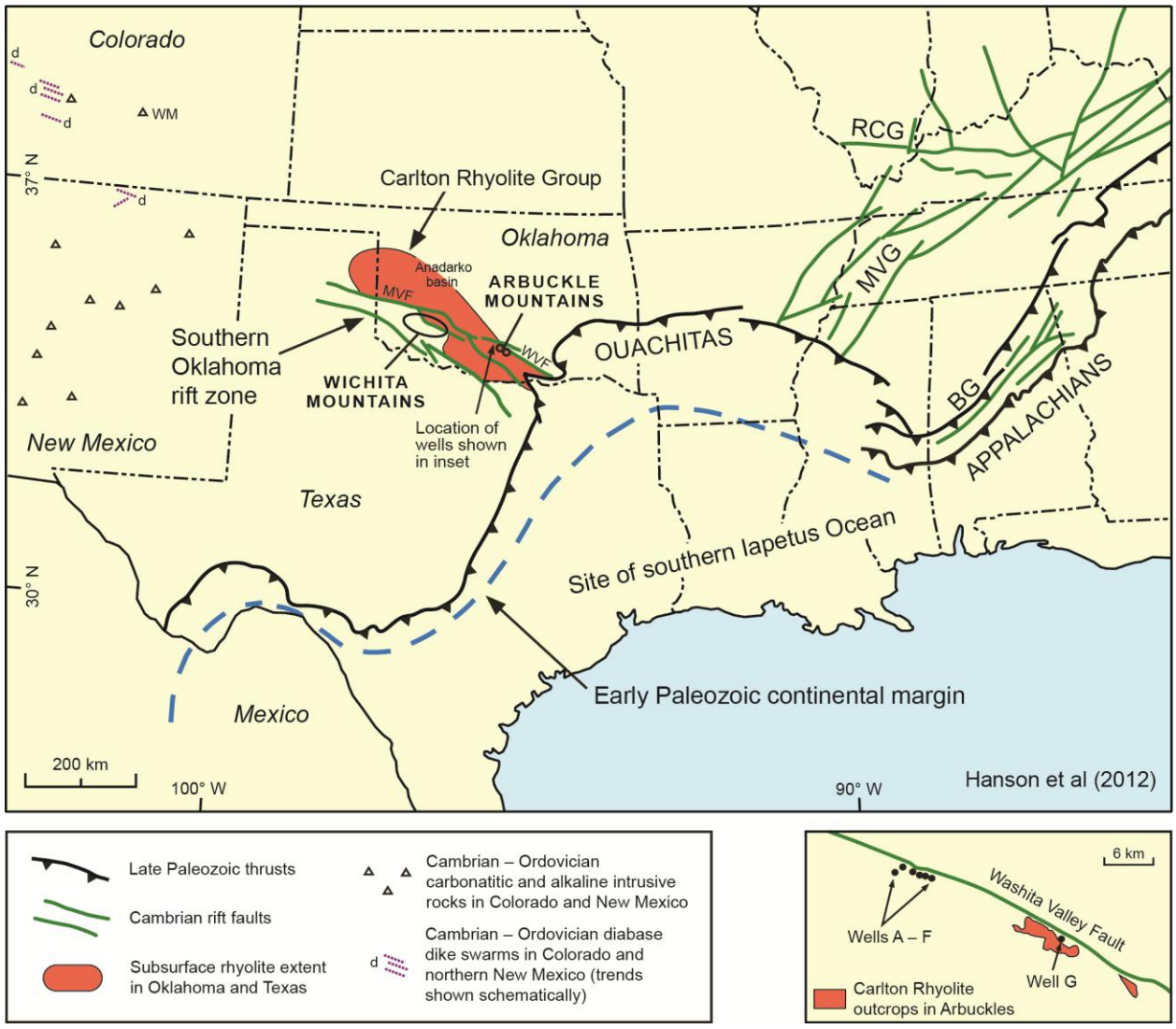

Figure 1: Map of Southern Oklahoma rift zone after Hanson et al (2012). The approximate location of igneous rocks present in the Wichita and Arbuckle Mountains are indicated. The inset displays the four wells mentioned in this study, along with wells discussed in Hanson et al (2012). Well A: Pan-Am Newberry; Well C: Pan-Am Jarman; Well E: Pan-Am Williams; Well G: Turner Falls. Adapted from Hanson et al (2012). WM: Wet Mountains; MVF: Mountain View Fault; WVF: Washita Valley Fault; BG: Birmingham graben; MCG: Mississippi Valley graben; RCG: Rough Creek graben.

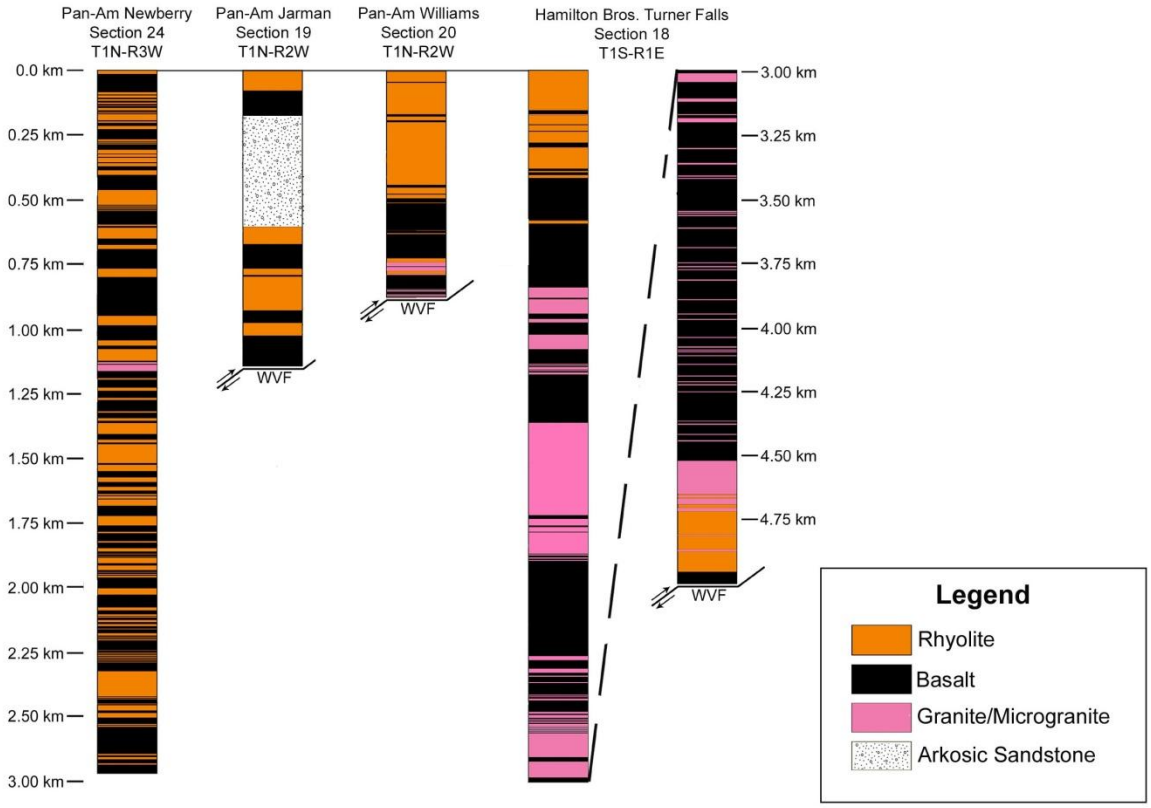

Figure 2: Lithologic well logs of igneous – sedimentary stratigraphy in the Southern Oklahoma rift zone adapted from Hanson et al (2012).

Chapter 2 - **Methods**

To better understand the geologic significance of the subsurface mafic rocks, samples of well cuttings were collected from four wells in the Western Arbuckle Mountains region (Pan-Am Williams D-2, Pan-Am Jarman 1-19, Pan-Am Newberry 1, and Hamilton Brothers 1A-18 Turner Falls). These four wells were chosen based on the apparent thickness of mafic rocks drilled into and the availability of well cuttings to sample. Figure 3 shows the location of the four wells that samples were collected from, superimposed on the Arbuckle Mountains Geologic Map published by the Oklahoma Geological Survey (Ham and McKinley, 1954; Puckett, unpublished figure). Samples were collected from the sample library at the Oklahoma Petroleum Information Center, managed by the Oklahoma Geological Survey in Norman, Oklahoma. Well cuttings weighing approximately 20 g total were collected from ~15 m intervals within each of the wells. These cuttings were an average of 2.5 mm in diameter, ranging from one to ten mm in diameter. Sample collection was limited to intervals that contained predominantly mafic material in hand sample or under a binocular microscope. To minimize contamination from other units located above each interval, samples were collected at least 300 m below the upper contact of the mafic sequence. In total, 76 samples were collected from the wells (21 samples from the Williams, 17 samples from the Jarman, 23 samples from the Newberry, and 15 samples from the Turner Falls). Samples from the Turner Falls well were not analyzed and will not be discussed further, due to: (1) difficulty with small grain sizes and (2) the profound contamination (e.g. heterogeneous nature of the cuttings) present from other lithologies within the cuttings.

Samples were prepared at Kansas State University for major and trace element analysis by x-ray fluorescence (XRF) spectroscopy. The bulk sample was handpicked using a research grade binocular microscope to remove any zeolite/carbonate minerals, foreign rock, and/or altered rock cuttings. Handpicking occurred to ensure samples processed further were 100% mafic rock fragments, thus granitoid and rhyolite clasts that were present in the collected bulk samples were removed, as were zeolite and carbonate minerals, which appeared clear under the binocular microscope. Rock cuttings that appeared to have a predominantly greenish tint, indicating a high level of propylitic alteration, were also removed.

After separation, samples containing more than 10 g of rock cuttings were crushed to a clay size (<200 mesh-sieve size) fraction in a Spex Industries aluminum oxide shatterbox.

Appendix A shows the 48 samples that were analyzed, along with the collected and analyzed weights (in grams) of the samples and the depth interval that each sample was collected from.

Samples were sent to Franklin and Marshall College for XRF spectroscopy to obtain major and trace element compositions and loss on ignition (LOI) values. Samples were analyzed following the method outlined in Mertzman (2000) and online at Mertzman (2012).

One-gram aliquots of rock powder were weighted to four decimal precision and placed in clean ceramic crucibles and put in a nine sample wire basket, which were heated at 900° C for one to one and a quarter hours in a muffle furnace. The samples cooled to room temperature in large desiccators and were reweighed. The percentage change was reported as loss on ignition. Following LOI determination, 0.4000 grams of powder was mixed with 3.6000 grams of lithium tetraborate ($Li_2B_4O_7$) and melted in 95% Pt-5% Au crucibles. This melt was quenched into homogeneous glass disks used for XRF analysis of major elements. Major elements were analyzed using a Panalytical, Inc. 2404 XRF vacuum spectrometer equipped with a 4 kW Rh x-ray tube. Major elements (SiO_2, Al_2O_3, CaO, K_2O, P_2O_5, TiO_2, Fe_2O_3, MnO, Na_2O, and MgO) are presented as weight percent oxide. Nineteen trace elements (Rb, Sr, Y, Zr, Nb, Ni, Ga, Cu, Zn, U, Th, Co, Pb, Sc, Cr, V, La, Ce, and Ba) were analyzed using the same XRF instrumentation used for major elements. A mixture of 7.000 g of whole-rock sample powder and 1.4000 grams of high purity Copolywax powder (a binding agent) was used to create pressed powder briquettes for XRF analysis of trace elements. Trace element concentrations are presented as parts per million (ppm).

Alteration

As mentioned, some samples of mafic well cuttings from the Arbuckle Mountains were visibly altered in hand sample. Puckett (2011) reported that the samples encountered in the Turner Falls well were partially altered through multiple processes, including sericitization, carbonate replacement of plagioclase, chloritization of matrix minerals, and epidotization of mafic minerals. This is true of samples in the three wells analyzed in this study. While cuttings that displayed visible alteration under a binocular microscope were removed from the samples prior to analysis, it is possible that this alteration still affected the analyses. This would decrease the accuracy of interpretations utilizing compatible major and trace elements. For this reason,

this thesis has looked to utilize incompatible major and trace element data to support the interpretations utilizing compatible major and trace element data.

Beswick and Soucie (1978) proposed an "alteration filter" that could be used to determine the extent of alteration that an igneous rock sample had undergone significant alteration, such that the alteration would affect the interpretation of geochemical data. This "alteration filter" plots molecular proportions of major element ratios (Al_2O_3/K_2O, SiO_2/K_2O, CaO/K_2O, etc.) on a logarithmic XY-plot (Beswick and Soucie, 1978). When plotted on a logarithmic scale, unaltered samples will appear clustered in linear array. Any significant variation from this linear array is indicative of post-eruptive alteration present in the samples. Samples from the Arbuckle Mountains exhibit some low-grade metamorphism, although many of the cuttings still exhibit primary mineral compositions and textures. Due to this, samples from the Arbuckle Mountains were run through the "alteration filter" of Beswick and Soucie (1978). Well cuttings from the Arbuckle Mountains indicate that the concentrations of Al_2O_3, Na_2O, P_2O_5, Rb, Ba, and Cu are the most mobile elements in the system. Typically, concentrations of MgO, CaO, K_2O, and Sr are also mobile elements during low-grade metamorphism (Walker et al, 2002). Therefore, geochemical interpretations using these elements should be used cautiously. These interpretations are supported in this research with diagrams or interpretations that utilize immobile major and trace elements. Arbuckle samples plotted as linear arrays with minimal variation, indicating that minimal alteration was present in the analyzed samples in which visibly altered cuttings were removed.

One sample (CB-PAJ-17) did not lie near the linear array on multiple versions of these plots (Figure 27 in Appendix E). This sample has been classified as 'significantly altered' via low-grade metamorphism. This sample was removed from the final interpretations presented in this research.

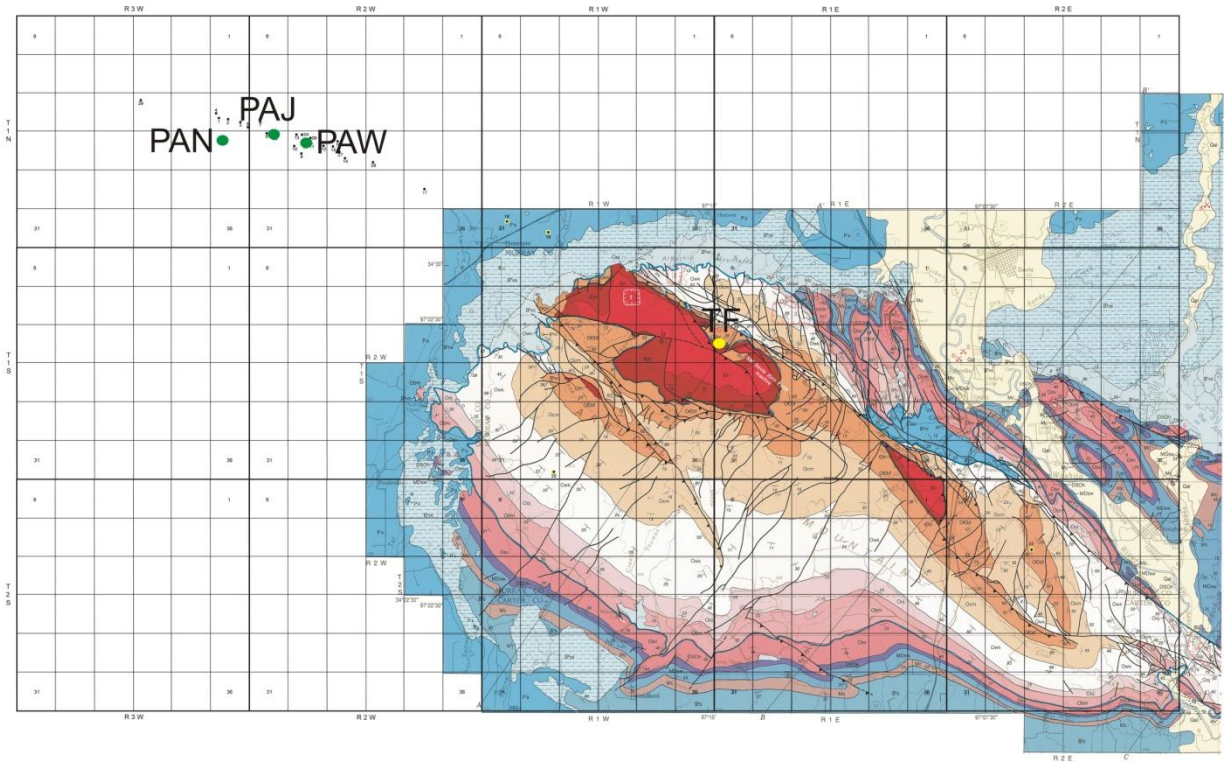

Figure 3: Geologic map of Arbuckle Mountains in southeastern Oklahoma (after Ham and McKinley, 1954; Puckett, unpublished figure). The location of three wells analyzed in this study (Williams, Newberry, and Jarman) is indicated by the green dots, while the location of the Turner Falls well is indicated by the yellow dot. Red unit is the Carlton Rhyolite, while the adjacent dark red unit is the Cambrian Timbered Hills group (containing the Reagan Sandstone overlain by Honey Creek Formation) that overlies the Carlton Rhyolite.

Chapter 3 - **Geochemical and Normative Mineralogical Results**

Major and trace element geochemical data was obtained on 48 samples of subsurface mafic rocks from three wells present in the Arbuckle Mountains of southern Oklahoma. Major element data is reported in weight percent (wt. %) oxide and trace element data is reported as parts per million (ppm). Complete major and trace element data is found in Appendix B. The complete normative mineralogy for each analyzed sample is found in Appendix C, expressed as weight percent norm. Representative samples are found in Table 1.

Geochemical Classification and Normative Mineralogy

On the total alkalis versus silica diagram of Le Bas et al (1986), the subsurface mafic rocks plot as basalts to andesites, with SiO_2 values ranging from 46.2 to 60.0 wt. % (Figure 4). The samples lie along a positive linear trend with increasing alkali contents as silica content increases and are subalkaline to slightly transitional.

The Zr/TiO_2 versus Nb/Y diagram utilized by Winchester and Floyd (1977) to classify igneous rocks is shown in Figure 5. Samples for the Arbuckle plot as subalkaline-alkaline basalts to andesite-trachyandesites. This supports the interpretation gained from the total alkalis versus silica diagram of Le Bas et al (1986) and also indicates that the bulk chemistry of the rocks have not been that affected by post-emplacement alteration.

The well cuttings plot as dominantly tholeiitic on the FeO*/MgO versus silica discrimination diagram used by Miyashiro (1974; shown in Figure 6). Some of the samples cluster around each other, and these are from similar or subsequent depths below the surface. This interpretation is also supported on the AFM diagram (Irvine and Baragar, 1971) with the majority of samples plotting in the tholeiite field (Figure 7). Discrimination diagrams utilizing immobile trace elements to describe the samples consistently depict them as tholeiites, again supporting the major element data. Figure 8 illustrates the well cuttings on the Nb/Y versus $Zr/(P_2O_5 \times 10^4)$ diagram used by Floyd and Winchester (1975). This diagram indicates the well cuttings are tholeiitic.

Samples contain the highest values of normative plagioclase and normative pyroxene. Normative anorthite ranges from ~8.9 to 26.4 wt. %, while normative albite ranges from ~21.6 to 42.3 wt. %. Normative hypersthene varies from ~7.8 to 17.3 wt. % and normative diopside varies

from ~2.0 to 22.3 wt. %. Values range from ~0.0 to 3.2 wt. %, and ~0.7 to 1.5 wt. % for normative olivine and normative apatite, respectively and most samples contain no normative olivine. Normative leucite and normative nepheline are absent from all of the samples, consistent with their subalkaline bulk chemistry.

The remaining normative mineral values are low to moderate. Normative quartz ranges from ~0.0 to 17.9 wt. %, while normative orthoclase values range from ~4.1 to 16.7 wt. %. Samples also contain ~6.4 to 8.9 wt. % normative magnetite and ~3.1 to 7.4 wt. % normative ilmenite.

Figure 9 shows the Ne'-Ol'-Q' diagram used by Irvine and Barager (1971). This diagram uses normative mineral values of olivine, nepheline, and quartz to distinguish between different basalt types. Analyzed samples plot in the subalkaline fields in regions common for tholeiitic basalts and olivine tholeiites.

Major and Trace Element Geochemical Characteristics

Harker diagrams for the major elements plotted versus SiO_2 are depicted in Figure 10. The data is plotted as weight percent major oxide for each major element and silica. Each of these diagrams shows linear arrays for the major elements in comparison to silica. Negative linear arrays exist when comparing Al_2O_3, FeO*, MgO, TiO_2, and CaO with silica. Alumina concentrations range from ~12.5 to 14.5 wt. %. FeO concentrations range from ~5.2 to 9.5 wt. %, while Fe_2O_3 concentrations range from ~4.4 to 6.0 wt. %. CaO and MgO values range from ~4.0 to 10.4 wt. % and ~2.2 to 6.4 wt. %, respectively. TiO_2 concentrations range from ~1.6 to 3.8 wt. %. K_2O and Na_2O concentrations show an increase with increasing SiO_2, while P_2O_5 shows an invariable relationship with silica. Total alkali values (Na_2O and K_2O) range from ~2.5 to 5.0 wt. % for Na_2O and ~0.7 to 2.8 wt. % for K_2O. P_2O_5 concentrations range from ~0.3 to 0.7 wt. %.

In general, samples from the Newberry well contain the lowest concentrations of silica, while samples from the Jarman well contain the highest concentrations of silica. Samples from the Williams well contain silica concentrations that overlap both the Jarman and Newberry well samples.

Trace element concentrations are plotted against wt. % SiO_2 in Figures 11 and 12. Trace element data plotted on these diagrams is presented in parts per million.

The values of Ce, Y depict an increasing array with an increase in silica content in these samples, while the values of Co, Cr, Cu, and V decrease with an increase in silica. Pb and Zn concentration increase slightly with increasing silica.

Arbuckle Mountain samples generally have Ni concentrations ranging from ~15 to 75 ppm. Nickel concentrations decrease with increasing silica. At least four groups of samples from subsequent depths in the Williams and Jarman wells form separate clusters on the Ni versus SiO_2 diagram in Figure 11. Scandium concentrations show similar relationships; decreasing with increasing silica and containing clusters with samples from subsequent depths. In general, these clusters occur with the same samples with similar nickel and scandium concentrations. Contents of scandium vary from ~21 to 45 ppm.

Positive relationships occur between silica and rubidium, barium, zirconium, and niobium. Concentrations range from ~12.1 to 52.3 ppm Rb, ~237 to 639 ppm Ba, ~117 to 431 ppm Zr, and ~16.1 to 42.1 ppm Nb. These diagrams also depict clusters of the concentrations, especially with samples from the Williams well. Zirconium and niobium exhibit the best clusters with samples from all three wells. These elements, along with Ba, also exhibit subparallel arrays between samples. Approximately three subparallel arrays are visible on the zirconium versus silica diagram, which appear to project back to the same Zr and SiO_2 concentrations. Similar trends appear on the niobium and barium versus silica diagrams, although they are most obvious on the zirconium versus silica diagram. Strontium concentrations range from ~170 to 439 ppm and show a negative relationship with silica.

Negative relationships exist between silica and cobalt, copper, chromium, and vanadium. Contents vary from ~38 to 57 ppm Co, ~34 to 210 ppm Cu, ~17 to 121 ppm Cr, and ~137 to 401 ppm V. Concentrations are more scattered for copper and chromium, especially at lower silica concentrations.

Cerium, lanthanum, and yttrium concentrations depict positive relationships with silica. These relationships are nearly linear for both cerium and yttrium, but appear slightly exponential for lanthanum. Minimal scatter is present on these three diagrams. Concentrations range from ~15 to 77 ppm Ce, ~24.7 to 55.8 ppm La, and ~9 to 29 ppm Y.

Zinc and lead concentrations in each sample are fairly low. Zn concentrations range from ~100 to 215 ppm, while Pb concentrations range from ~1 to 20 ppm. The outlier contains 311 ppm of Zn and 50 ppm of lead. Both Zn and Pb show slight positive relationships with silica.

Table 1: Representative major element and trace element data for well cutting samples from the Arbuckle Mountains in southeastern Oklahoma. Major element data is given in weight percent oxide and trace element data is given in parts per million.

	CB-PAW-10	CB-PAW-20	CB-PAJ-2	CB-PAJ-7	CB-PAN-13	CB-PAN-21
SiO_2	51.52	54.47	54.95	56.96	49.42	47.13
TiO_2	1.97	1.99	3.11	1.79	3.84	2.97
Al_2O_3	13.86	13.38	12.79	13.83	12.54	14.42
Fe_2O_3	4.75	5.30	5.39	5.06	5.85	4.87
FeO	6.96	7.59	7.24	6.90	9.39	9.31
MnO	0.21	0.22	0.19	0.17	0.23	0.23
MgO	6.08	4.15	4.53	4.32	4.51	5.89
CaO	7.92	7.19	4.02	5.23	7.22	9.86
Na_2O	3.24	3.46	3.02	3.61	3.48	2.75
K_2O	2.17	1.65	2.70	1.57	1.35	0.69
P_2O_5	0.31	0.36	0.65	0.31	0.58	0.40
Total	98.99	99.76	98.59	99.75	98.46	98.52
LOI	4.44	3.38	4.53	6.24	1.77	3.18
Ba	467	411	551	290	399	318
Ce	37	48	38	56	15	25
Co	46	45	42	45	50	52
Cr	84	49	35	28	71	104
Cu	100	104	111	100	181	103
Ga	14.7	16.7	19.0	17.0	17.9	17.5
La	12	21	19	21	11	12
Nb	19.8	27.3	42.1	32.7	30.2	16.9
Ni	55	37	33	42	42	70
Pb	1	4	10	12	5	1
Rb	27.0	27.0	37.0	23.4	20.5	12.1
Sc	35	33	26	31	34	37
Sr	321	288	244	219	373	392
Th	1.6	10.4	12.5	12.4	12.2	7.7
U	1.9	1.3	2.0	1.1	0.5	0.5
V	308	277	263	274	397	350
Y	31.4	42.5	52.6	46.6	37.1	28.1
Zn	102	150	134	130	135	118
Zr	147	238	360	274	283	149

Table 2: Representative normative mineralogical data for well cutting samples from the Arbuckle Mountains in southeastern Oklahoma. Normative mineralogy given in weight percent.

	CB-PAW-10	CB-PAW-20	CB-PAJ-2	CB-PAJ-7	CB-PAN-13	CB-PAN-21
Q	0.89	8.13	12.33	12.04	4.27	0.41
Or	12.91	9.76	16.18	9.29	8.09	4.13
Ab	27.61	29.30	25.91	30.60	29.85	23.57
An	16.98	16.12	13.55	16.92	14.99	25.28
Lc	0	0	0	0	0	0
Ne	0	0	0	0	0	0
Di	16.83	14.21	1.93	5.79	14.44	17.79
Hy	13.34	10.18	14.65	13.87	11.07	15.02
Ol	0	0	0	0	0	0
Mt	6.93	7.68	7.92	7.34	8.59	7.14
Il	3.76	3.78	5.98	3.40	7.38	5.70
Ap	0.74	0.85	1.56	0.73	1.39	0.96

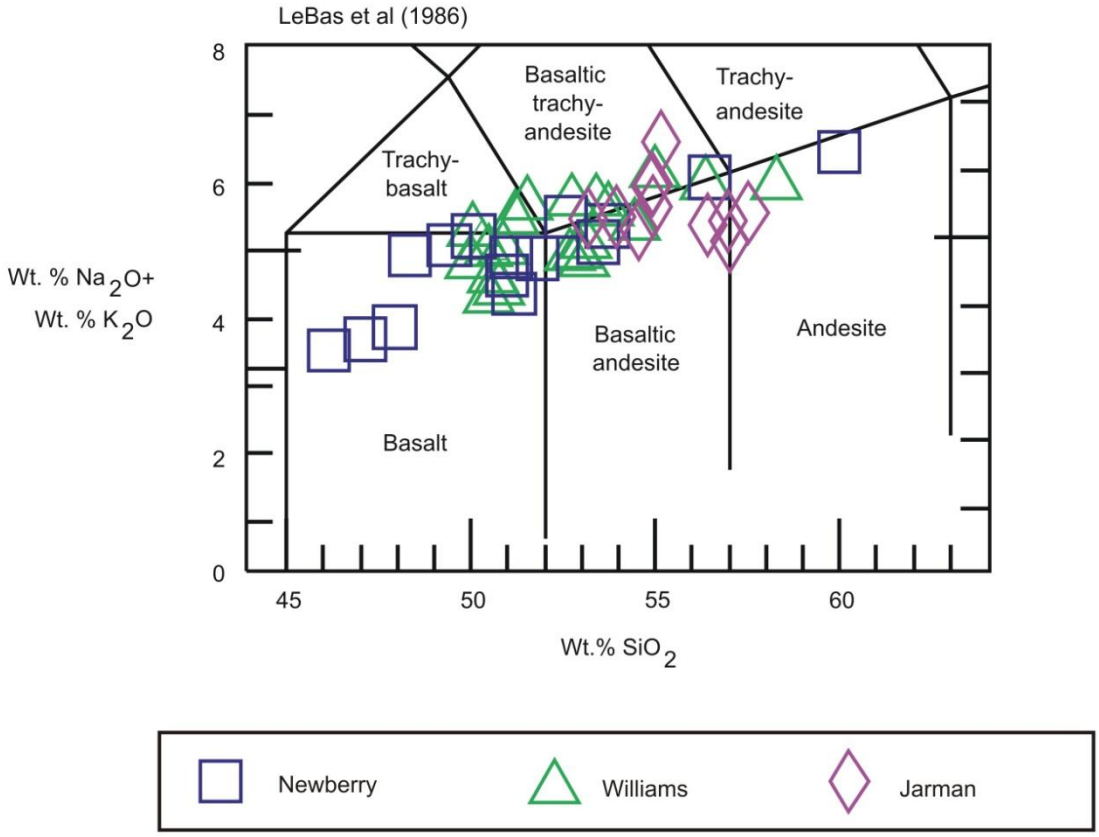

Figure 4: Total alkalis versus silica diagram of Le Bas et al (1986) used to classify igneous rocks utilizing major element concentrations.

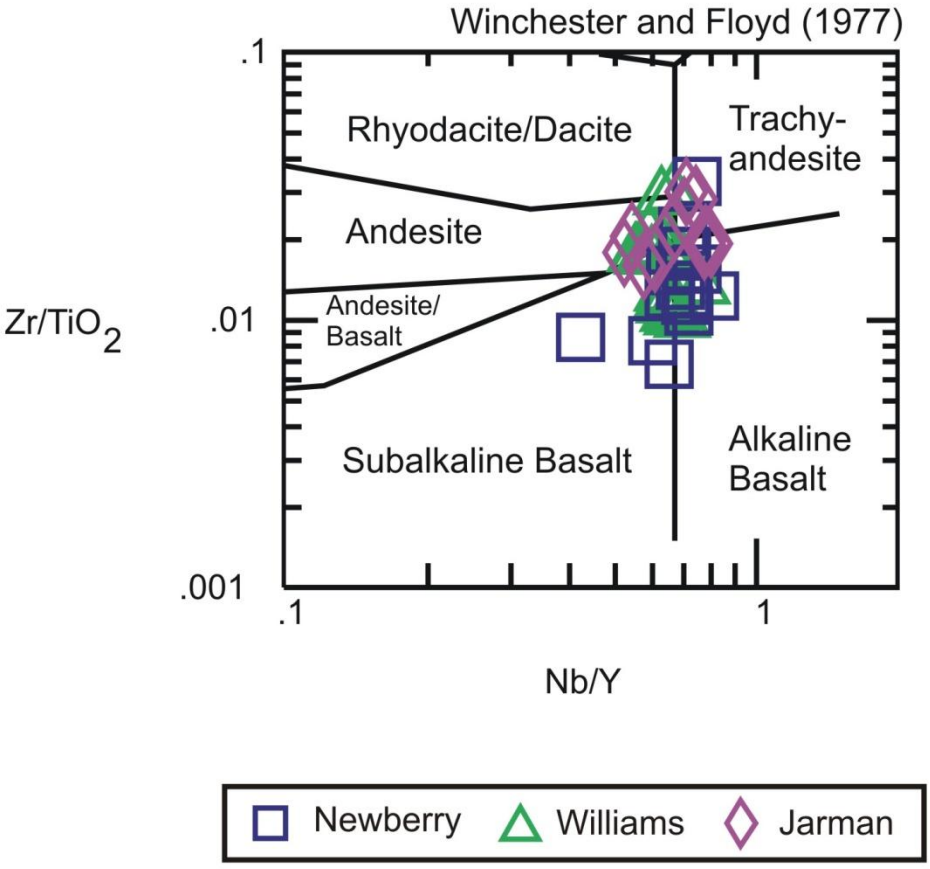

Figure 5: Zr/TiO2 versus Nb/Y diagram (Winchester and Floyd, 1977) to classify igneous rocks utilizing incompatible trace elements.

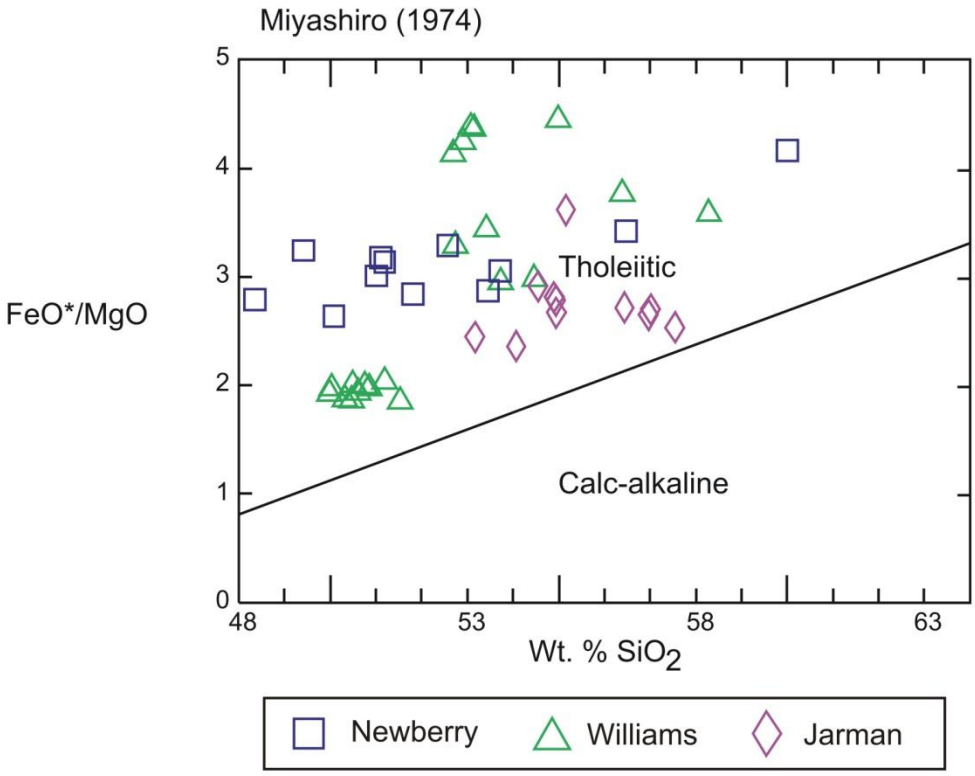

Figure 6: Discrimination diagram of Miyashiro (1974) distinguishing between tholeiitic and calc-alkaline magmas.

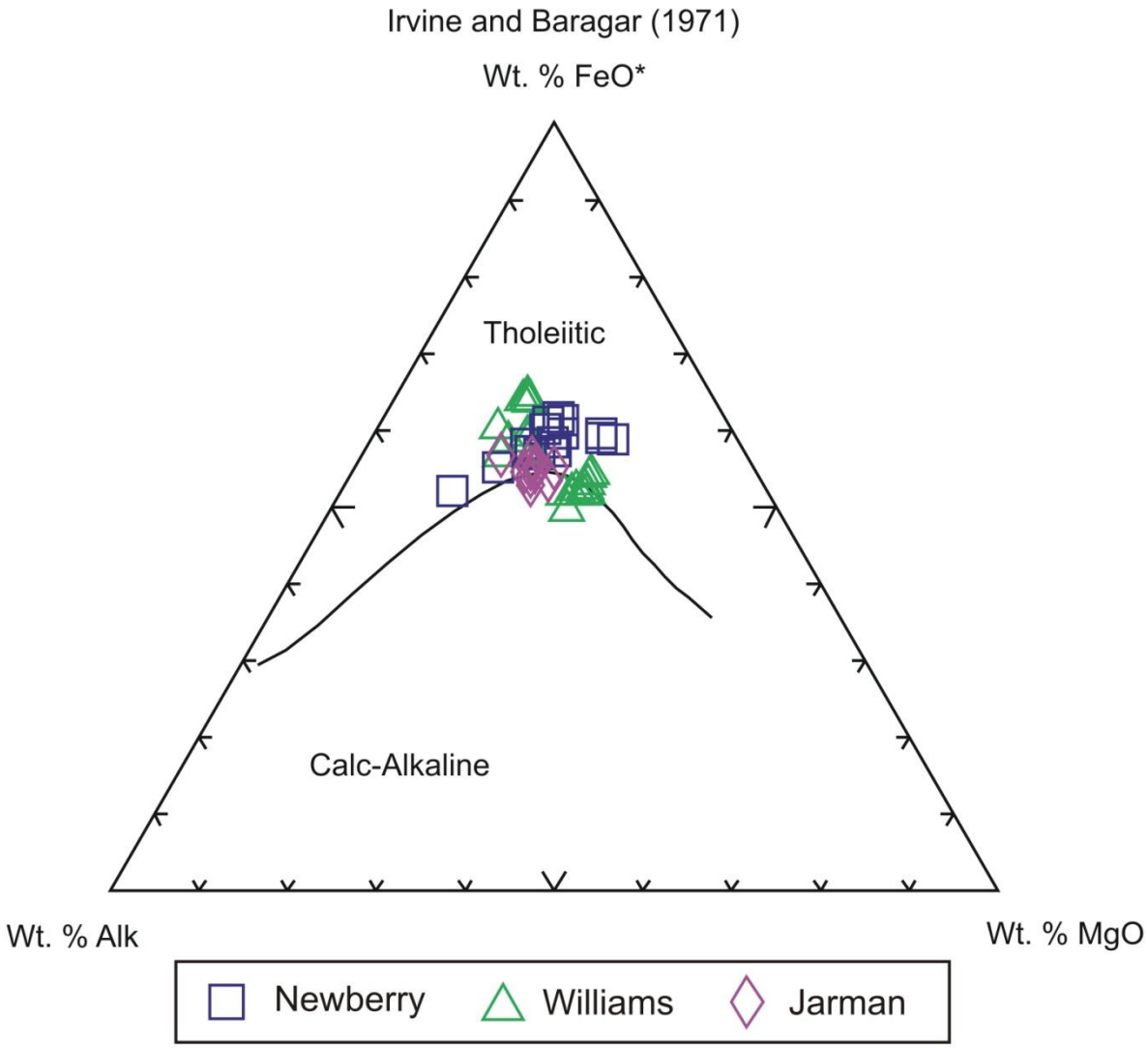

Figure 7: AFM diagram of Irvine and Baragar (1971) distinguishing between tholeiitic and calc-alkaline magmas.

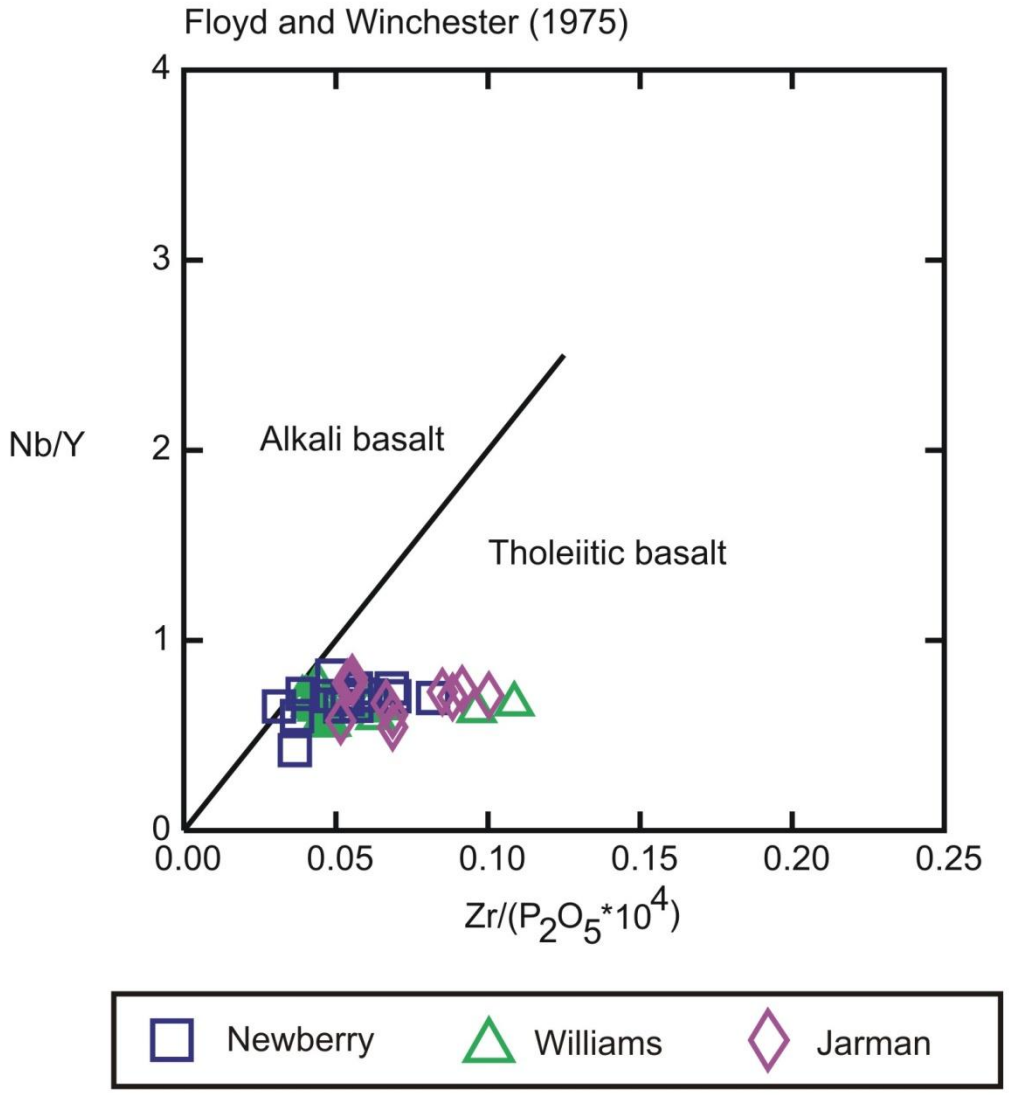

Figure 8: Discrimination diagram used by Floyd and Winchester (1975) to distinguish between tholeiitic and alkali basalts using incompatible trace elements.

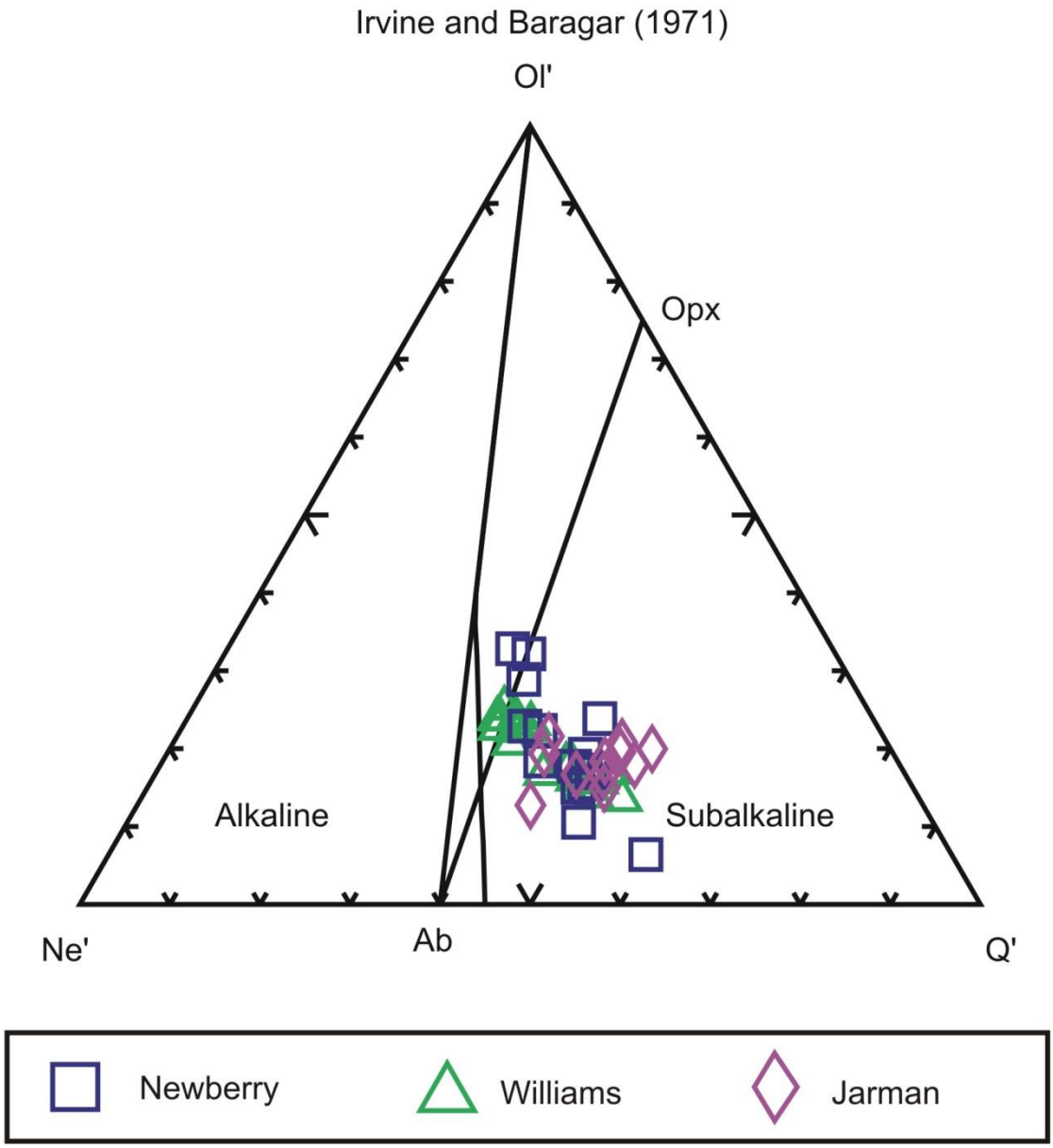

Figure 9: Ne'-Ol'-Q' diagram used by Irvine and Baragar (1971) to distinguish between alkaline and subalkaline magma types using normative mineralogy.

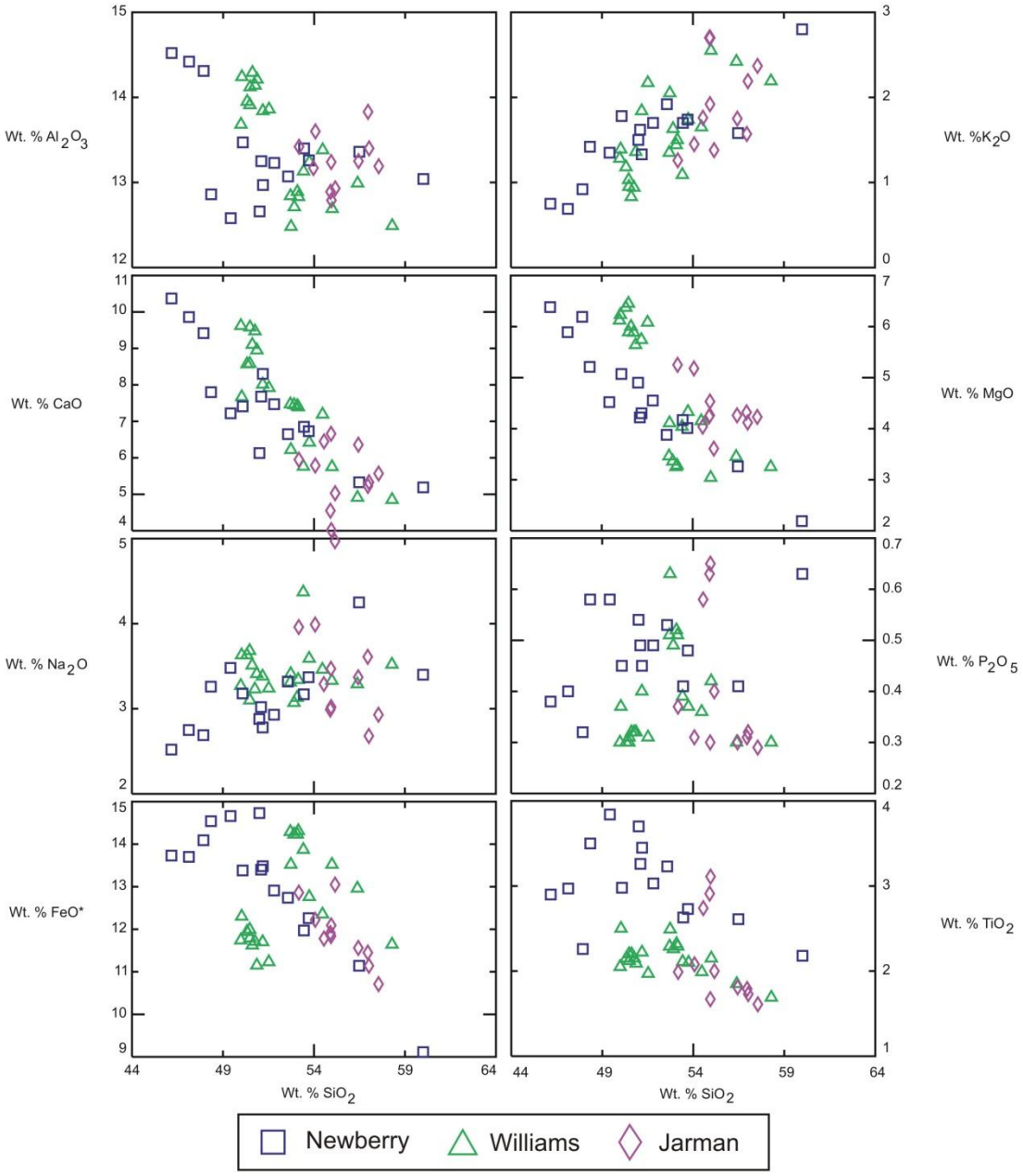

Figure 10: Harker diagrams depicting concentrations of major elements, in wt. %.

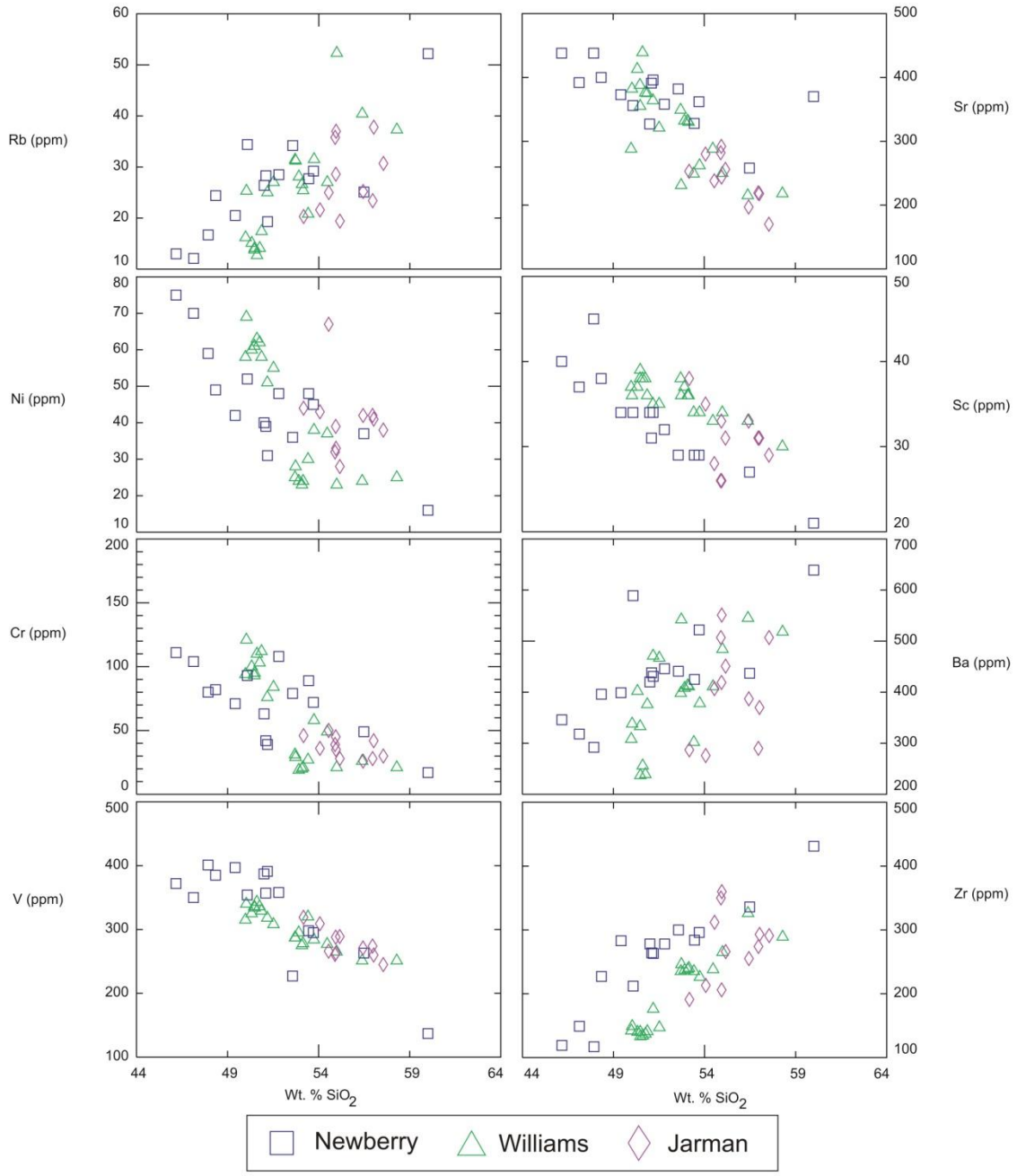

Figure 11: Harker diagrams depicting concentrations of selected trace elements, in ppm.

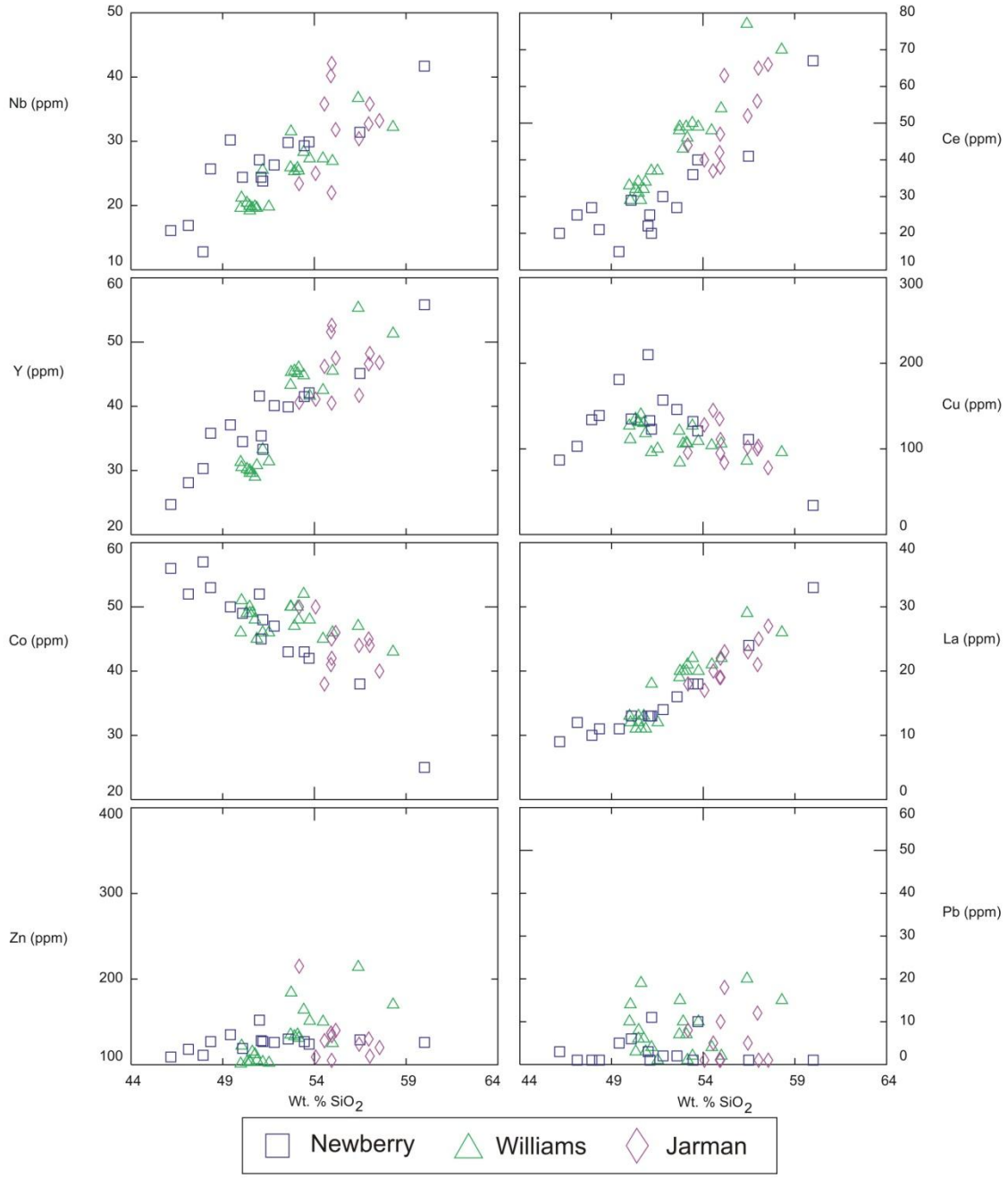

Figure 12: Harker diagrams depicting concentrations of selected trace elements, in ppm.

Chapter 4 - **Discussion**

Chemostratigraphy

Variations in the geochemistry of the samples with depth beneath the surface may be indicative of the presence of lava flow "packages," within each well. The term "lava flow package" is used here to indicate chemically-similar layers of lava flows that occur at adjacent depth intervals. These may be similar to the compound lava flows of Bondre and Hart (2008). While the depth intervals in which mafic well cuttings are present vary slightly between each of the three wells (Figure 2), comparisons of the geochemical properties of each sample can help to define stratigraphically separate flow packages (Shervais et al, 2006; Brueseke et al, 2007; Bondre and Hart, 2008). These comparisons were made using two methods: statistical correlations and chemostratigraphic variation diagrams.

Each analyzed sample was compared statistically using similarity coefficients to the remaining samples to determine how geochemically similar they were to each other (Borchardt et al, 1971; Borchardt et al, 1972). This was completed by determining how similar each individual concentration of a string of selected major and trace elements were for the two samples. These similarities were then averaged together to determine the similarity coefficient for the two compared samples. In general, if the samples are more than 91% similar, the two samples are considered similar to each other. When the similarity coefficient rises above 95%, the two samples are considered very similar to each other (Borchardt et al, 1971; Borchardt et al, 1972).

Appendix D shows similarity coefficients between samples analyzed from the wells. This appendix illustrates multiple points. For example, two samples from the Williams well (CB-PAW-2 and CB-PAW-4) show a similarity coefficient of 94.7%. However, few other similarity coefficients between the samples reach the requisite 91% to consider the samples geochemically related. This is the case for most samples compared by this method. The Williams well is the only of the three wells to contain a significant number of samples that have high enough similarity coefficients to consider them related. These samples are present are subsequent depths in the upper interval of the well (from ~1700 to 1950 meters below the surface). Samples CB-PAW-2 and CB-PAW-4 also appear to be related to CB-PAW-3, CB-PAW-5, CB-PAW-6, CB-PAW-7, and CB-PAW-8, while samples CB-PAW-11, CB-PAW-12, CB-PAW-13, and CB-

PAW-14 also appear to be related to each other. Only a handful of samples for the Newberry and Jarman wells appear related to even one other sample. This may indicate that two lava flow packages (e.g. potentially compound lava flows) that originate from geochemically-similar sources are present in the upper interval of the Williams well. Individual samples from separate wells do not exhibit high enough similarity coefficients to be conclusively related to each other. Therefore, individual samples from the Williams well cannot be correlated to the Jarman and Newberry wells using this method. This table also tells us that the geochemistry of the samples become less similar to each other the farther away the wells are located. These three wells are located linearly across a transect of three sections in townships T1N, R2W and T1N, R3W in southern Oklahoma, with the Williams and Newberry being present on the east and west ends of this transect, respectively, approximately 3.2 km apart from each other (Figure 3). This indicates a geochemical heterogeneity in samples from these wells that is likely a function of different magmatic and eruptive systems for the lava flows (Brueseke et al, 2007). Similar observations are found for Cenozoic basalts of the eastern Snake River plain (ID), that erupted from numerous and disparate shield volcanoes (e.g "plains-style" volcanism; Greely, 1982; Hughes et al., 1999).

Figure 13 depicts chemostratigraphic variation diagrams that show variations in compositions of SiO_2, FeO*, Ni, Zr, and K/P for each of the three wells analyzed. Concentrations of SiO_2 and FeO* are used to show variations in major elements, while Ni and Zr concentrations are used to show variations in compatible and incompatible trace elements. K/P ratios are indicators of crustal contamination. While the scale of the x-axis (depicting geochemical compositions) varies for each diagram, the scale of the y-axis (depicting depth from the surface in meters) is held constant. The middle interval (~1500 to 2000 meters) of each diagram is the most important for comparison between the three wells. The only apparent overlap in depth between mafic intervals in all three wells occurs from ~1600 to 1800 meters. This interval contains two samples from the Newberry well, five samples from the Jarman well, and six samples from the Williams well for these diagrams. Samples from the Newberry and Williams wells are the most similar to each other, as is sample CB-PAJ-11 (one of the Jarman samples). These contain relatively low silica concentrations (47-53 wt. %), similar FeO* concentrations (12-14 wt. %), nickel concentrations ranging from 40-65 ppm, relatively low zirconium concentrations (100-200 ppm), and moderate K/P values (5-10). While the individual samples cannot be traced across multiple wells, these samples appear to be similar enough in their

concentrations and patterns to indicate a geochemical relationship that represents a single flow package that can be correlated across all three wells.

The remaining four samples from the Jarman well are similar to these samples when comparing concentrations of FeO*, Ni, and Zr, but contain higher concentrations of silica (56-58 wt. %) and higher K/P values (8-16). These four samples cluster together with each other on the chemostratigraphic variation diagrams in the Jarman well, indicating that they may have evolved similarly to each other. Their relationship to other samples at this depth in each well is inconclusive. It is likely that they represent the same flow package.

Samples located in the upper intervals of the Newberry well (~1200 to 1600 m) are highly scattered and whether they represent specific flow packages is inconclusive. Upper interval samples in the Jarman well (located between 1000 to 1200 meters below the surface) are clustered together and are likely geochemically related to each other. This interval (featuring three samples) may represent a single flow package in the Jarman well. Samples are not present in the Newberry or Williams wells at these depths.

The lower interval samples in the Jarman and Williams wells (located from ~2000 to 2200 m and ~2500 to 2600 m below the surface, respectively) all cluster together as well. These lower interval samples in the Williams well contain the lowest concentrations of silica from any of the samples, indicating that these samples are likely less evolved geochemically than other samples analyzed. The lower interval samples in the Jarman well are clustered together and contain relatively moderate concentrations of silica, FeO*, but relatively lower concentrations of nickel and zirconium and lower K/P values. These samples may be related to the lower interval of samples from the Williams well, which occur at similar depths (~2000 to 2100 m) and have similar geochemical traits. This represents a second potential flow package that can be traced throughout multiple wells.

While the chemostratigraphic variation diagrams for the Newberry and Jarman wells in Figure 13 tell us a lot about these samples, the chemostratigraphic variation diagram in this figure for the Williams well is not as definitive, due to the higher number of samples present in the interval shown. Because of this, Figure 14 has increased the vertical scale of the diagram to better distinguish the relationship between each sample with depth. This diagram shows two continuous intervals of samples. The upper interval occurs between ~1700 and 1925 meters, while the lower interval (compared above to the lower interval of the Jarman well) occurs

between ~2000 and 2100 meters. These two intervals are separated by ~75 meters of rhyolite and/or granite. The upper interval shows two distinctive flow packages.

The first occurs between ~1700 and 1850 meters. This flow package may be related to samples present at the same depths in the Jarman and Newberry wells. While the selected major and trace element concentrations are very similar to each other in this flow package, there are variations with depth. The most notable variation is the increase in silica and K/P values with depth. These K/P values increase enough to likely indicate a higher amount of upper crustal contamination in the older flows. This occurs in two cycles within this flow package. The second flow package occurs between ~1850 and 1925 meters. This flow package has higher concentrations of silica, FeO*, and zirconium, as well as significantly lower concentrations of nickel than the first flow package. These lava flows also show an increase in silica and K/P values with depth.

Samples from the three wells show up to five possible flow packages. The deepest possible flow package (A) occurs at approximately 2550 meters below the surface in the Newberry well. While only two samples were obtained from this package, it is confined between two intervals of rhyolite, which may support the interpretation that it represents a single flow package. Additional samples from this interval may help confirm this. The second flow package (B) occurs between ~2000 and 2100 meters below the surface and may be present in both the Williams and Jarman wells. The third flow package (C) occurs between ~1850 and 1925 meters below the surface in the Williams well. It is separated from flow package B in the Williams well by ~75 meters of rhyolite and/or granite. The fourth flow package (D) occurs directly atop flow package C in the Williams well (~1700 to 1850 meters). This flow package may also be traced into the Jarman and Newberry wells, although more samples from each of these wells may help determine this relationship. Four samples from the Jarman well in this flow package appear to vary slightly from the remaining samples, possibly due to a higher amount of upper crustal contamination. The fifth and shallowest flow package (E) occurs at approximately 1050 meters below the surface in the Jarman well. This flow package contains only three samples, which are closely related to each other.

Discussion of possible flow packages have not taken into account possible variation in surficial elevation between these wells at the time of eruption. A slight variation in surficial elevation between the Jarman and Newberry wells could indicate a correlation between the

uppermost samples of both wells, which appear to have similar geochemical properties. However, for the purpose of this contribution, the topography of this region at the time of eruption is assumed to be fairly uniform given what has been observed in other continental flood basalt provinces and modern regions characterized by large numbers of basaltic eruptive centers.

Geochemistry and Normative Mineralogy

An expanded basalt tetrahedron illustrating experimental primary melt compositions and differentiation paths is shown on Figure 15 (Thompson et al, 1983). Samples from the Arbuckle Mountains plot along and as an extension of the 1 atm cotectic. This is common for flood basalt provinces around the world and indicates that the Arbuckle Mountains magmas were last equilibrated in the upper crust prior to eruption onto the surface (Thompson et al, 1983). Flood basalt provinces are also typically dominated by igneous suites of tholeiitic basalts and olivine tholeiites, both of which are present in the Arbuckle Mountains. Recent geophysical estimates for the volume of mafic igneous rocks in the subsurface of the Southern Oklahoma rift zone indicate that as much as 210,000 km^3 of mafic material may be present (Hanson et al, 2012). The presence of this large volume of mafic to intermediate igneous rocks, accompanied by large volumes of felsic material (up to 40,000 km^3) and the normative mineralogical data shown in Figure 15, supports the hypothesis that the Southern Oklahoma rift zone represents a large igneous province dominated by flood basalt volcanism. The presence of this material, accompanied with major and trace element data also supports the hypothesis that the Southern Oklahoma rift zone represents the failed arm of a three-armed radial rift system, as opposed to the leaky transform fault system suggested by Thomas (2011). Leaky transform fault systems are typically characterized by alkaline (to transitional) magmatic affinities (Skulski et al, 1991; Skulski et al, 1992). Continental rift environments commonly contain bimodal basalt-rhyolite igneous suites containing dominantly tholeiitic basaltic liquids (Hoffman et al, 1974; BVTP, 1981; Diez de Medina, 1988; Hanson et al, 2012). It is unlikely that this large volume of subalkaline mafic magma would be generated in and erupted through a leaky transform fault system.

Arrays present in the geochemical plots of Figure 7 suggests that samples that are more evolved formed from less-evolved basalts through fractional crystallization accompanied by upper crustal contamination, in some circumstances. The decreases in concentrations of MgO,

FeO*, and CaO as silica increases are byproducts of the crystallization of olivine, pyroxene, and calcium-rich plagioclase, as are the increases in concentrations of Na_2O and K_2O as silica increases.

Incompatible trace element ratios provide an insight into the mantle reservoirs that source igneous material. These ratios include Zr/Nb, La/Nb, Ba/Nb and Ba/Th. K/Nb and K/P ratios are indicators of crustal contamination. K concentrations increase when igneous rocks are exposed to upper crustal rocks, raising the K/Nb and K/P ratios. K/Nb, Ba/Nb, and Ba/Th ratios are also indicators of a subduction zone environment. Ba concentrations increase and Nb concentrations decrease in a subduction zone environment, causing increases in these ratios. The incompatible trace element ratios of the samples resemble those of enriched mantle ocean-island basalts (EMI OIB). Typical EMI OIB contains Zr/Nb values ranging from 5 to 10, La/Nb values ranging from 0.75 to 1.25, Ba/Nb values ranging from 10 to 20, Ba/Th values ranging from 80 to 150, and K/Nb values ranging from 200 to 500 (Weaver, 1991). As shown in Figure 16, the samples contain Zr/Nb values ranging from 8 to 10, La/Nb values ranging from 0.5 to 1.0, Ba/Nb values ranging from 10 to 20, Ba/Th values ranging from 50 to 150, and K/Nb values ranging from 300 to 600. This suggests that the mafic well cuttings of southern Oklahoma formed from a mantle source enriched in large-ion lithophile elements (LILE). This enrichment in LILE, according to Weaver (1991), can be achieved from a source primarily composed of ancient oceanic crust contaminated by pelagic sediments. Subsurface magma bodies where the Arbuckle mafic magmas resided in prior to eruption were also likely contaminated by continental crust (e.g. coeval rhyolite/granite, or other K-rich upper crust), especially as the magma began to evolve to basaltic andesites and andesite compositions. This is evident from the increased K/P ratio values present in some samples. K/P values greater than five are indicative of contamination of basaltic magma with upper continental crust (Carlson and Hart, 1987). Arbuckle samples with higher silica concentrations (>54 wt. %) show an increase in K/P values to as much as 16. This increase is also shown definitively in Figure 14 with samples from the Williams well. Vertical variation from this trend is an indicator of magma mixing or crustal assimilation (e.g. open-system processes).

Multi-element diagrams normalized to mid-ocean ridge basalts (MORB; modified from Pearce, 1983) are shown in Figure 17 for each of the analyzed wells. Each well shows

enrichment in barium in relation to other LILE, which is common for EMI OIB (Weaver, 1991). The relative enrichment of all LILE is also common for EMI OIB (Weaver, 1991).

On the tectonic discrimination diagram used by Meschede (1986) shown in Figure 18, the samples plot dominantly as intraplate tholeiitic basalts. Figure 19 shows the tectonic discrimination diagram of Pearce and Cann (1973). The samples plot in fields C and D, which represent intraplate basalts and calc-alkaline basalts. These fields are also commonly associated with intraplate OIB. The well cuttings also plot as OIB on the discrimination diagram of Mullen (1983), shown in Figure 20. Overall, the mafic well cuttings of the Arbuckle Mountains appear to represent tholeiitic basalts to andesites that originate from an enriched mantle source (EMI OIB), where melts of this source were contaminated by upper continental crust, as they evolved via dominantly fractional crystallization.

Relationship to Wichita Mountains

Samples from the Arbuckle Mountains are compared here to three mafic plutonic units in the Wichita Mountains (Roosevelt Gabbros, Late Diabase Dikes, and Kimbell Gabbro). Data for the Navajoe Mountain Basalt-Spilite Group is limited, but comparisons are made between the Navajoe Mountain Basalt-Spilite Group and Arbuckle samples using the available geochemical data. The Navajoe Mountain Group contains basalt and altered basalt that are not exposed on the surface (Shapiro, 1981). The Roosevelt Gabbros represent a series of gabbroic plutons ~552 Ma that have been classified as hydrous olivine tholeiites. They are composed of four separate units (Sandy Creek, Glen Creek, Mount Sheridan, and Mount Scott). Roosevelt Gabbro outcrops are spread throughout the Wichita Mountains and are intruded by later felsic volcanism (Cameron et al, 1986; McConnell and Gilbert, 1990).

Late Diabase Dikes represent the latest stage of magmatism in the Wichita Mountains. They exhibit tholeiitic to transitional geochemical affinities and display geochemical traits that represent an intraplate extensional environment. They also appear to be related to a small body of gabbro located north of the main portion of the Wichita Mountains, known as the Kimbell Gabbro (Gilbert and Hughes, 1986; McConnell and Gilbert, 1990; DeGroat et al, 1995).

Geochemical comparisons between these mafic units and the Arbuckle well cuttings are shown in Figure 21. Geochemical data for the Roosevelt Gabbros was collected from Shapiro (1981), Gilbert and Hughes (1986), Aquilar (1988), and Diez de Medina (1988), while data for

the Late Diabase Dikes and Kimbell Gabbro were collected from Gilbert and Hughes (1986) and DeGroat et al (1995). Samples from the Late Diabase Dikes and Kimbell Gabbro are limited to lower silica concentrations (~44-46 wt. %). These samples contain a range of nickel concentrations (~10-90 ppm) and MgO concentrations (~4.5-8.0 wt. %), but fairly confined concentrations of K_2O (~0-1.8 wt. %) and Zr (~100-160 ppm). Values for Zr/Nb range from 6-10, consistent with typical EMI OIB values (5-10), as well as values for the analyzed samples from the Arbuckle Mountains (~8-10). K/P values in the Late Diabase Dikes and Kimbell Gabbro remain close to primitive (five or below).

Most of the arrays of the well cuttings from the Arbuckle Mountains trace back to the fields in which the Late Diabase Dike and Kimbell Gabbro data are present. While this may indicate that the Late Diabase Dike and Kimbell Gabbro have a similar magma source to the samples of the Arbuckle Mountains, the samples appear to be more similar to the Roosevelt Gabbros.

The Roosevelt Gabbro data extends over a wider range of silica concentrations (~45-55 wt. %). Arrays present in the Roosevelt Gabbros in Figure 21 are very similar to those of the samples of the Arbuckle Mountains. Both contain increasing values of K_2O and Zr with increasing silica, as well as decreasing MgO and Ni concentrations. Zr/Nb values for both the Roosevelt Gabbros and the basalts of the Arbuckle Mountains range from ~8-10 ppm. K/P values for the Roosevelt Gabbros remain near primitive values (~5), while the higher silica samples rise to as high as 15. This, however, is likely a by-product of upper crustal contamination that would have occurred as the magmas were rising closer to the surface to erupt. The samples of the Arbuckle Mountains extend beyond the fields of the Roosevelt Gabbros, but continue the array.

Due to these similarities, it is likely that the Roosevelt Gabbros represent the intrusive equivalent of the Arbuckle samples. The similarities between the Roosevelt Gabbros and the analyzed well cuttings of the Arbuckle Mountains indicate a genetic relationship, especially since they are located in close proximity to each other and are both interlayered with the Carlton Rhyolite. This relationship supports the hypothesis that the Southern Oklahoma rift zone extends linearly from the Arbuckle Mountains to the Wichita Mountains and was the site of large volumes of bimodal basalt-rhyolite volcanism.

Geochemical comparisons between the Navajoe Mountain Basalt-Spilite Group and the samples from this study are shown in Figure 22. These comparisons are limited to TiO_2 (wt. %), Fe_2O_3* (wt. %), Rb (ppm), Sr (ppm), Zr (ppm), and Y (ppm) data. Data for the Navajoe Mountain Basalt-Spilite Group was collected from Shapiro (1981). Samples from the Navajoe Mountain Basalt-Spilite Group contain relatively low concentrations of Zr (100-150 ppm), which coincide with the least evolved samples from the Arbuckle Mountains. These samples contain varying concentrations of Sr (200-400 ppm), but fairly confined concentration of TiO_2 (~3 wt. %), Fe_2O_3* (10-12 wt. %), Rb (5-10 ppm), and Y (5-10 ppm). Zr/Sr values range from 0.25 to 0.55 and Zr/Sr values for the Arbuckle Mountains samples trace back to the field containing Navajoe Mountain Basalt-Spilite Group samples. Arrays present within the Arbuckle Mountains sample data for Fe_2O_3*, Rb, and Sr also appear to trace back to fields for the Navajoe Mountain. Together, these relationships suggest that the Navajoe Mountain represent less evolved lava flows than are present in the Arbuckle Mountains and that both are broadly related. The Navajoe Mountain does contain much lower concentrations of Y, which may be caused by lower levels of fractional crystallization that has affected these samples. While the Navajoe Mountain Basalt-Spilite Group appears to have a genetic relationship to the Arbuckle Mountain samples, additional data for Navajoe Mountain samples are needed to better determine this relationship.

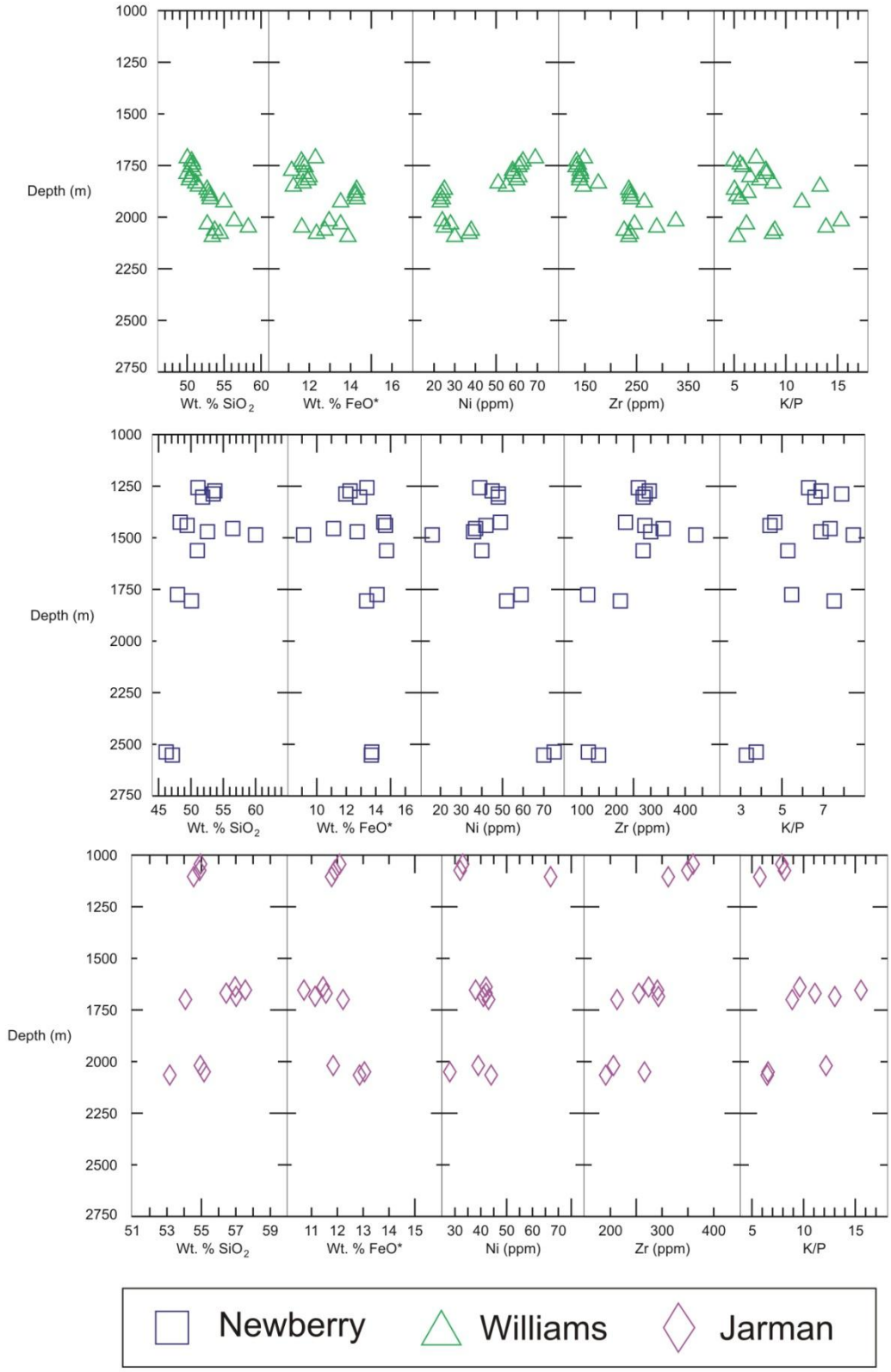

Figure 13: Chemostratigraphic diagrams depicting variations in the geochemistry of basalts present in each well with depth (meters).

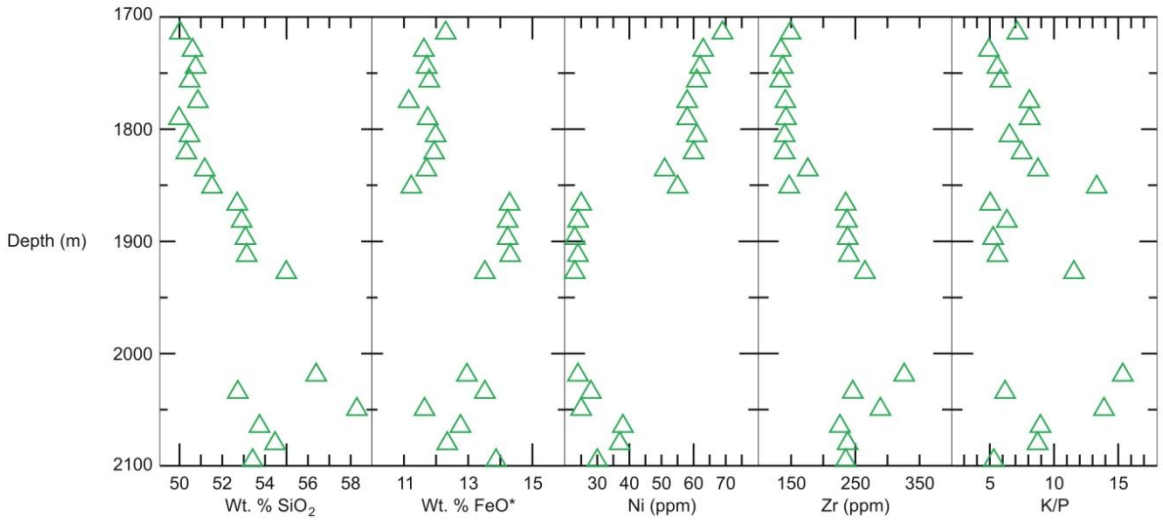

Figure 14: Chemostratigraphic diagrams for the Pan-Am Williams well. This diagram increases the scale of the y-axis to show geochemical variation in the Williams well more effectively.

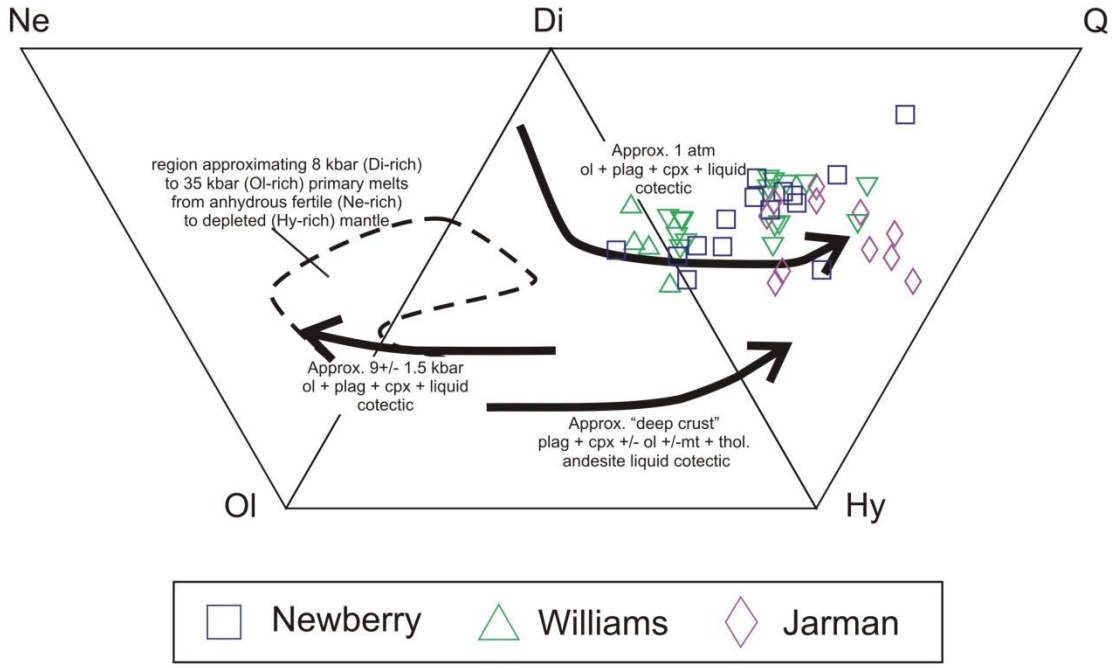

Figure 15: Expanded basalt tetrahedron used by Thompson et al (1983). Analyzed samples plot as an extension to the 1 atm cotectic. Similar patterns occur in other flood basalt provinces, such as the Columbia River-Oregon Plateaus (Thompson et al, 1983; Brueseke et al, 2009).

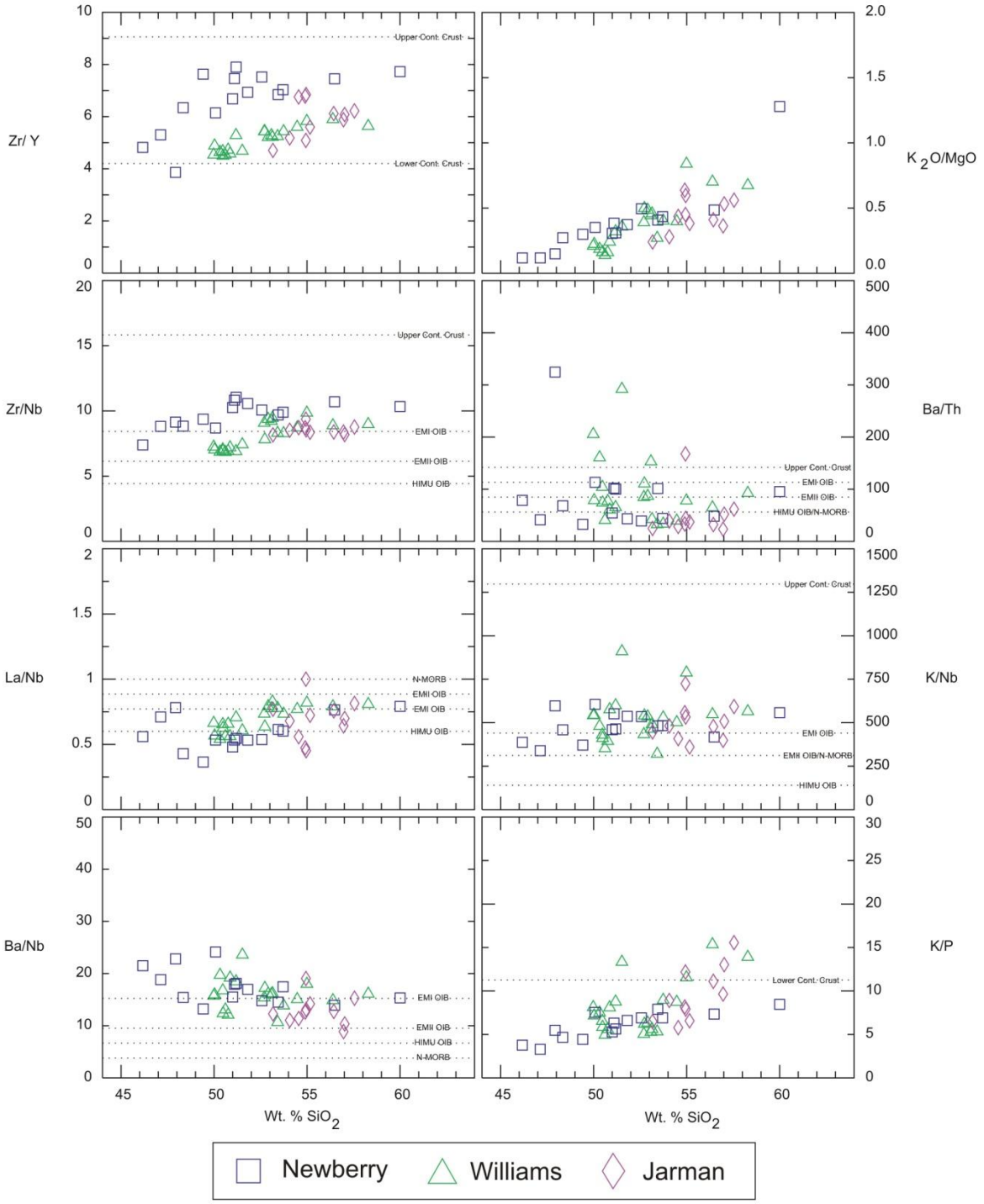

Figure 16: XY-diagrams plotting incompatible major and trace element ratios versus silica concentrations (wt. %). Values for average EMI OIB, EMII OIB, HIMU OIB, N-MORB, and continental crust are shown from Weaver (1991) and Rudnick and Gao (2003).

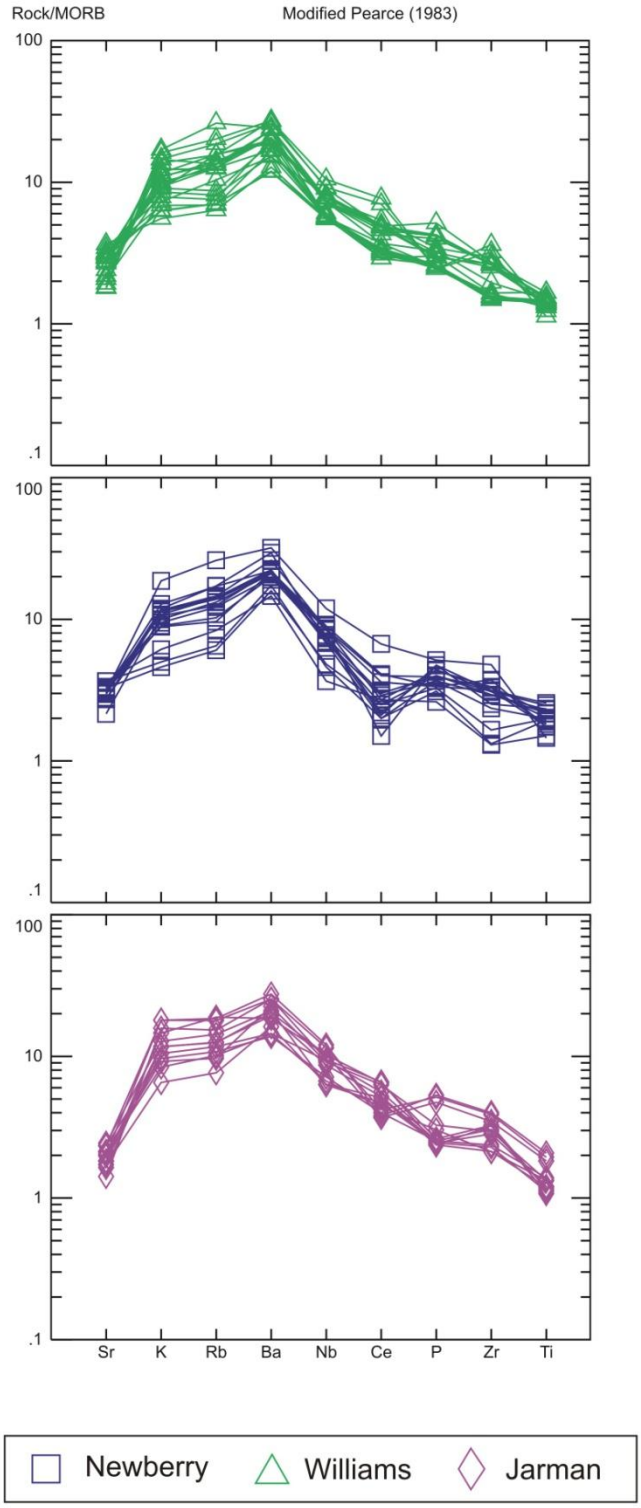

Figure 17: MORB-normalized Spider diagrams, modified from Pearce (1983), for each of the three wells (Pan-Am Jarman; Pan-Am Williams; Pan-Am Newberry) analyzed in the Arbuckle Mountains of southeastern Oklahoma.

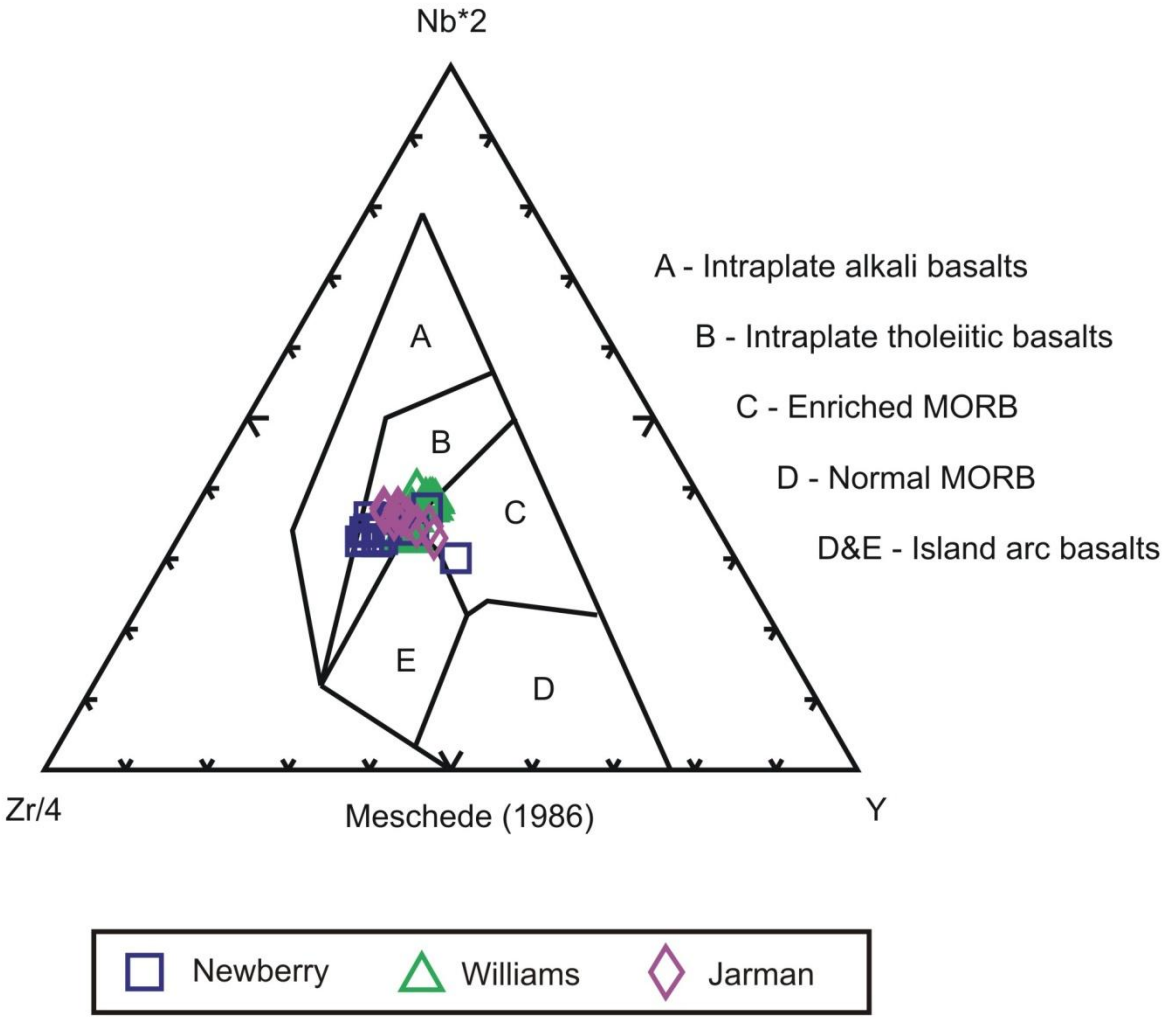

Figure 18: Discrimination diagram of Meschede (1983), utilizing incompatible trace elements.

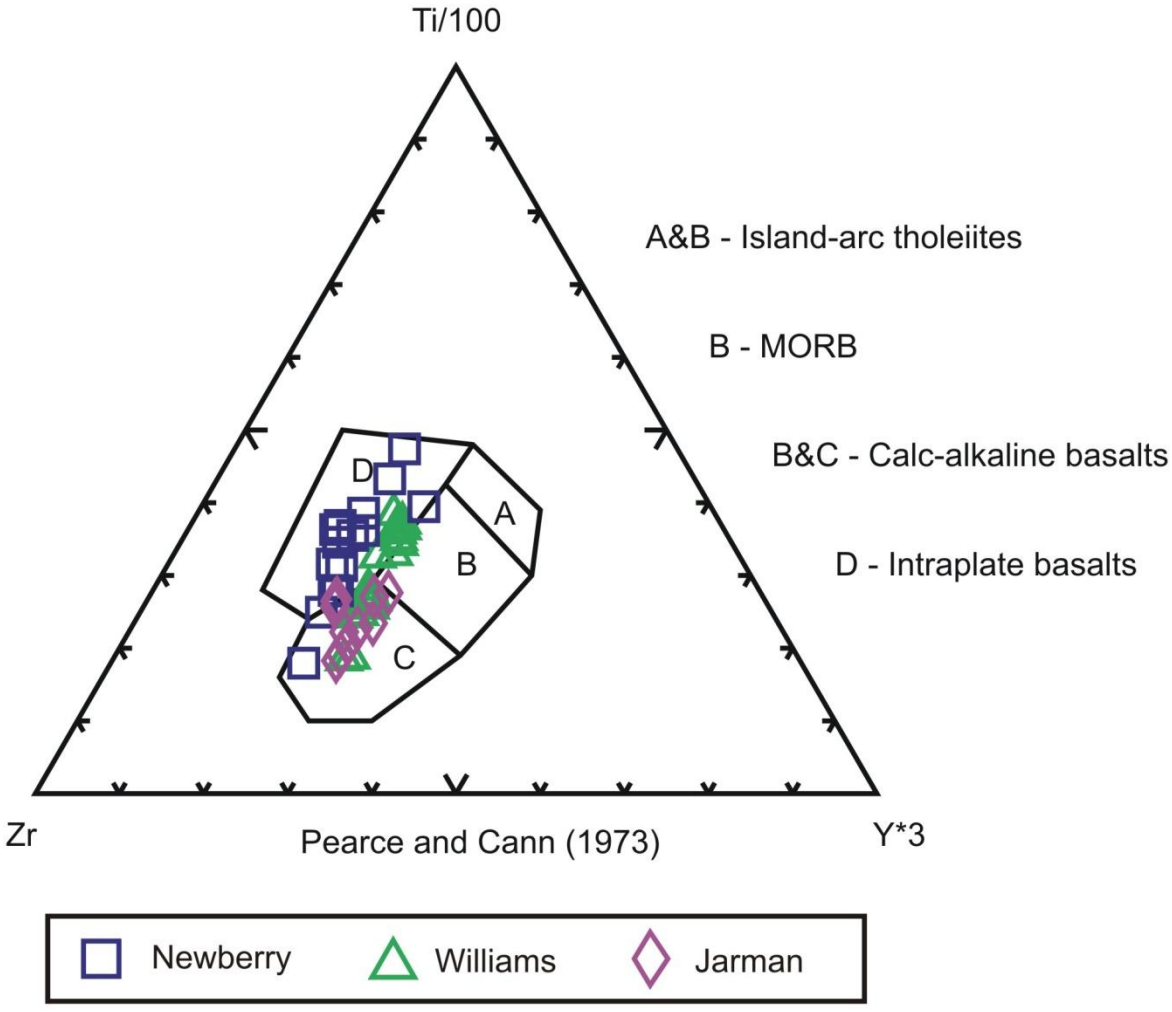

Figure 19: Discrimination diagram of Pearce and Cann (1973), utilizing Ti, Zr, and Y concentrations.

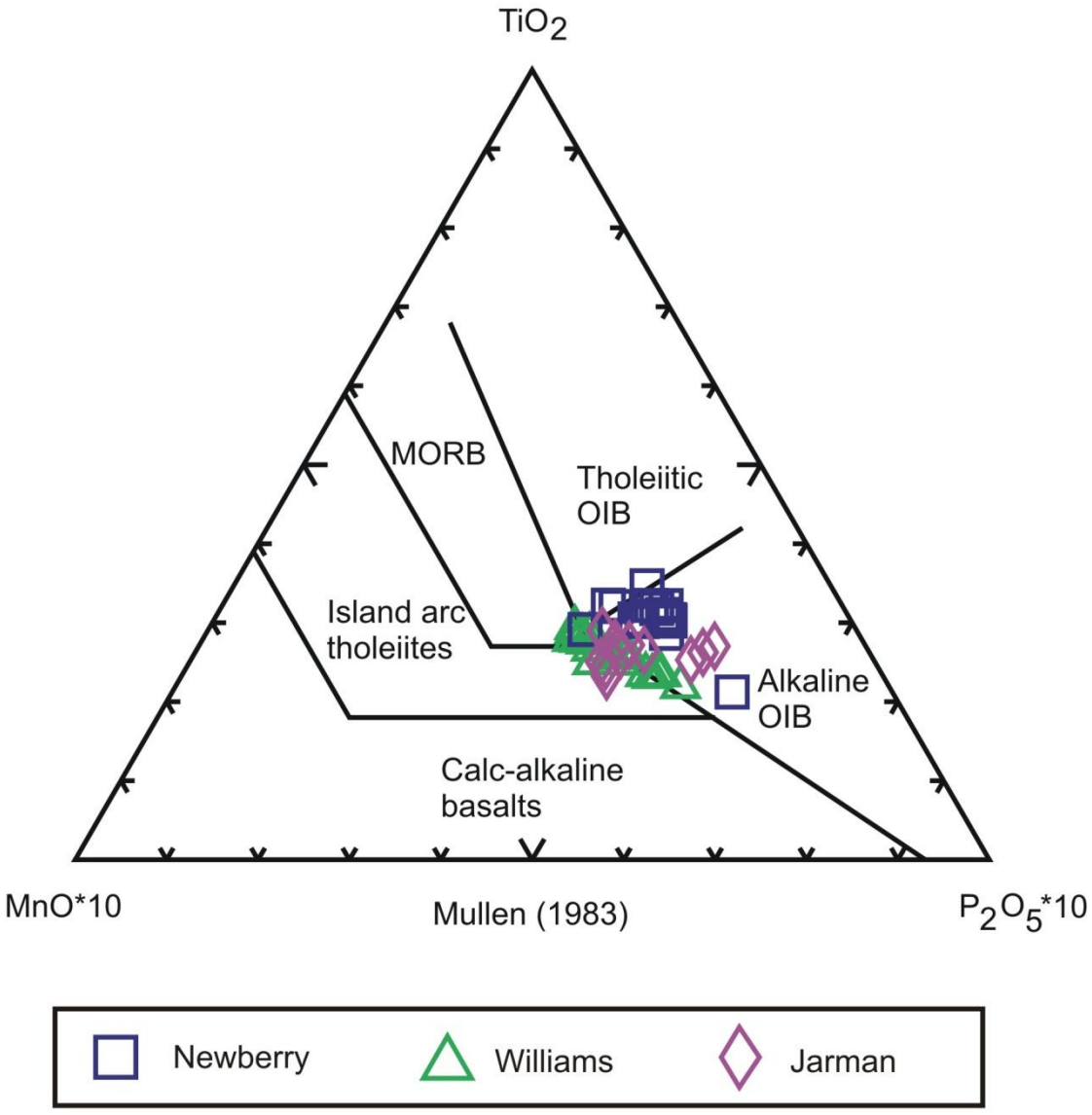

Figure 20: Discrimination diagram of Mullen (1983), utilizing major element concentrations.

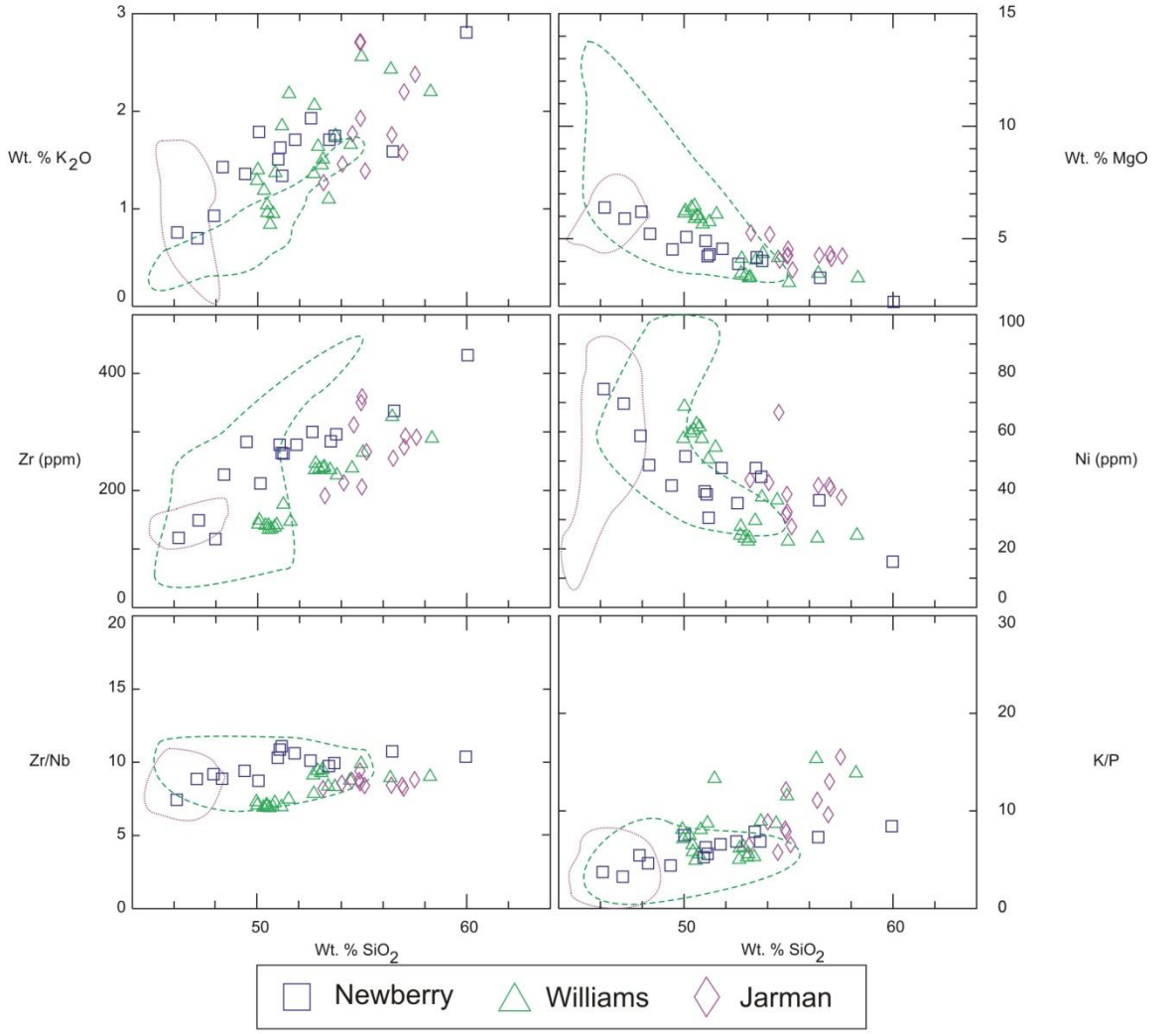

Figure 21: XY-diagrams showing concentrations of K_2O (wt. %), MgO (wt. %), Zr (ppm), Ni (ppm), Zr/Nb, and K/P versus silica concentrations. The field outlined in purple dots represents data for the Late Diabase Dikes and Kimbell Gabbro from Gilbert and Hughes (1986) and DeGroat et al (1995). The field outlined in green dashes represents data for the Roosevelt Gabbros from Shapiro (1981), Gilbert and Hughes (1986), Aquilar (1988), and Diez de Medina (1988).

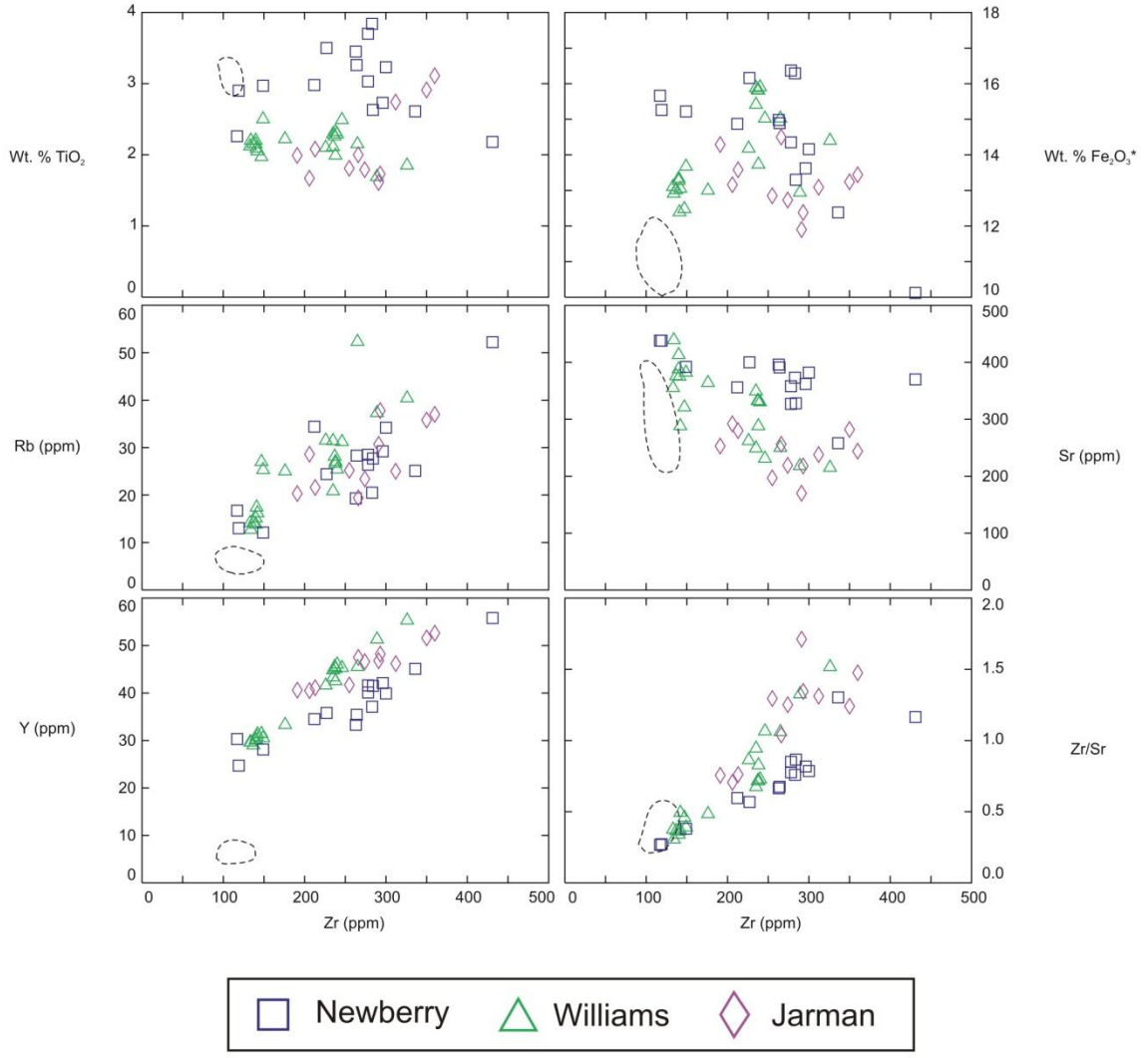

Figure 22: XY-diagrams showing concentrations of TiO_2 (wt. %), Fe_2O_3* (wt. %), Rb (ppm), Sr (ppm), Y (ppm), and Zr/Sr versus Zr concentrations (ppm). The field outlined in black dashes represents data for the Navajoe Mountain Basalt-Spilite Group (NMBSG) from Shapiro (1981). Limited data is available for the NMBSG.

Chapter 5 - **Comparisons to Other Flood Basalt Provinces**

Geochemical characteristics for samples from the Arbuckle Mountains are compared here to those of two other large igneous provinces around the world (Columbia River-Oregon Plateaus and East African Rift System). These comparisons are used to help define the type of geologic setting that the samples from the Arbuckle Mountains were formed in, as well as determine whether the mafic igneous sequence of the Arbuckle Mountains represents a flood basalt province. The Columbia River-Oregon Plateaus and the East African Rift System were chosen due to their relatively young age and low levels of alteration. These properties have made these locations two of the most researched and geochemically constrained large igneous provinces present on the planet.

Columbia River and Oregon Plateaus

The Columbia River Basalt Group and Steens Basalt are part of one of the most extensively studied flood basalt provinces in the world, due to their relatively young age, small size, easy accessibility, and low levels of alteration. Because of this, researchers have a reasonable knowledge of the distribution of lava flows and flow packages on the surface of the Columbia River and Oregon Plateaus.

The Columbia River Basalt Group covers approximately 200,000 km^2 in southeastern Washington, northeastern Oregon, and western Idaho, forming a series of stacked sheet lava flows with an estimated 234,000 km^3 of basalt (Hooper et al, 2007). The rapid eruption of this large volume of dominantly tholeiitic basaltic lava flows is typical of large flood basalt provinces around the world. The Columbia River Basalt Group erupted approximately 98% of its entire flood basalt package within the first 1.5 million years of its eruption (Hooper, 2000).

The Steens Basalt represents the initial pulse of magmatism in the Columbia River and Oregon Plateaus. Samples from the Steens Basalt vary chemically from olivine tholeiites and high-alumina basalt to more evolved basaltic andesites, trachybasalts, and basaltic trachyandesites (Brueseke et al, 2007). The Imnaha Basalts is the oldest formation present on the Columbia River Plateau in northeastern Oregon and southeastern Washington, erupting between 17.5 and 16.0 Ma (Barry et al, 2010). The Imnaha Basalts are plagioclase and olivine-phyric basalts (Hooper et al, 2007). The Grande Ronde Basalts accounted for 60% of the entire

sequence of basalt erupted in the Columbia River Plateau. As opposed to the Steens and Imnaha Basalts, the Grande Ronde Basalts are aphyric tholeiitic basaltic andesites(Hooper et al, 2007).

While there is still considerable debate about the origin of the flood basalt province (e.g. mantle plume vs. non-plume models), the whole rock geochemistry and radiogenic isotope data of Columbia River basalt group lava flows indicate that they originated from a mantle source with OIB-like chemistries. However, the less voluminous Steens Basalt have radiogenic isotope and trace element characteristics similar to depleted MORB. The Grande Ronde Basalts display clear enrichments in lithospheric components, although these enrichments are not present in the Imnaha Basalts. The bulk chemistry and radiogenic isotope data from select samples of the Columbia River Basalt Group and Steens Basalt also indicate crustal assimilation affected the magmas as they evolved (Hart et al., 1989; Carlson and Hart, 1987; Hooper et al, 2007; Brueseke et al, 2007).

Comparisons with Samples of this Study

Figures 23 and 24 depict geochemical comparisons between the Grande Ronde and Imnaha Basalts of the Columbia River Basalt Group, the Steen Basalts, and the well cuttings analyzed in this study. Samples from this study display similar arrays as those present in the Columbia River and Oregon Plateaus. These samples plot within fields created by the Columbia River Basalt Group and Steens Basalt on diagrams that plot wt. % K_2O and wt. % MgO versus silica, as well as on Ni (ppm) and Zr (ppm) plots versus silica. Analyzed basaltic andesites to andesites from the Arbuckle Mountains contain higher concentrations of zirconium than is present in those of the Columbia River Basalt Group and Steens Basalt, while the Columbia River Basalt Group and Steens Basalt contain up to four times as much nickel as analyzed well cuttings from the Arbuckle Mountains. These differences are likely due to different crystallization histories between the samples from the Arbuckle Mountains, the Columbia River Basalt Group and Steens Basalt. Despite these differences, similar trends and concentrations of major and trace elements support the hypothesis that the samples from the Arbuckle Mountains are representative of a flood basalt province.

The Zr/Nb values of the Columbia River Basalt Group and Steens Basalt are higher than those of the analyzed samples of the Arbuckle Mountains. These values in the Columbia River Basalt Group and Steens Basalt have been attributed to their derivation from multiple sources

chemically similar to OIBs and depleted MORBs. The analyzed samples from the Arbuckle Mountains have Zr/Nb values that remain around enriched mantle OIB source values and as mentioned earlier, indicate that they likely originated from a single source with chemical characteristics similar to EMI OIB.

Ba/Th values from the Columbia River Basalt Group and Steens Basalt are much higher than those of the Arbuckle Mountains, with Ba/Th values reaching as high as 1,000 in the Steens Basalt and 600 in the Grande Ronde. The samples from the Arbuckle Mountains do not rise above 300 with the majority of the samples remaining around 100. These values are indicative of an EMI OIB mantle source, which has Ba/Th values ranging from 100 to 150 (Weaver, 1991). The samples from the Columbia River Basalt Group and Steens Basalt have values that are much higher and can be attributed to upper crustal contamination, which raises concentrations of Ba in the samples, causing the Ba/Th ratio to increase, as well.

K/Nb values from the Columbia River Basalt Group and Steens Basalt are also higher than those of the Arbuckle Mountains. K/Nb values for samples from the Columbia River Basalt Group and Steens Basalt range from 100 to 1,500. These values are consistent with high amounts of upper crustal contamination, which typically displays K/Nb values above 1300. The majority of the Arbuckle Mountains samples display K/Nb values around 400 to 500 with some samples rising as high as 950. Samples with higher K/Nb values are exhibiting higher amounts of upper crustal contamination. The remaining samples are indicative of an EMI OIB magma source with some upper crustal contamination. EMI OIB magmas contain K/Nb values ranging from 200 to 450 (Weaver, 1991).

K/P values from the Columbia River Basalt Group, Steens Basalt, and analyzed samples of the Arbuckle Mountains show an increasing trend with increasing zirconium contents. Any increase in these values above five can be attributed to upper crustal contamination, which likely occurred in both of these regions, although to different extents. The Imnaha Basalts from the Columbia River Basalt Group display K/P values that reach as high as 17 with basalts, while the analyzed samples from the Arbuckle Mountains only show an increase above five in more evolved basaltic andesite and andesite samples.

The similarities between the Columbia River Basalt Group, Steens Basalt, and the analyzed well cuttings of the Arbuckle Mountains provide an insight to the petrogenesis of the samples from the Arbuckle Mountains. The presence of large volumes of tholeiitic basalts to

andesites in the Arbuckle Mountains, coupled with the major and trace element characteristics presented here, is similar to what is present in the Columbia River and Oregon Plateaus, indicate that the analyzed well cuttings from the Arbuckle Mountains represent a flood basalt province likely originating from an EMI OIB source magma coupled with upper crustal assimilation. Incompatible trace element ratios partially overlap, between provinces, however the Columbia River and Oregon Plateau lava flows are characterized by ratios that have also been influenced by what appears to be a greater (overall) upper crustal component, as well as a subduction-related component (e.g. high Ba, low Nb), that reflects their location behind an active volcanic arc in the mid-Miocene.

East African Rift System

The Ethiopian volcanic province, divided into the Main Ethiopian Rift (MER), the Afar Rift, and surrounding plateaus, represents the northern portion of this rift system. The surrounding plateaus are characterized by basaltic lava flows that were extruded through fissures. These large basaltic lava plateaus are accompanied by significant amounts of rhyolitic and intermediate composition lavas erupted from similar fissures and multiple vent complexes in the region (Hart et al, 1989).

The birth of the modern East African Rift is attributed to the onset of flood basalt volcanism in Ethiopia, Eritrea, and Yemen that began in the late Oligocene (~28 Ma; Furman, 2007). This volcanism is associated with an estimated 350,000 km^3 of flood basalts that began with the breakup of the Afro-Arabian shield causing the formation of the Red Sea. This event represents the third arm of a triple junction in eastern Africa. Volcanism reached the central and northern portions of the Main Ethiopian Rift at the same time the three arms connected to each other to form the Afar triple junction approximately 11 Ma (Furman, 2007).

Overall, the flood basalts in the MER display tholeiitic to transitional geochemical affinities. Samples become more tholeiitic in the 6-4 Ma period and more alkalic during the last 3 Ma (Hart et al, 1989). Incompatible elements display within-plate characteristics in many of the MER lavas. Ba and Nb enrichments are also common within the MER lavas, which are also common in oceanic ridges and oceanic islands, as well as in other continental flood basalt provinces (Hart et al, 1989). The Afar Rift also displays transitional to tholeiitic geochemical

affinities. The Afar region exhibits geochemical characteristics common in oceanic ridges and oceanic islands (Hart et al, 1989).

During the initial stages of rifting in the MER, lithospheric melting was prominent and upper crustal contamination significant. As rifting continued, depleted asthenospheric melting became more important, initially as a component for magma mixing, but eventually as the controlling mantle reservoir. Depleted MORB mantle controlled magma generation in the Afar Rift and Red Sea during the formation of oceanic crust (Hart et al, 1989). Furman (2007) suggested that the East African Rift was supported by two separate regions of upwelling magma occurring at upper mantle levels, which may have been connected in deeper mantle.

Comparisons with Samples of this Study

Figures 25 and 26 depict geochemical comparisons between the Main Ethiopian Rift, Afar Rift, and analyzed samples from the Arbuckle Mountains.

Samples from the Arbuckle Mountains appear similar to the samples from the Main Ethiopian and Afar Rifts, in most cases. The Arbuckle Mountains samples display an increase in K_2O and Zr concentrations with increasing silica, as is the case with samples from the Ethiopian Plateau, although more evolved samples from the Ethiopian Plateau contain higher concentrations of Zr, indicating regional variations in the source material between the Ethiopian Plateau and the Arbuckle Mountains. Both the Ethiopian Plateau and the Arbuckle Mountains mafic material display decreasing trends for MgO and Ni with increasing silica concentrations. Ethiopian Plateau samples, in most cases, have an order of magnitude more nickel than is present in the Arbuckle Mountains, which is likely caused by regional variations in nickel concentrations in the source magma.

Zr/Nb values are limited for this data to only the Afar Rift, due to the lack of Nb data in Hart et al (1989) for the MER and Afar Rift samples analyzed. The data for the Afar Rift displays two clusters of samples that indicate two separate magma sources. One of these groups ranges from two to seven, which is consistent with an EMI OIB source and the samples from the Arbuckle Mountains (Weaver, 1991). The second group exhibits Zr/Nb values that range from fifteen to thirty, consistent with normal mid-ocean ridge basalts coupled with upper crustal contamination. While the Ethiopian Plateau flood basalts are likely derived from two separate

mantle sources (Furman, 2007), the Arbuckle Mountains samples display consistent values from five to ten, indicating they are derived from a single EMI OIB mantle source.

The majority of values for K/Nb in the Ethiopian Plateau are similar to those of the Arbuckle Mountains, ranging from 300 to 600, indicative of an EMI OIB mantle source with some upper crustal contamination. However, some of the Ethiopian Plateau samples rise as high as 1,300, indicating a much higher level of upper crustal contamination in the East African Rift. The same pattern occurs with Ba/Th values. The East African Rift values primarily occur around 50 to 250, which is indicative of an EMI OIB magma source. Values in the Ethiopian Plateau, however, also rise to as high as 950 in the Afar Rift and as high as 750 in the Main Ethiopian Rift, indicating higher levels of upper crustal contamination. Values for K/P are very similar for the Arbuckle Mountains, MER, and Afar Rift. Evolved samples from the Arbuckle Mountains display higher K/P values than are present in the Ethiopian Plateau, but all three sets of samples show values over five, indicating the occurrence of upper crustal contamination.

The overall geochemical similarities between the samples from the Ethiopian Plateau and the Arbuckle Mountains support the hypothesis that the Arbuckle Mountains represent a flood basalt province that is consistent with the failed third arm of a triple junction. Both regions also contain large volumes of silicic volcanism; the major notable difference between the two locations is the varying magma sources for each location. The Ethiopian Plateau is derived from two separate magma sources (EMI OIB and MORB with upper crustal contamination), while the analyzed samples of the Arbuckle Mountains are derived from a single EMI OIB magma source with upper crustal contamination.

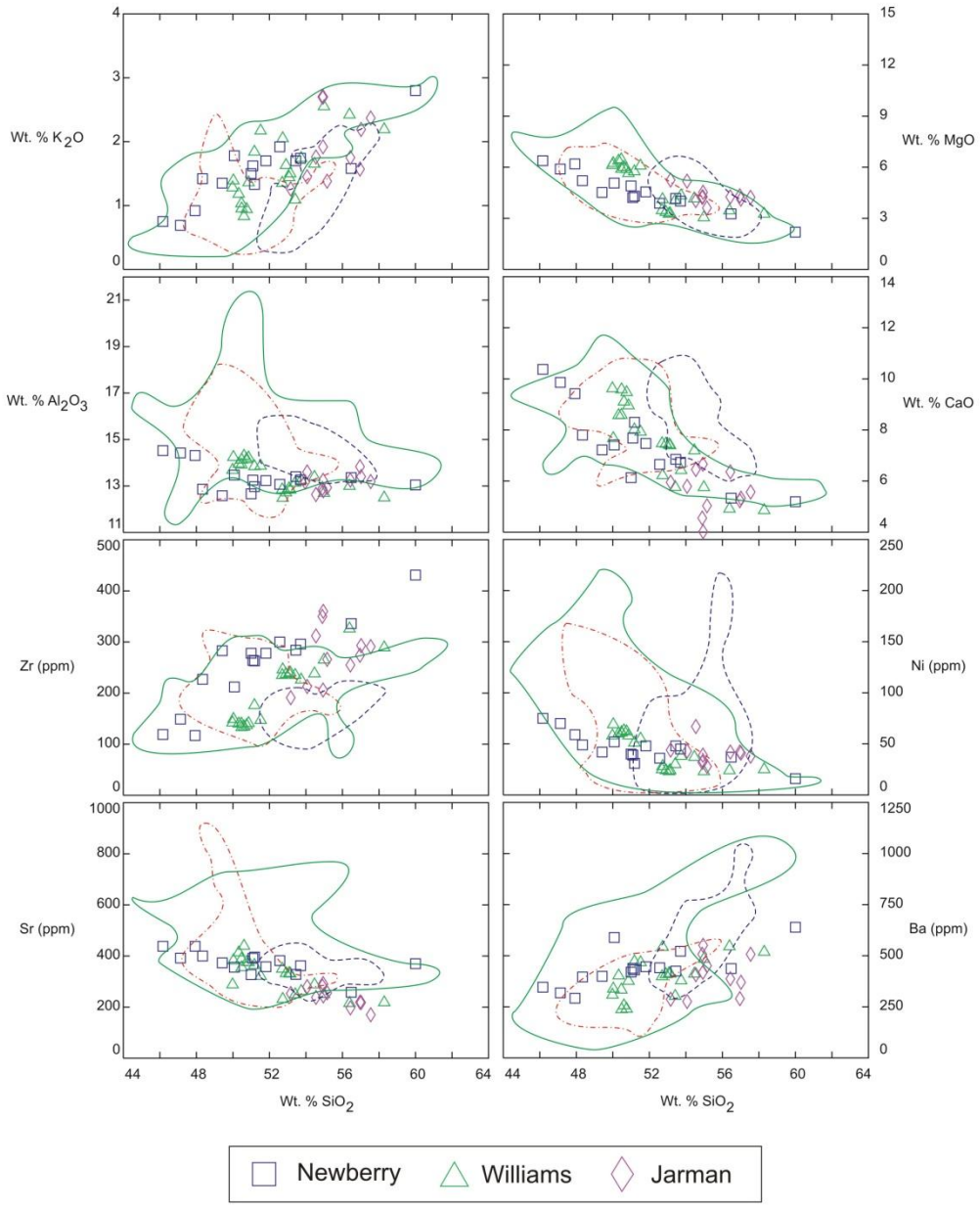

Figure 23: XY-diagrams showing major and trace element concentrations versus silica concentrations compared to those of the Columbia River-Steens Basalt Group. The field outlined in blue dashes represents data for the Grande Ronde Basalts in the Columbia River Plateau from Hooper (2000). The field outlined in dotted and dashed red represents data from the Imnaha Basalts in the Columbia River Plateau from Hooper (2000). The field outlined in solid green represents data for the Steens Basalts in the Oregon Plateau from Johnson et al (1998) and Brueseke et al (2007).

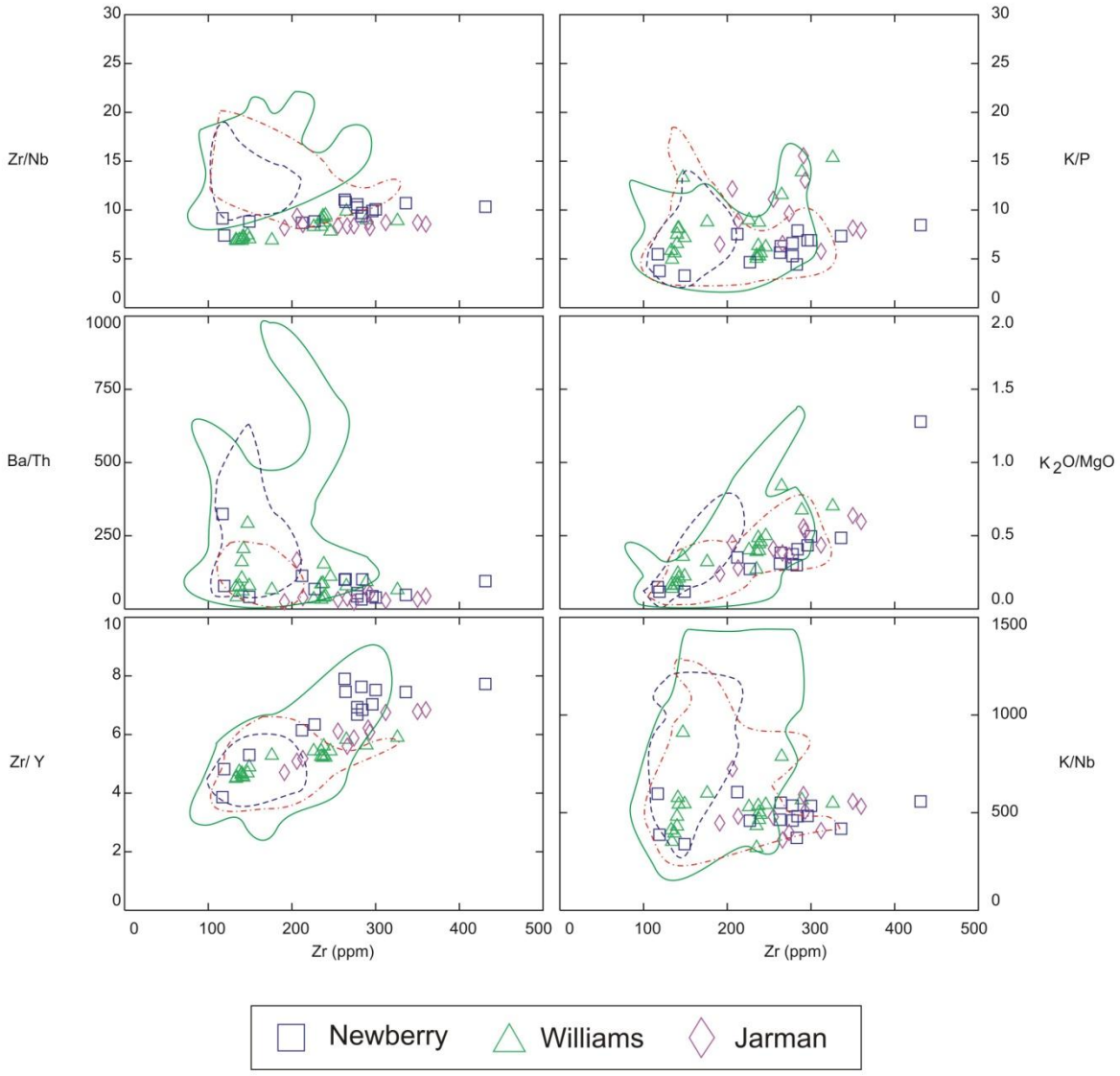

Figure 24: XY-diagrams showing incompatible trace element ratios versus zirconium concentrations compared to those of the Columbia River-Steens Basalt Group. The field outlined in blue dashes represents data for the Grande Ronde Basalts in the Columbia River Plateau from Hooper (2000). The field outlined in dotted and dashed red represents data from the Imnaha Basalts in the Columbia River Plateau from Hooper (2000). The field outlined in solid green represents data for the Steens Basalts in the Oregon Plateau from Johnson et al (1998) and Brueseke et al (2007).

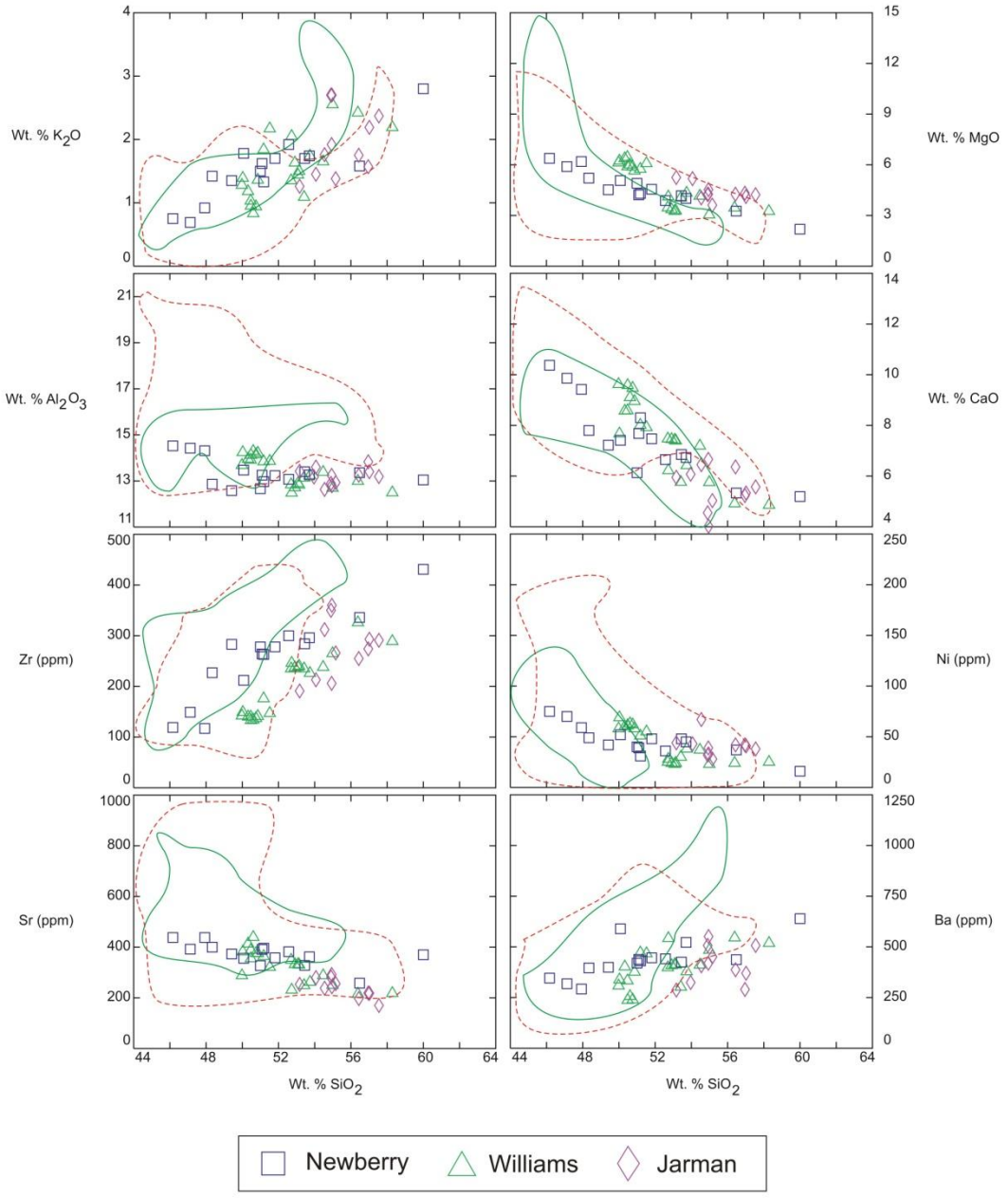

Figure 25: XY-diagrams showing major and trace element concentrations versus silica concentrations compared to those of the East African Rift System. The field outlined in solid green represents data for the Main Ethiopian Rift from Hart et al (1989), while the field outlined in red dashes represents data for the Afar Rift from Hart et al (1989) and Kieffer et al (2004).

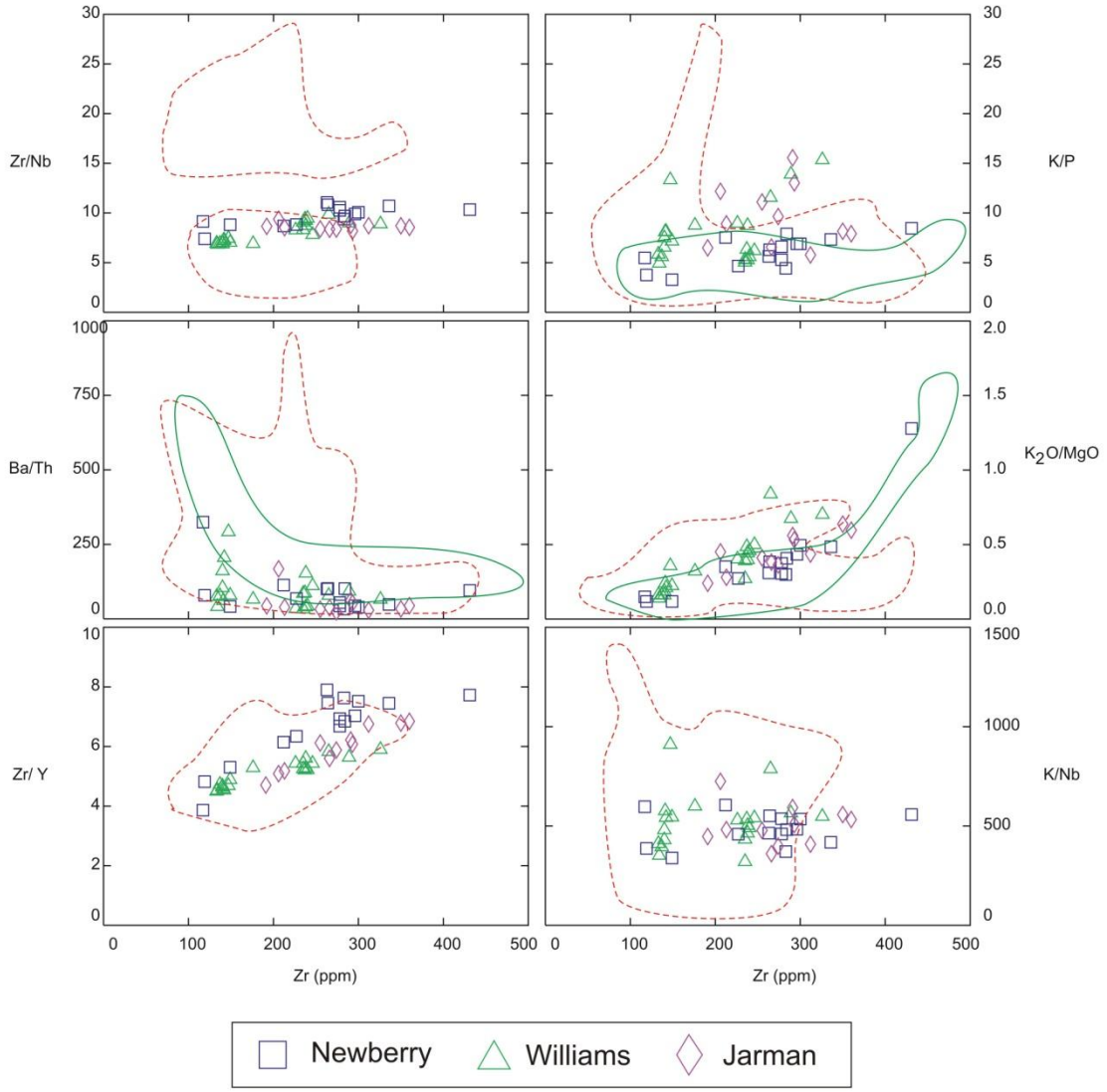

Figure 26: XY-diagrams showing incompatible trace element ratios versus zirconium concentrations compared to those of the East African Rift System. The field outlined in solid green represents data for the Main Ethiopian Rift from Hart et al (1989), while the field outlined in red dashes represents data for the Afar Rift from Hart et al (1989) and Kieffer et al (2004). Samples from Hart et al (1989) for the Main Ethiopian Rift do not have data for Nb concentrations.

Chapter 6 - **Summary**

The Arbuckle Mountains in southern Oklahoma are located in the eastern extent of the Southern Oklahoma Rift Zone, which stretches from southeastern Oklahoma into Texas, New Mexico, Colorado, and Utah. The Southern Oklahoma Rift Zone contains large volumes of bimodal basalt-rhyolite volcanism, including an estimated 210,000 km^3 of mafic lava flows in the Arbuckle Mountains, which extruded as a result of the break-up of Pannotia and the opening of the Iapetus Ocean forming the failed arm of a three-armed triple junction (Hanson et al, 2012).

Mafic lava flows present exclusively in the subsurface of the Arbuckle Mountains are tholeiitic basalts to andesites, typical of continental rift and flood basalt provinces. The chemostratigraphy of three wells from the Arbuckle Mountains reveal up to five possible lava flow packages. The deepest flow package (A) occurs 2550 meters below the surface in the Newberry well. Flow package B occurs between 2000 and 2100 meters below the surface and is present in both the Williams and Jarman. Flow package C occurs between 1850 and 1925 meters below the surface in the Williams well. Flow package D occurs between 1700 and 1850 meters in the Williams well. The shallowest flow package (E) occurs 1050 meters below the surface in the Jarman well. While flow packages B through D are clearly evident in the Williams well, more samples from flow package A and E may provide greater insight into the existence of these flow packages, as well as their vertical extents.

Geochemical comparisons between the samples from the Arbuckle Mountains and mafic rocks in the nearby Wichita Mountains reveal a likely connection between the Roosevelt Gabbros and the mafic samples from the Arbuckle Mountains; the Roosevelt Gabbros appear to represent the intrusive equivalent of the analyzed samples from this study. The Navajoe Mountain Basalt-Spilite Group appears to represent a similar lava flow package that is less evolved than the samples from the Arbuckle Mountains.

The samples from the Arbuckle Mountains contain geochemical traits that differ slightly from samples from the Columbia River, Oregon, and Ethiopian Plateaus, which provide first-order insights into the mantle sources and petrogenetic processes that affected the samples in this study. The Columbia River and Oregon Plateaus are a well-studied example of a flood basalt province in the United States, albeit with a still contentious origin; while the Ethiopian Plateau represents a flood basalt province originating due to the formation of a continental rift, plume

uplift, and triple junction. The presence of large volumes of bimodal basalt-rhyolite eruptive materials in these provinces, as well as in the Southern Oklahoma Rift Zone, is consistent with the interpretation that the Southern Oklahoma Rift Zone represents an additional flood basalt province in North America. Geochemical characteristics of analyzed samples from the Arbuckle Mountains reveal that the mafic lava flows of the Arbuckle Mountains and southern Oklahoma rift zone were derived from an EMI OIB mantle source coupled with crustal assimilation, that likely occurred when these magmas stalled out in the upper crust prior to eruption. This is notably different than the Ethiopian Plateau, where mafic magmas are sourced from two separate mantle sources (MORB with upper crustal contamination and EMI OIB), as well as the Columbia River and Oregon Plateaus, which originate from an OIB-like mantle source and also a depleted MORB source with significant amounts of crustal assimilation.

Chapter 7 - **Future Work**

Mafic rocks have been defined in multiple wells in the Arbuckle Mountains of southern Oklahoma, including the four mentioned in this study. Collection and geochemical analysis from additional wells located further away from the Newberry, Williams, and Jarman wells can provide a great insight into the lateral and vertical extent of mafic material in the subsurface of the Arbuckle Mountains, as well as provide further evidence for the existence of lava flow packages in these basalts and their stratigraphic locations. Samples from the Turner Falls well that were collected for this study are currently being examined to determine whether enough material is present to undergo major and trace element geochemical analysis.

Major and trace element geochemistry provides only a limited insight into the petrogenesis of the subsurface mafic lava flows present in the Arbuckle Mountains. As a result, radiogenic isotope data and rare earth element analysis will provide additional and more detailed insight into mantle sources and crustal interaction, as well as the petrogenesis of the mafic to intermediate rocks. Furthermore, obtaining geochronologic data from the interlayered silicic units can provide precise age constraints on the entire volcanic package present throughout the subsurface of the Arbuckle Mountains.

References

Aquilar, J., 1988, Geochemistry of Mafic Rock Units of the Southern Oklahoma Aulacogen, Southwestern Oklahoma: *University of Oklahoma unpublished M.S. thesis*, 167 p.

Barry, T.L., Self, S., Kelley, S.P., Reidel, S., Hooper, P., and Widdowson, M., 2010, New $^{40}Ar/^{39}Ar$ dating of the Grande Ronde lavas, Columbia River Basalts, USA: Implications for duration of flood basalt eruption episodes: *Lithos*, v. 118, no. 3-4, p. 213-222.

Basaltic Volcanism Study Project, 1981, Basaltic Volcanism on the Terrestrial Planets, Pergamon Press, Inc., New York, 1288 p.

Beswick, A.E. and Soucie, G., 1978, A correction procedure for metasomatism in an Archean greenstone belt: *Precambrian Research*, v. 6, p. 235-248.

Bickford, M.E., and Lewis, R.D., 1979, U-Pb geochronology of exposed basement rocks in Oklahoma: *Geological Society of America Bulletin*, v. 90, p. 540-544.

Bondre, N.R. and Hart, W.K., 2008, Morphological and textural diversity of the Steens Basalt lava flows, Southeastern Oregon, USA: implications for emplacement style and nature of eruptive episodes: *Bulletin of Volcanology*, v. 70, p. 999-1019.

Borchardt, G.A., Harward, M.E., and Schmitt, R.A., 1971, Correlation of Volcanic Ash Deposits by Activation Analysis of Glass Separates: *Quarternary Research*, v. 1, p. 247-260.

Borchardt, G.A., Aruscavage, P.J., and Millard, Jr., H.T., 1972, Correlation of the Bishop Ash, A Pleistocene Marker Bed, Using Instrumental Neutron Activation Analysis: *Journal of Sedimentary Petrology*, v. 42, no. 2, p. 301-306.

Brueseke, M.E., Heizler, M.T., Hart, W.K., and Mertzman S.A., 2007, Distribution and geochronology of Oregon Plateau (U.S.A.) flood basalt volcanism: The Steens Basalt revisited: *Journal of Volcanology and Geochemical Research*, v. 161, p. 187-214.

Cameron, M., Weaver, B.L., and Diez de Medina, D., 1986, A Preliminary Report on Trace Element Geochemistry of Mafic Igneous Rocks of the Southern Oklahoma Aulacogen *in* Gilbert, M.C., 1986, Petrology of the Cambrian Wichita Mountains Igneous Suite: *Oklahoma Geological Survey Guidebook*, v. 23, p. 80-85.

Carlson, R.W. and Hart, W.K., 1987, Crustal Genesis on the Oregon Plateau: *Journal of Geophysical Research*, v. 92, no. B7, p. 6191-6206.

Cross, W., Iddings, J.P., Pirsson, L.V., and Washington, H.S., 1902, A quantitative chemico-mineralogical classification and nomenclature of igneous rocks: *Journal of Geology*, v. 10, p. 555-690.

DeGroat, P.J., Donovan, R.N., Hanson, R.E., and Weaver, B.L., 1995, Cambrian Diabase and Gabbro in the Blue Creek Canyon Area, Wichita Mountains, Southwestern Oklahoma: *Oklahoma Geology Notes*, v. 55, n. 5, p. 168-186.

Denison, R.E., 1995, Significance of air-photograph linears in basement rocks of the Arbuckle Mountains *in* Johnson, K.S. (eds), Structural styles in the southern Midcontinent, 1992 symposium: *Oklahoma Geological Survey Circular*, v. 97, p. 119-131.

Diez de Medina, D.M., 1988, Geochemistry of the Sandy Creek gabbro, Wichita Mountains, Oklahoma: *University of Oklahoma unpublished M.S. thesis*, 163 p.

Floyd, P.A. and Winchester, T.A., 1975, Magma type and tectonic setting discrimination using immobile elements: *Earth and Planetary Science Letters*, v. 27, no. 2, p. 211-218.

Furman, T., 2007, Geochemistry of East African Rift basalts: An overview: *Journal of African Earth Sciences*, v. 48, p. 147-160.

Gilbert, M.C. and Hughes, S.S., 1986, Partial Chemical Characterization of Cambrian Basaltic Liquids of the Southern Oklahoma Aulacogen *in* Gilbert, M.C., 1986, Petrology of the Cambrian Wichita Mountains Igneous Suite: *Oklahoma Geological Survey Guidebook*, v. 23, p. 73-79.

Greeley, R., 1982, The Snake River Plain, Idaho: Representative of a new category of volcanism: *Journal of Geophysical Research*, v. 87, p. 2705-2712.

Gunn, B.M. and Watkins, N.D., 1970, Geochemistry of the Steens Mountain Basalts, Oregon: *Geological Society of America Bulletin*, v. 81, p. 1497-1516.

Ham, W.E. and McKinley, M.E., Geologic Map and Sections of the Arbuckle Mountains, Oklahoma [map], 1:100,000. Revised 1990. Norman, Oklahoma: University of Oklahoma, Oklahoma Geological Survey, 1954.

Ham, W.E., Denison, R.E., and Merritt, C.A., 1965, Basement Rocks and Structural Evolution of Southern Oklahoma – A Summary: *Bulletin of the AAPG*, v. 49, n. 7, p. 927-934.

Hanson, R.E. and Al-Shaieb, Z., 1980, Voluminous subalkaline silicic magmas related to intracontinental rifting in the southern Oklahoma aulacogen: *Geology*, v. 8, p. 180-184.

Hanson, R.E., Puckett Jr., R.E., Keller, G.R., Brueseke, M.E., Bulen, C.L., Mertzman, S.A., Finegan, S.A., and McCleery, D.A., Intraplate magmatism related to opening of the southern Iapetus Ocean: Cambrian Wichita igneous province in the Southern Oklahoma rift zone: *Lithos (2012)*, doi: 10.1016/j.lithos.2012.06.003.

Hart, W.K., Carlson, R.W., and Mosher, S.A., 1989, Petrogenesis of the Pueblo Mountains basalt, southeastern Oregon and northern Nevada *in* Reidel, S.P. and Hooper, P.R (*eds*), Volcanism and tectonism in the Columbia River flood-basalt province: *Geological Society of America Special Paper*, v. 139, p. 367-378.

Hart, W.K., WoldeGabriel, G., Walter, R.C., and Mertzman, S.A., 1989, Basaltic Volcanism in Ethiopia: Constraints on Continental Rifting and Mantle Interactions: *Journal of Geophysical Research*, v. 94, no. B6, p. 7731-7748.

Hoffman, P., Dewey, J.F., and Burke, K., 1974, Aulacogens and their Genetic Relation to Geosynclines, with a Proterozoic Example from Great Slave Lake, Canada *in* Dott Jr, R.H. and Shaver, R.H., 1974, Modern and Ancient Geosynclinal Sedimentation: *SEPM Special Publication*, v. 19, p. 38-55.

Hooper, P.R., 2000, Chemical discrimination of Columbia River basalt flows: *Geochemistry, Geophysics, Geosystems*, v. 1, no. 1, p. 1024-1038.

Hooper, P.R., Camp, V.E., Reidel, S.P., and Ross, M.E., 2007, The origin of the Columbia River flood basalt province: Plume versus nonplume models: *in* Foulger, G.R. and Jurdy, D.M.

(*eds*), Plates, plumes, and planetary processes: *The Geological Society of America Special Paper 430*, p. 635-668.

Hughes, S.S., Smith, R.P., Hackett, W.R., and Anderson, S.R., 1999, Mafic Volcanism and Environmental Geology of the Eastern Snake River Plain, Idaho *in* Hughes, S.S. and Thackray, G.D. (*eds*), Guidebook to the Geology of Eastern Idaho: *Idaho Museum of Natural History*, p. 143-168.

Irvine, T.N. and Baragar, W.R.A., 1971, A Guide to the Chemical Classification of the Common Volcanic Rocks: *Canadian Journal of Earth Sciences*, v. 8, no. 5, p. 523-548.

Johnson, J.A., Hawkesworth, C.J., Hooper, C.J., and Binger, P.R., 1998, Major- and trace-element analyses of Steens Basalt, Southern Oregon: *U.S. Geological Survey Open File Report*, v. 98-482, p. 30.

Keller, G.R. and Stephenson, R.A., 2007, The Southern Oklahoma and Dniepr-Donets aulacogens: A comparative analysis, *in* Hatcher, R.D., Jr., Carlson, M.P., McBride, J.H., and Martinez Catalan, J.R. (eds.), 4-D Framework of Continental Crust: *Geological Society of America Memoir*, v. 200, p. 127-143.

Kieffer, B., Arndt, N., LaPierre, H., Bastien, F., Bosch, D., Pecher, A., Yirgu, G., Ayalew, D., Weis, D., Jerram, D.A., Keller, F., and Meugniot, C., 2004, Flood and Shield Basalts from Ethiopia: Magmas from the African Superswell: *Journal of Petrology*, v. 45, no. 4, p. 793-834.

Larson, E.E., Patterson, P.E., Curtis, G., Drake, R., and Mutschler, F.E., 1985, Petrologic, paleomagnetic, and structural evidence of a Paleozoic rift system, in Oklahoma, New Mexico, Colorado, and Utah: *Geological Society of America Bulletin*, v. 96, p. 1364-1372.

Le Bas, M.J., Le Maitre, R.W., Streckeiser, A., and Zanettin, B., 1986, Chemical classification of volcanic rocks based on total alkali-silica diagram: *Journal of Petrology*, v. 27, no. 3, p. 745-750.

McConnell, D.A. and Gilbert, M.C., 1990, Cambrian extensional tectonics and magmatism within the Southern Oklahoma Aulacogen *in* Lucchitta, I. and Morgan, P. (eds.), Heat and Detachment in Continental Extension: *Tectonophysics*, v. 174, p. 147-157.

Mertzman, S.A., 2000, K-Ar results from the southern Oregon-northern California Cascade Range: *Oregon Geology*, v. 62, no. 4, p. 99-122.

Mertzman, S.A., 2012, X-ray Laboratory. In *Franklin & Marshall College Department of Earth and Environment*. Retrieved 2012, from http://www.fandm.edu/earth-and-environment/x-ray-laboratory.

Meschede, M., 1986, A method of discriminating between different types of mid-ocean ridge basalts and continental tholeiites with the Nb-Zr-Y diagram: *Chemical Geology*, v. 56, no. 3-4, p. 207-218.

Miyashiro, A., 1974, Volcanic rock series in island arcs and active continental margins: *American Journal of Science*, v. 274, p. 321-355.

Mullen, E.D., 1983, $MnO/TiO_2/P_2O_5$: a minor element discriminant for basaltic rocks of oceanic environments and its implications for petrogenesis: *Earth and Planetary Science Letters*, v. 62, no. 1, p. 53-62.

Pearce, J.A. and Cann, J.R., 1973, Tectonic setting of basic volcanic rocks determined using trace element analyses: *Earth and Planetary Science Letters*, v. 19, no. 2, p. 290-300.

Powell, B.N. and Phelps, D.W., 1977, Igneous cumulates of the Wichita province and their tectonic implications: *Geology*, v. 5, p. 52-56.

Puckett, R.E., 2012, A thick sequence of rift-related basalts in the Arbuckle Mountains, Oklahoma, as revealed by deep drilling: *Shale Shaker*, Jan/Feb 2011, p. 207-216.

Rudnick, R.L. and Gao, S., 2003, Composition of the Continental Crust *in* Holland, H.D. and Turekian, K.K. (eds), Treatise on Geochemistry, v. 3, no. 1, p. 1-64.

Scofield, N., 1975, Layered Series of the Wichita Complex, Oklahoma: *Geological Society of America Bulletin*, v. 86, p. 732-736.

Scotese, C.R., 2009, Late Proterozoic plate tectonics and palaeogeography: a tale of two supercontinents, Rodinia and Pannotia *in* Craig, J, Thurow, J, Thusu, B, Whitham, A, and Abutarruna, Y (eds), Global Neoproterozoic Petroleum Systems: The Emerging Potential in North Africa: *Geological Society of London Special Publications*, v. 326, p. 67-83.

Shapiro, B.E., 1981, Chemistry and Petrography of the Navajoe Mountain Basalt Spillites of Southern Oklahoma: *University of Texas at Arlington unpublished M.S. thesis*, 116 p.

Shervais, J.W., Vetter, S.K., and Hanan B.B., 2006, Layered mafic sill complex beneath the eastern Snake River Plain: Evidence from cyclic geochemical variations in basalt: *Geology*, v. 34, no. 5, p. 365-368.

Skulski, T., Francis, D., and Ludden, J., 1991, Arc-transform magmatism in the Wrangell volcanic belt: *Geology*, v. 19, p. 11-14.

Skulski, T., Francis, D., and Ludden, J., 1992, Volcanism in an arc-transform transition zone: the stratigraphy of the St. Clare Creek volcanic field, Wrangell volcanic belt, Yukon, Canada: *Canadian Journal of Earth Sciences*, v. 29, p. 446-461.

Thomas, W.A., 2006, Tectonic inheritance at a continental margin: *GSA Today*, v. 16, no. 2, p. 4-11.

Thomas, W.A., 2011, The Iapetan rifted margin of Southern Laurentia: *Geosphere*, February 2011, v. 7, no.2, p. 97-120.

Thompson, R.N., Morrison, M.A., Dickin, A.P., and Hendry, G.L., 1983, Continental Flood Basalts…Arachnids Rule OK? *in* Hawkesworth, C.J. and Norry, M.J. (eds.), Continental Basalts and Mantle Xenoliths: *Shiva*, p. 158-185.

Walker, J.A., Pippin, C.G., Cameron, B.I., Patino, L, 2002, Tectonic insights provided by Mesoproterozoic mafic rocks of the St. Francois Mountains, southeastern Missouri: *Precambrian Research*, v. 117, p. 251-268.

Weaver, B.L., 1991, The origin of ocean island basalt end-member compositions: trace element and isotopic constraints: *Earth and Planetary Science Letters*, v. 104, p. 381-397.

Winchester, T.A. and Floyd, P.A., 1977, Geochemical discrimination of different magma series and their differentiation products using immobile elements: *Chemical Geology*, v. 20, p. 325-343.

Appendix A - Arbuckle Mountains Samples

Samples collected from the Oklahoma Petroleum Information Center operated by the Oklahoma Geological Survey in Norman, Oklahoma are shown in the table below. Samples that contain a "-" symbol in the "Analyzed Weight (g)" column were not analyzed. These samples were removed from analysis due to high levels of visible contamination (e.g. very heterogeneous sample where hand-picking would be impossible) or alteration leading to less than 10 g of sample being available to analyze, or due to smaller grain sizes that made preparing the samples for accurate geochemical analyses difficult. Samples with an "*" contained high amounts of alteration and were excluded from the interpretations in this study.

Sample	Well	Amount Collected (g)	Analyzed Weight (g)	Depth (ft)	Depth (m)
CB-PAW-1	Williams	21.00	16.3190	5600-5650	1706.88-1722.12
CB-PAW-2	Williams	17.00	14.9944	5650-5700	1722.12-1737.36
CB-PAW-3	Williams	20.00	16.7700	5700-5750	1737.36-1752.60
CB-PAW-4	Williams	17.00	14.3427	5750-5780	1752.60-1761.74
CB-PAW-5	Williams	21.00	17.4843	5800-5850	1767.84-1783.08
CB-PAW-6	Williams	22.00	15.9653	5850-5900	1783.08-1798.32
CB-PAW-7	Williams	21.00	17.2385	5900-5950	1798.32-1813.56
CB-PAW-8	Williams	21.00	17.0142	5950-6000	1813.56-1828.80
CB-PAW-9	Williams	17.00	14.6001	6000-6050	1828.80-1844.04
CB-PAW-10	Williams	21.00	14.9573	6050-6100	1844.04-1859.28
CB-PAW-11	Williams	20.00	14.2409	6100-6150	1859.28-1874.52
CB-PAW-12	Williams	21.00	15.0798	6150-6200	1974.52-1889.76
CB-PAW-13	Williams	18.00	13.3783	6200-6250	1889.76-1905.00
CB-PAW-14	Williams	21.00	16.3847	6250-6300	1905.00-1920.24
CB-PAW-15	Williams	22.00	15.6596	6300-6350	1920.24-1935.48
CB-PAW-16	Williams	22.00	13.1114	6600-6650	2011.68-2026.92
CB-PAW-17	Williams	21.00	15.3981	6650-6700	2026.92-2042.16
CB-PAW-18	Williams	21.00	13.3473	6700-6750	2042.16-2057.40
CB-PAW-19	Williams	20.00	14.3571	6750-6800	2057.40-2072.64
CB-PAW-20	Williams	20.00	15.0173	6800-6850	2072.64-2087.88
CB-PAW-21	Williams	18.00	13.2271	6850-6900	2087.88-2103.12
CB-PAN-1	Newberry	17.00	-	1910-1950	582.17-594.36
CB-PAN-2	Newberry	16.00	-	1950-2000	594.36-609.60
CB-PAN-3	Newberry	17.00	-	2000-2050	609.60-624.84
CB-PAN-4	Newberry	17.00	-	2650-2700	807.72-822.96
CB-PAN-5	Newberry	17.00	14.9966	3250-3300	990.60-1005.84
CB-PAN-6	Newberry	17.00	10.4506	4100-4150	1249.68-1264.92
CB-PAN-7	Newberry	17.00	10.1620	4150-4200	1264.92-1280.16
CB-PAN-8	Newberry	17.00	11.1054	4200-4250	1280.16-1295.40
CB-PAN-9	Newberry	17.00	10.9267	4250-4300	1295.40-1310.64

Sample	Well	Amount Collected (g)	Analyzed Weight (g)	Depth (ft)	Depth (m)
CB-PAN-10	Newberry	17.00	-	4550-4600	1386.84-1402.08
CB-PAN-11	Newberry	17.00	-	4600-4650	1402.08-1417.32
CB-PAN-12	Newberry	17.00	12.6393	4650-4700	1417.32-1432.56
CB-PAN-13	Newberry	18.00	13.9964	4700-4750	1432.56-1447.80
CB-PAN-14	Newberry	17.00	10.8552	4750-4800	1447.80-1463.04
CB-PAN-15	Newberry	17.00	13.2124	4800-4850	1463.04-1478.28
CB-PAN-16	Newberry	17.00	12.7181	4850-4900	1478.28-1493.52
CB-PAN-17	Newberry	17.00	11.7596	5100-5150	1554.48-1569.72
CB-PAN-18	Newberry	18.00	14.3230	5800-5850	1767.84-1783.08
CB-PAN-19	Newberry	16.00	11.4959	5900-5950	1798.32-1813.56
CB-PAN-20	Newberry	17.00	15.9467	8300-8350	2529.84-2545.08
CB-PAN-21	Newberry	21.00	16.1022	8350-8400	2545.08-2560.32
CB-PAN-22	Newberry	19.00	-	10,450-10,500	3185.16-3200.40
CB-PAN-23	Newberry	15.00	-	10,650-10,700	3246.12-3261.36
CB-PAJ-1	Jarman	18.00	-	3350-3400	1021.08-1036.32
CB-PAJ-2	Jarman	15.00	11.3063	3400-3450	1036.32-1051.56
CB-PAJ-3	Jarman	16.00	-	3450-3500	1051.56-1066.80
CB-PAJ-4	Jarman	17.00	12.9741	3500-3550	1066.80-1082.04
CB-PAJ-5	Jarman	16.00	-	3550-3600	1082.04-1097.28
CB-PAJ-6	Jarman	17.00	13.2516	3600-3650	1097.28-1112.52
CB-PAJ-7	Jarman	17.00	12.2396	5350-5400	1630.68-1645.92
CB-PAJ-8	Jarman	16.00	13.4692	5400-5450	1645.92-1661.16
CB-PAJ-9	Jarman	16.00	12.4763	5450-5500	1661.16-1676.40
CB-PAJ-10	Jarman	17.00	13.1791	5500-5550	1676-40-1691.64
CB-PAJ-11	Jarman	17.00	14.6107	5550-5600	1691.64-1706.88
CB-PAJ-12	Jarman	15.00	-	6550-6600	1996.44-2011.68
CB-PAJ-13	Jarman	18.00	13.3425	6600-6650	2011.68-2026.92
CB-PAJ-14	Jarman	17.00	-	6650-6700	2026.92-2042.16
CB-PAJ-15	Jarman	17.00	13.4938	6700-6750	2042.16-2057.40
CB-PAJ-16	Jarman	17.00	14.0411	6750-6800	2057.40-2072.64
CB-PAJ-17*	Jarman	17.00	14.7024	6800-6850	2072.64-2087.88
CB-TF-1	Turner Falls	20.00	-	13,200-13,300	4023.36-4053.84
CB-TF-2	Turner Falls	20.00	-	13,300-13,500	4053.84-4114.80
CB-TF-3	Turner Falls	20.00	-	13,500-13,610	4114.80-4148.33
CB-TF-4	Turner Falls	20.00	-	13,610-13,620	4148.33-4151.38
CB-TF-5	Turner Falls	22.00	-	13,620-13,630	4151.38-4154.42
CB-TF-6	Turner Falls	22.00	-	13,630-13,640	4154.42-4157.47
CB-TF-7	Turner Falls	20.00	-	13,620-13,700	4151.38-4175.76
CB-TF-8	Turner Falls	20.00	-	13,700-13,900	4175.76-4236.72
CB-TF-9	Turner Falls	20.00	-	13,900-13,910	4236.72-4239.77
CB-TF-10	Turner Falls	22.00	-	13,910-13,930	4239.77-4245.86
CB-TF-11	Turner Falls	20.00	-	13,930-13,950	4245.86-4251.96
CB-TF-12	Turner Falls	17.00	-	13,950-13,970	4251.96-4258.06
CB-TF-13	Turner Falls	17.00	-	13,970-14,000	4258.06-4267.20
CB-TF-14	Turner Falls	24.00	-	14,000-14,270	4267.20-4349.50
CB-TF-15	Turner Falls	17.00	-	14,270-14,290	4349.50-4355.60

Appendix B - Major and Trace Element Geochemistry

Major and trace element geochemistry was determined using XRF analysis at Franklin and Marshall College. Major element concentrations are given in weight percent, while trace element concentrations are given in parts per million. Techniques for XRF analysis are described above and in Mertzman et al (2000).

	CB-PAW-1	CB-PAW-2	CB-PAW-3	CB-PAW-4	CB-PAW-5	CB-PAW-6
SiO_2	50.03	50.61	50.76	50.48	50.86	49.98
TiO_2	2.50	2.20	2.15	2.12	2.09	2.05
Al_2O_3	14.24	14.29	14.14	14.12	14.21	13.68
Fe_2O_3	5.00	4.56	4.56	4.54	4.51	4.64
FeO	7.80	7.51	7.60	7.70	7.09	7.57
MnO	0.26	0.25	0.24	0.23	0.23	0.22
MgO	6.23	6.00	5.88	5.89	5.64	6.12
CaO	7.67	9.10	9.47	9.58	8.95	9.62
Na_2O	3.63	3.51	3.23	3.10	3.41	3.27
K_2O	1.39	0.83	0.94	0.95	1.36	1.28
P_2O_5	0.37	0.32	0.32	0.31	0.32	0.30
Total	99.12	99.18	99.29	99.02	98.67	98.73
LOI	3.66	4.84	5.04	5.10	4.32	4.57
Ba	338	256	239	237	376	308
Ce	29	29	32	31	34	33
Co	51	49	48	49	45	46
Cr	121	110	103	95	112	94
Cu	111	140	130	131	118	127
Ga	15.4	14.7	15.1	14.6	14.7	14.8
La	12	11	13	12	11	13
Nb	21.2	19.6	19.8	19.2	19.6	19.6
Ni	69	63	62	61	58	58
Pb	14	19	6	8	3	10
Rb	25.3	12.7	14.1	14.1	17.4	16.2
Sc	36	38	38	39	36	37
Sr	382	439	376	355	375	288
Th	4.3	6.3	3.1	3.2	6.2	1.5
U	0.5	1.4	2.6	0.5	0.7	0.5
V	340	343	336	324	329	315
Y	30.5	29.6	29.0	29.6	30.8	31.3
Zn	122	115	112	103	105	101
Zr	149	134	137	133	141	142

	CB-PAW-7	CB-PAW-8	CB-PAW-9	CB-PAW-10	CB-PAW-11	CB-PAW-12
SiO_2	50.47	50.32	51.18	51.52	52.70	52.91
TiO_2	2.20	2.15	2.22	1.97	2.29	2.26
Al_2O_3	13.91	13.95	13.84	13.86	12.84	12.71
Fe_2O_3	4.81	4.81	4.87	4.75	5.86	5.86
FeO	7.67	7.61	7.31	6.96	9.02	8.96
MnO	0.23	0.23	0.23	0.21	0.25	0.25
MgO	6.45	6.37	5.74	6.08	3.46	3.36
CaO	8.58	8.57	8.01	7.92	7.47	7.45
Na_2O	3.68	3.63	3.38	3.24	3.31	3.07
K_2O	1.03	1.18	1.84	2.17	1.35	1.63
P_2O_5	0.30	0.30	0.40	0.31	0.51	0.49
Total	99.33	99.12	99.03	98.99	99.06	98.95
LOI	3.59	3.74	3.77	4.44	1.49	1.29
Ba	333	402	471	467	398	408
Ce	34	32	37	37	48	43
Co	50	49	46	46	50	47
Cr	93	100	76	84	31	19
Cu	132	135	96	100	121	106
Ga	15.1	14.8	14.7	14.7	17.7	17.5
La	13	11	18	12	19	20
Nb	19.9	20.4	25.5	19.8	25.9	25.3
Ni	61	60	51	55	25	24
Pb	6	3	4	1	7	10
Rb	13.8	15.1	25.0	27.0	31.4	28.1
Sc	38	37	35	35	38	37
Sr	388	413	364	321	349	332
Th	3.2	2.5	7.2	1.6	4.7	4.7
U	0.9	0.7	0.5	1.9	1.5	0.5
V	336	325	318	308	287	295
Y	30.0	30.2	33.3	31.4	43.3	45.5
Zn	104	103	103	102	135	133
Zr	140	140	176	147	235	237

	CB-PAW-13	CB-PAW-14	CB-PAW-15	CB-PAW-16	CB-PAW-17	CB-PAW-18
SiO_2	53.08	53.14	54.99	56.39	52.73	58.29
TiO_2	2.32	2.29	2.15	1.85	2.49	1.69
Al_2O_3	12.89	12.83	12.69	12.99	12.48	12.49
Fe_2O_3	5.83	5.96	6.08	5.86	5.80	5.36
FeO	8.98	8.95	8.05	7.69	8.29	6.82
MnO	0.24	0.24	0.23	0.21	0.26	0.21
MgO	3.25	3.28	3.04	3.45	4.11	3.25
CaO	7.42	7.39	5.75	4.91	6.22	4.85
Na_2O	3.13	3.34	3.33	3.29	3.41	3.52
K_2O	1.44	1.50	2.55	2.42	2.05	2.19
P_2O_5	0.52	0.51	0.42	0.30	0.63	0.30
Total	99.10	99.42	99.27	99.35	98.48	98.97
LOI	1.25	1.19	1.13	2.06	2.14	2.10
Ba	413	411	484	545	542	518
Ce	49	46	54	77	49	70
Co	50	48	46	47	50	43
Cr	20	21	21	26	29	21
Cu	107	106	106	86	84	96
Ga	18.3	17.2	17.2	18.2	16.3	17.4
La	20	21	22	29	20	26
Nb	25.8	25.4	26.9	36.7	31.5	32.2
Ni	23	24	23	24	28	25
Pb	7	1	2	20	15	15
Rb	26.6	25.4	52.3	40.4	31.2	37.3
Sc	36	36	34	33	36	30
Sr	332	330	250	215	231	218
Th	2.7	9.7	6.2	8.4	4.9	5.6
U	0.5	0.5	0.5	1.0	0.5	2.4
V	275	278	265	251	287	251
Y	45.1	46.0	45.5	55.3	45.3	51.3
Zn	135	131	125	214	184	170
Zr	238	240	265	326	246	289

	CB-PAW-19	CB-PAW-20	CB-PAW-21	CB-PAN-5	CB-PAN-6	CB-PAN-7
SiO_2	53.74	54.47	53.42	51.19	51.10	53.71
TiO_2	2.10	1.99	2.11	3.45	3.26	2.73
Al_2O_3	13.24	13.38	13.13	12.97	13.25	13.26
Fe_2O_3	5.50	5.30	6.00	5.26	5.39	5.21
FeO	7.81	7.59	8.47	8.75	8.55	7.56
MnO	0.23	0.22	0.22	0.20	0.21	0.20
MgO	4.33	4.15	4.04	4.30	4.22	4.01
CaO	6.42	7.19	5.76	8.20	7.68	6.73
Na_2O	3.59	3.46	4.37	2.78	3.02	3.37
K_2O	1.74	1.65	1.09	1.33	1.62	1.74
P_2O_5	0.37	0.36	0.39	0.45	0.49	0.48
Total	99.07	99.76	99.00	98.98	98.79	99.01
LOI	2.64	3.38	3.10	0.88	1.66	2.18
Ba	378	411	302	431	438	522
Ce	49	48	50	20	25	40
Co	48	45	52	48	45	42
Cr	58	49	27	39	42	72
Cu	109	104	127	123	133	121
Ga	16.8	16.7	17.8	18.5	18.7	18.4
La	20	21	22	13	13	18
Nb	27.3	27.3	28.3	23.8	24.4	29.9
Ni	38	37	30	31	39	45
Pb	10	4	2	11	1	10
Rb	31.5	27.0	20.8	19.3	28.3	29.2
Sc	34	33	34	34	31	29
Sr	262	288	249	396	391	362
Th	11.3	10.4	9.3	4.3	4.3	11.9
U	0.9	1.3	1.4	1.1	1.3	0.5
V	284	277	320	391	357	295
Y	41.6	42.5	44.8	33.3	35.4	42.1
Zn	151	150	164	127	128	124
Zr	226	238	235	263	264	296

	CB-PAN-8	CB-PAN-9	CB-PAN-12	CB-PAN-13	CB-PAN-14	CB-PAN-15
SiO_2	53.45	51.81	48.34	49.42	56.48	52.57
TiO_2	2.63	3.03	3.50	3.84	2.61	3.23
Al_2O_3	13.40	13.23	12.86	12.58	13.36	13.07
Fe_2O_3	5.01	5.23	5.68	5.85	5.07	5.39
FeO	7.46	8.20	9.43	9.39	6.58	7.89
MnO	0.20	0.20	0.23	0.23	0.17	0.21
MgO	4.17	4.55	5.21	4.52	3.26	3.88
CaO	6.85	7.47	7.80	7.22	5.33	6.65
Na_2O	3.17	2.93	3.26	3.48	4.25	3.32
K_2O	1.70	1.70	1.42	1.35	1.58	1.92
P_2O_5	0.41	0.49	0.58	0.58	0.41	0.53
Total	98.45	98.85	98.31	98.46	99.10	98.66
LOI	2.50	2.21	2.11	1.77	3.69	2.26
Ba	425	446	396	399	437	441
Ce	36	30	21	15	41	27
Co	43	47	53	50	38	43
Cr	89	108	82	71	49	79
Cu	132	157	139	181	111	146
Ga	19.3	18.0	17.0	17.9	20.8	18.1
La	18	14	11	11	24	16
Nb	29.3	26.3	25.7	30.2	31.4	29.8
Ni	48	48	49	42	37	36
Pb	1	2	1	5	1	2
Rb	27.7	28.5	24.4	20.5	25.1	34.2
Sc	29	32	38	34	27	29
Sr	328	358	400	373	258	382
Th	4.2	10.3	5.8	12.2	9.1	11.3
U	1.2	1.7	3.2	0.5	0.5	2.3
V	298	358	385	397	263	227
Y	41.5	40.1	35.8	37.1	45.1	39.9
Zn	127	126	127	135	129	130
Zr	284	278	227	283	336	300

	CB-PAN-16	CB-PAN-17	CB-PAN-18	CB-PAN-19	CB-PAN-20	CB-PAN-21
SiO_2	60.00	51.00	47.93	50.08	46.17	47.13
TiO_2	2.18	3.70	2.26	2.98	2.90	2.97
Al_2O_3	13.04	12.66	14.31	13.47	14.52	14.42
Fe_2O_3	4.38	5.83	5.12	5.42	4.77	4.87
FeO	5.17	9.49	9.48	8.50	9.44	9.31
MnO	0.18	0.24	0.23	0.23	0.23	0.23
MgO	2.19	4.90	6.19	5.07	6.38	5.89
CaO	5.19	6.13	9.42	7.41	10.37	9.86
Na_2O	3.40	2.88	2.69	3.18	2.52	2.75
K_2O	2.80	1.50	0.92	1.78	0.75	0.69
P_2O_5	0.63	0.54	0.32	0.45	0.38	0.40
Total	99.15	98.86	98.87	98.57	98.43	98.52
LOI	1.88	3.28	2.30	2.71	2.44	3.18
Ba	639	420	292	589	346	318
Ce	67	22	27	29	20	25
Co	25	52	57	49	56	52
Cr	17	63	80	93	111	104
Cu	34	210	134	135	87	103
Ga	20.2	18.4	16.7	17.7	17.0	17.5
La	33	13	10	13	9	12
Nb	41.7	27.1	12.8	24.4	16.1	16.9
Ni	16	40	59	52	75	70
Pb	1	3	1	6	3	1
Rb	52.2	26.4	16.7	34.4	13.0	12.1
Sc	21	34	45	34	40	37
Sr	370	327	438	356	438	392
Th	6.7	7.7	0.9	5.2	4.4	7.7
U	2.8	1.2	0.5	0.5	1.1	0.5
V	137	387	401	354	372	350
Y	55.8	41.6	30.3	34.5	24.7	28.1
Zn	126	152	111	119	109	118
Zr	431	278	117	212	119	149

	CB-PAJ-2	CB-PAJ-4	CB-PAJ-6	CB-PAJ-7	CB-PAJ-8	CB-PAJ-9
SiO_2	54.95	54.90	54.55	56.96	57.55	56.44
TiO_2	3.11	2.91	2.74	1.79	1.61	1.81
Al_2O_3	12.79	12.89	12.63	13.83	13.19	13.25
Fe_2O_3	5.39	5.30	5.04	5.06	4.79	5.07
FeO	7.24	7.15	7.24	6.90	6.40	7.00
MnO	0.19	0.23	0.19	0.17	0.17	0.18
MgO	4.53	4.24	4.04	4.32	4.23	4.26
CaO	4.02	4.55	6.45	5.23	5.57	6.36
Na_2O	3.02	2.99	3.29	3.61	2.93	3.37
K_2O	2.70	2.70	1.76	1.57	2.37	1.75
P_2O_5	0.65	0.63	0.58	0.31	0.29	0.30
Total	98.59	98.48	98.51	99.75	99.10	99.79
LOI	4.53	4.18	5.92	6.24	6.62	7.13
Ba	551	507	407	290	507	387
Ce	38	42	37	56	66	52
Co	42	41	38	45	40	44
Cr	35	39	50	28	30	26
Cu	111	135	145	100	78	102
Ga	19.0	19.3	17.6	17.0	16.1	16.0
La	19	19	20	21	27	23
Nb	42.1	40.2	35.8	32.7	33.2	30.4
Ni	33	32	67	42	38	42
Pb	10	1	5	12	1	5
Rb	37.0	35.8	25.0	23.4	30.7	25.2
Sc	26	26	28	31	29	33
Sr	244	282	238	219	170	197
Th	12.5	15.2	14.2	12.4	8.2	12.0
U	2.0	0.8	0.5	1.1	0.5	0.5
V	263	261	266	274	245	271
Y	52.6	51.6	46.2	46.6	46.8	41.7
Zn	134	137	128	130	120	124
Zr	360	350	312	274	291	255

	CB-PAJ-10	CB-PAJ-11	CB-PAJ-13	CB-PAJ-15	CB-PAJ-16	CB-PAJ-17
SiO_2	57.02	54.07	54.94	55.16	53.17	53.96
TiO_2	1.73	2.08	1.67	2.00	1.99	1.79
Al_2O_3	13.40	13.60	13.24	12.93	13.42	13.17
Fe_2O_3	4.84	5.31	5.18	6.03	5.47	5.32
FeO	6.78	7.44	7.18	7.63	7.93	7.60
MnO	0.16	0.20	0.20	0.26	0.24	0.21
MgO	4.12	5.18	4.26	3.61	5.25	5.23
CaO	5.33	5.79	6.66	5.03	5.95	6.07
Na_2O	2.68	3.99	3.47	4.97	3.96	4.26
K_2O	2.19	1.45	1.92	1.38	1.26	0.98
P_2O_5	0.32	0.31	0.30	0.40	0.37	0.29
Total	98.58	99.42	99.02	99.39	99.02	98.87
LOI	6.10	3.39	2.31	2.08	2.95	3.96
Ba	370	276	419	451	287	324
Ce	65	40	47	63	44	51
Co	44	50	45	46	50	50
Cr	42	36	45	28	46	44
Cu	103	128	95	84	96	94
Ga	17.2	16.6	14.5	17.4	15.6	16.2
La	25	17	22	23	18	18
Nb	35.8	25.0	22.0	31.8	23.4	22.2
Ni	41	43	39	28	44	41
Pb	1	1	1	18	8	50
Rb	27.8	21.6	28.6	19.4	20.3	15.3
Sc	31	35	33	31	38	35
Sr	218	280	292	256	253	207
Th	7.1	7.1	2.5	12.1	11.6	7.5
U	1.8	0.5	1.4	0.5	1.7	0.5
V	260	309	288	289	319	284
Y	48.2	41.1	40.5	47.5	40.6	42.4
Zn	110	109	105	140	215	311
Zr	293	213	206	266	191	192

Appendix C - Normative Mineralogy

Normative mineralogy was calculated from major element geochemical data determined using XRF analysis at Franklin and Marshall College. Normative mineralogy is given in weight percent norm. This was done using a CIPW norm spreadsheet provided by Dr. Matthew Brueseke. This spreadsheet converts major element oxide weight percent concentrations to normative mineralogy values, using the calculations outlined in Cross et al (1902).

	CB-PAW-1	CB-PAW-2	CB-PAW-3	CB-PAW-4	CB-PAW-5	CB-PAW-6
Q	0.00	1.17	2.09	2.17	1.23	0.00
Or	8.27	4.93	5.58	5.65	8.12	7.63
Ab	30.91	29.86	27.45	26.41	29.15	27.93
An	18.57	20.89	21.39	21.96	19.65	19.04
Lc	0.00	0.00	0.00	0.00	0.00	0.00
Ne	0.00	0.00	0.00	0.00	0.00	0.00
Di	14.17	18.37	19.45	19.60	18.95	22.28
Hy	14.20	13.19	12.56	12.79	11.54	11.02
Ol	0.94	0.00	0.00	0.00	0.00	0.67
Mt	7.29	6.64	6.63	6.62	6.60	6.78
Il	4.77	4.19	4.09	4.05	4.00	3.92
Ap	0.88	0.76	0.76	0.74	0.76	0.72

	CB-PAW-7	CB-PAW-8	CB-PAW-9	CB-PAW-10	CB-PAW-11	CB-PAW-12
Q	0.00	0.00	1.40	0.89	8.58	9.32
Or	6.11	7.01	10.95	12.91	8.05	9.73
Ab	31.25	30.89	28.80	27.61	28.26	26.24
An	18.46	18.39	17.28	16.98	16.33	16.24
Lc	0.00	0.00	0.00	0.00	0.00	0.00
Ne	0.00	0.00	0.00	0.00	0.00	0.00
Di	18.28	18.37	16.49	16.83	14.68	14.82
Hy	13.01	11.82	12.79	13.34	9.95	9.58
Ol	1.00	1.70	0.00	0.00	0.00	0.00
Mt	6.99	7.01	7.10	6.93	8.56	8.57
Il	4.19	4.10	4.24	3.76	4.38	4.33
Ap	0.71	0.71	0.95	0.74	1.22	1.17

	CB-PAW-13	CB-PAW-14	CB-PAW-15	CB-PAW-16	CB-PAW-17	CB-PAW-18
Q	9.96	8.83	10.17	12.14	7.40	14.80
Or	8.58	8.91	15.17	14.38	12.29	13.07
Ab	26.71	28.41	28.36	28.01	29.27	30.07
An	17.01	15.66	12.22	13.61	12.87	11.92
Lc	0.00	0.00	0.00	0.00	0.00	0.00
Ne	0.00	0.00	0.00	0.00	0.00	0.00
Di	13.86	14.81	11.37	7.38	11.75	8.58
Hy	9.69	9.13	8.74	11.71	11.61	9.77
Ol	0.00	0.00	0.00	0.00	0.00	0.00
Mt	8.52	8.68	8.86	8.54	8.52	7.84
Il	4.44	4.36	4.10	3.53	4.79	3.24
Ap	1.24	1.21	1.00	0.71	1.51	0.72

	CB-PAW-19	CB-PAW-20	CB-PAW-21	CB-PAN-5	CB-PAN-6	CB-PAN-7
Q	7.15	8.13	6.00	8.31	6.87	9.09
Or	10.36	9.76	6.50	7.92	9.67	10.37
Ab	30.62	29.30	37.32	23.72	25.82	28.76
An	14.99	16.12	13.11	19.14	18.00	16.05
Lc	0.00	0.00	0.00	0.00	0.00	0.00
Ne	0.00	0.00	0.00	0.00	0.00	0.00
Di	12.10	14.21	10.87	15.99	14.22	11.89
Hy	11.86	10.18	12.46	9.57	10.11	9.87
Ol	0.00	0.00	0.00	0.00	0.00	0.00
Mt	8.03	7.68	8.77	7.68	7.89	7.61
Il	4.01	3.78	4.04	6.60	6.25	5.22
Ap	0.88	0.85	0.93	1.07	1.17	1.14

	CB-PAN-8	CB-PAN-9	CB-PAN-12	CB-PAN-13	CB-PAN-14	CB-PAN-15
Q	9.27	7.58	1.84	4.27	11.28	8.26
Or	10.19	10.14	8.52	8.09	9.41	11.48
Ab	27.20	25.04	28.00	29.85	36.24	28.43
An	17.56	18.10	16.50	14.92	12.81	15.27
Lc	0.00	0.00	0.00	0.00	0.00	0.00
Ne	0.00	0.00	0.00	0.00	0.00	0.00
Di	11.67	13.23	15.57	14.44	9.14	12.01
Hy	10.62	11.28	13.09	11.07	7.76	9.19
Ol	0.00	0.00	0.00	0.00	0.00	0.00
Mt	7.36	7.65	8.35	8.59	7.40	7.90
Il	5.06	5.80	6.74	7.38	4.99	6.20
Ap	0.98	1.17	1.39	1.39	0.98	1.27

	CB-PAN-16	CB-PAN-17	CB-PAN-18	CB-PAN-19	CB-PAN-20	CB-PAN-21
Q	17.90	8.60	0.15	3.20	0.00	0.41
Or	16.66	8.96	5.49	10.65	4.49	4.13
Ab	28.98	24.62	22.98	27.25	21.61	23.57
An	12.13	17.36	24.48	17.44	26.44	25.28
Lc	0.00	0.00	0.00	0.00	0.00	0.00
Ne	0.00	0.00	0.00	0.00	0.00	0.00
Di	7.92	8.06	16.97	13.82	19.08	17.79
Hy	4.36	15.49	17.35	12.91	11.67	15.02
Ol	0.00	0.00	0.00	0.00	3.22	0.00
Mt	6.39	8.53	7.49	7.95	7.00	7.14
Il	4.16	7.09	4.33	5.72	5.57	5.70
Ap	1.50	1.29	0.76	1.08	0.91	0.96

	CB-PAJ-2	CB-PAJ-4	CB-PAJ-6	CB-PAJ-7	CB-PAJ-8	CB-PAJ-9
Q	12.33	12.07	11.31	12.04	13.77	11.23
Or	16.18	16.19	10.54	9.29	14.12	10.35
Ab	25.91	25.67	28.21	30.60	24.99	28.54
An	13.55	13.97	14.69	16.92	15.96	15.87
Lc	0.00	0.00	0.00	0.00	0.00	0.00
Ne	0.00	0.00	0.00	0.00	0.00	0.00
Di	1.93	3.89	11.41	5.79	8.20	11.31
Hy	14.65	13.32	9.79	13.87	12.20	11.21
Ol	0.00	0.00	0.00	0.00	0.00	0.00
Mt	7.92	7.79	7.40	7.34	6.99	7.35
Il	5.98	5.60	5.26	3.40	3.08	3.43
Ap	1.56	1.51	1.39	0.73	0.69	0.71

	CB-PAJ-10	CB-PAJ-11	CB-PAJ-13	CB-PAJ-15	CB-PAJ-16	CB-PAJ-17
Q	15.26	5.79	8.22	6.04	5.13	5.39
Or	13.12	8.61	11.44	8.19	7.51	5.85
Ab	22.99	33.91	29.61	42.26	33.80	36.40
An	18.31	14.98	15.00	8.94	15.25	14.05
Lc	0.00	0.00	0.00	0.00	0.00	0.00
Ne	0.00	0.00	0.00	0.00	0.00	0.00
Di	5.25	9.72	13.46	11.15	9.94	11.87
Hy	13.86	14.57	10.79	9.88	15.70	14.54
Ol	0.00	0.00	0.00	0.00	0.00	0.00
Mt	7.11	7.72	7.56	8.78	7.99	7.78
Il	3.33	3.96	3.19	3.81	3.81	3.43
Ap	0.77	0.74	0.71	0.95	0.88	0.69

Appendix D - Similarity Coefficients

Similarity coefficients were calculated, by the method of Borchardt et al (1971) and Borchardt et al (1972), to determine the statistical similarity between different samples present in the three analyzed wells in this study. In general, if samples are more than 91% similar (highlighted in yellow), the two samples are considered similar to each other. When the similar coefficients rise above 95%, the two samples are considered very similar to each other. Similarity coefficients are calculated by determining how similar each individual major and trace element concentration are for the two samples. These similarities were then averaged together to determine the final similarity coefficient of the two selected samples.

	CB-PAW-1	CB-PAW-2	CB-PAW-3	CB-PAW-4	CB-PAW-5	CB-PAW-6
CB-PAW-1	-	0.891	0.888	0.877	0.913	0.886
CB-PAW-2	0.891	-	0.954	0.947	0.918	0.903
CB-PAW-3	0.888	0.954	-	0.974	0.927	0.933
CB-PAW-4	0.877	0.947	0.974	-	0.921	0.936
CB-PAW-5	0.913	0.918	0.927	0.921	-	0.941
CB-PAW-6	0.886	0.903	0.933	0.936	0.941	-
CB-PAW-7	0.904	0.931	0.950	0.946	0.929	0.940
CB-PAW-8	0.905	0.930	0.932	0.933	0.946	0.937
CB-PAW-9	0.874	0.820	0.841	0.839	0.880	0.864
CB-PAW-10	0.885	0.849	0.869	0.877	0.908	0.909
CB-PAW-11	0.792	0.730	0.750	0.742	0.775	0.765
CB-PAW-12	0.784	0.715	0.736	0.729	0.765	0.755
CB-PAW-13	0.785	0.708	0.728	0.722	0.758	0.746
CB-PAW-14	0.789	0.715	0.734	0.724	0.766	0.753
CB-PAW-15	0.719	0.667	0.684	0.674	0.709	0.708
CB-PAW-16	0.656	0.616	0.633	0.628	0.658	0.663
CB-PAW-17	0.735	0.669	0.683	0.675	0.710	0.707
CB-PAW-18	0.675	0.630	0.643	0.637	0.675	0.675
CB-PAW-19	0.805	0.740	0.756	0.749	0.790	0.787
CB-PAW-20	0.800	0.735	0.753	0.745	0.792	0.789
CB-PAW-21	0.763	0.729	0.746	0.740	0.751	0.767
CB-PAN-5	0.818	0.770	0.786	0.776	0.808	0.793
CB-PAN-6	0.827	0.765	0.778	0.769	0.797	0.784
CB-PAN-7	0.801	0.736	0.758	0.748	0.788	0.774
CB-PAN-8	0.822	0.761	0.785	0.779	0.809	0.807
CB-PAN-9	0.846	0.789	0.801	0.792	0.819	0.803
CB-PAN-12	0.856	0.806	0.803	0.800	0.829	0.810
CB-PAN-13	0.803	0.758	0.755	0.753	0.792	0.766
CB-PAN-14	0.758	0.681	0.697	0.689	0.733	0.728
CB-PAN-15	0.784	0.732	0.742	0.732	0.761	0.751
CB-PAN-16	0.584	0.549	0.562	0.551	0.583	0.563
CB-PAN-17	0.793	0.729	0.742	0.740	0.759	0.757
CB-PAN-18	0.847	0.897	0.890	0.894	0.866	0.871
CB-PAN-19	0.866	0.812	0.826	0.823	0.834	0.832
CB-PAN-20	0.838	0.867	0.846	0.844	0.830	0.815
CB-PAN-21	0.887	0.894	0.891	0.883	0.861	0.859
CB-PAJ-2	0.694	0.636	0.657	0.651	0.681	0.681
CB-PAJ-4	0.695	0.650	0.668	0.663	0.685	0.692
CB-PAJ-6	0.775	0.715	0.729	0.720	0.752	0.754
CB-PAJ-7	0.763	0.718	0.733	0.726	0.757	0.765
CB-PAJ-8	0.694	0.653	0.671	0.667	0.699	0.700
CB-PAJ-9	0.773	0.716	0.733	0.726	0.773	0.770
CB-PAJ-10	0.722	0.682	0.703	0.698	0.735	0.733
CB-PAJ-11	0.822	0.793	0.813	0.809	0.828	0.844
CB-PAJ-13	0.793	0.745	0.762	0.763	0.806	0.806
CB-PAJ-15	0.725	0.672	0.689	0.681	0.728	0.725
CB-PAJ-16	0.817	0.776	0.793	0.787	0.807	0.823
CB-PAJ-17	0.768	0.757	0.776	0.772	0.776	0.795

	CB-PAW-7	CB-PAW-8	CB-PAW-9	CB-PAW-10	CB-PAW-11	CB-PAW-12
CB-PAW-1	0.904	0.905	0.874	0.885	0.792	0.784
CB-PAW-2	0.931	0.930	0.820	0.849	0.730	0.715
CB-PAW-3	0.950	0.932	0.841	0.869	0.750	0.736
CB-PAW-4	0.946	0.933	0.839	0.877	0.742	0.729
CB-PAW-5	0.929	0.946	0.880	0.908	0.775	0.765
CB-PAW-6	0.940	0.937	0.864	0.909	0.765	0.755
CB-PAW-7	-	0.962	0.858	0.885	0.763	0.744
CB-PAW-8	0.962	-	0.863	0.893	0.765	0.750
CB-PAW-9	0.858	0.863	-	0.926	0.823	0.833
CB-PAW-10	0.885	0.893	0.926	-	0.778	0.794
CB-PAW-11	0.763	0.765	0.823	0.778	-	0.942
CB-PAW-12	0.744	0.750	0.833	0.794	0.942	-
CB-PAW-13	0.739	0.744	0.818	0.779	0.949	0.967
CB-PAW-14	0.744	0.751	0.829	0.785	0.945	0.970
CB-PAW-15	0.689	0.694	0.785	0.757	0.866	0.889
CB-PAW-16	0.641	0.647	0.717	0.716	0.797	0.801
CB-PAW-17	0.696	0.698	0.796	0.761	0.887	0.873
CB-PAW-18	0.656	0.663	0.737	0.732	0.806	0.824
CB-PAW-19	0.771	0.774	0.855	0.818	0.887	0.876
CB-PAW-20	0.764	0.772	0.858	0.830	0.888	0.891
CB-PAW-21	0.760	0.749	0.782	0.740	0.876	0.856
CB-PAN-5	0.793	0.801	0.815	0.785	0.844	0.826
CB-PAN-6	0.786	0.791	0.837	0.810	0.853	0.852
CB-PAN-7	0.768	0.770	0.872	0.820	0.866	0.861
CB-PAN-8	0.796	0.798	0.877	0.841	0.853	0.860
CB-PAN-9	0.800	0.810	0.858	0.829	0.839	0.844
CB-PAN-12	0.817	0.833	0.846	0.819	0.831	0.810
CB-PAN-13	0.772	0.789	0.798	0.766	0.816	0.790
CB-PAN-14	0.714	0.718	0.803	0.759	0.829	0.838
CB-PAN-15	0.751	0.757	0.825	0.788	0.841	0.826
CB-PAN-16	0.564	0.567	0.637	0.609	0.695	0.709
CB-PAN-17	0.751	0.755	0.801	0.778	0.823	0.817
CB-PAN-18	0.884	0.881	0.796	0.819	0.716	0.703
CB-PAN-19	0.832	0.835	0.879	0.856	0.826	0.818
CB-PAN-20	0.844	0.838	0.767	0.781	0.683	0.679
CB-PAN-21	0.879	0.864	0.809	0.823	0.726	0.724
CB-PAJ-2	0.661	0.663	0.752	0.729	0.808	0.802
CB-PAJ-4	0.674	0.677	0.755	0.732	0.823	0.812
CB-PAJ-6	0.740	0.745	0.814	0.776	0.832	0.834
CB-PAJ-7	0.740	0.737	0.799	0.778	0.830	0.833
CB-PAJ-8	0.678	0.685	0.763	0.760	0.787	0.786
CB-PAJ-9	0.746	0.753	0.826	0.805	0.847	0.853
CB-PAJ-10	0.710	0.711	0.781	0.780	0.799	0.799
CB-PAJ-11	0.824	0.817	0.853	0.828	0.850	0.834
CB-PAJ-13	0.782	0.791	0.868	0.859	0.847	0.850
CB-PAJ-15	0.701	0.710	0.776	0.738	0.858	0.853
CB-PAJ-16	0.805	0.797	0.847	0.809	0.830	0.816
CB-PAJ-17	0.797	0.782	0.797	0.778	0.799	0.778

	CB-PAW-13	CB-PAW-14	CB-PAW-15	CB-PAW-16	CB-PAW-17	CB-PAW-18
CB-PAW-1	0.785	0.789	0.719	0.656	0.735	0.675
CB-PAW-2	0.708	0.715	0.667	0.616	0.669	0.630
CB-PAW-3	0.728	0.734	0.684	0.633	0.683	0.643
CB-PAW-4	0.722	0.724	0.674	0.628	0.675	0.637
CB-PAW-5	0.758	0.766	0.709	0.658	0.710	0.675
CB-PAW-6	0.746	0.753	0.708	0.663	0.707	0.675
CB-PAW-7	0.739	0.744	0.689	0.641	0.696	0.656
CB-PAW-8	0.744	0.751	0.694	0.647	0.698	0.663
CB-PAW-9	0.818	0.829	0.785	0.717	0.796	0.737
CB-PAW-10	0.779	0.785	0.757	0.716	0.761	0.732
CB-PAW-11	0.949	0.945	0.866	0.797	0.887	0.806
CB-PAW-12	0.967	0.970	0.889	0.801	0.873	0.824
CB-PAW-13	-	0.975	0.891	0.801	0.877	0.823
CB-PAW-14	0.975	-	0.900	0.805	0.876	0.831
CB-PAW-15	0.891	0.900	-	0.861	0.865	0.879
CB-PAW-16	0.801	0.805	0.861	-	0.849	0.925
CB-PAW-17	0.877	0.876	0.865	0.849	-	0.852
CB-PAW-18	0.823	0.831	0.879	0.925	0.852	-
CB-PAW-19	0.873	0.875	0.858	0.796	0.879	0.819
CB-PAW-20	0.889	0.896	0.855	0.800	0.868	0.826
CB-PAW-21	0.865	0.867	0.854	0.798	0.864	0.809
CB-PAN-5	0.827	0.826	0.770	0.707	0.779	0.717
CB-PAN-6	0.838	0.837	0.782	0.721	0.799	0.740
CB-PAN-7	0.848	0.851	0.818	0.764	0.844	0.794
CB-PAN-8	0.848	0.847	0.808	0.747	0.819	0.776
CB-PAN-9	0.829	0.828	0.778	0.714	0.790	0.732
CB-PAN-12	0.814	0.815	0.732	0.666	0.766	0.679
CB-PAN-13	0.799	0.797	0.732	0.684	0.771	0.698
CB-PAN-14	0.839	0.848	0.836	0.794	0.819	0.823
CB-PAN-15	0.823	0.824	0.799	0.754	0.816	0.782
CB-PAN-16	0.714	0.712	0.764	0.757	0.709	0.752
CB-PAN-17	0.824	0.816	0.760	0.709	0.796	0.719
CB-PAN-18	0.697	0.698	0.646	0.602	0.651	0.612
CB-PAN-19	0.806	0.807	0.771	0.712	0.788	0.723
CB-PAN-20	0.674	0.674	0.628	0.586	0.643	0.589
CB-PAN-21	0.718	0.717	0.670	0.608	0.672	0.619
CB-PAJ-2	0.798	0.795	0.823	0.818	0.845	0.820
CB-PAJ-4	0.809	0.805	0.823	0.814	0.845	0.820
CB-PAJ-6	0.830	0.838	0.808	0.767	0.841	0.786
CB-PAJ-7	0.835	0.849	0.844	0.834	0.846	0.865
CB-PAJ-8	0.781	0.786	0.831	0.866	0.841	0.887
CB-PAJ-9	0.854	0.866	0.860	0.837	0.862	0.859
CB-PAJ-10	0.793	0.799	0.841	0.861	0.821	0.888
CB-PAJ-11	0.832	0.839	0.802	0.747	0.811	0.764
CB-PAJ-13	0.839	0.851	0.829	0.792	0.842	0.820
CB-PAJ-15	0.856	0.866	0.870	0.850	0.867	0.863
CB-PAJ-16	0.813	0.818	0.784	0.756	0.823	0.760
CB-PAJ-17	0.787	0.787	0.767	0.762	0.804	0.768

	CB-PAW-19	CB-PAW-20	CB-PAW-21	CB-PAN-5	CB-PAN-6	CB-PAN-7
CB-PAW-1	0.805	0.800	0.763	0.818	0.827	0.801
CB-PAW-2	0.740	0.735	0.729	0.770	0.765	0.736
CB-PAW-3	0.756	0.753	0.746	0.786	0.778	0.758
CB-PAW-4	0.749	0.745	0.740	0.776	0.769	0.748
CB-PAW-5	0.790	0.792	0.751	0.808	0.797	0.788
CB-PAW-6	0.787	0.789	0.767	0.793	0.784	0.774
CB-PAW-7	0.771	0.764	0.760	0.793	0.786	0.768
CB-PAW-8	0.774	0.772	0.749	0.801	0.791	0.770
CB-PAW-9	0.855	0.858	0.782	0.815	0.837	0.872
CB-PAW-10	0.818	0.830	0.740	0.785	0.810	0.820
CB-PAW-11	0.887	0.888	0.876	0.844	0.853	0.866
CB-PAW-12	0.876	0.891	0.856	0.826	0.852	0.861
CB-PAW-13	0.873	0.889	0.865	0.827	0.838	0.848
CB-PAW-14	0.875	0.896	0.867	0.826	0.837	0.851
CB-PAW-15	0.858	0.855	0.854	0.770	0.782	0.818
CB-PAW-16	0.796	0.800	0.798	0.707	0.721	0.764
CB-PAW-17	0.879	0.868	0.864	0.779	0.799	0.844
CB-PAW-18	0.819	0.826	0.809	0.717	0.740	0.794
CB-PAW-19	-	0.953	0.883	0.809	0.841	0.881
CB-PAW-20	0.953	-	0.874	0.822	0.859	0.881
CB-PAW-21	0.883	0.874	-	0.809	0.793	0.811
CB-PAN-5	0.809	0.822	0.809	-	0.929	0.830
CB-PAN-6	0.841	0.859	0.793	0.929	-	0.881
CB-PAN-7	0.881	0.881	0.811	0.830	0.881	-
CB-PAN-8	0.879	0.886	0.817	0.833	0.883	0.947
CB-PAN-9	0.840	0.844	0.779	0.870	0.922	0.902
CB-PAN-12	0.810	0.806	0.770	0.884	0.889	0.832
CB-PAN-13	0.807	0.805	0.783	0.878	0.868	0.841
CB-PAN-14	0.867	0.883	0.839	0.792	0.826	0.877
CB-PAN-15	0.848	0.844	0.779	0.840	0.895	0.916
CB-PAN-16	0.664	0.669	0.656	0.621	0.645	0.697
CB-PAN-17	0.840	0.833	0.795	0.876	0.893	0.847
CB-PAN-18	0.723	0.720	0.719	0.782	0.764	0.728
CB-PAN-19	0.836	0.821	0.768	0.859	0.898	0.875
CB-PAN-20	0.691	0.687	0.672	0.767	0.734	0.695
CB-PAN-21	0.730	0.727	0.717	0.802	0.788	0.742
CB-PAJ-2	0.812	0.808	0.776	0.775	0.805	0.840
CB-PAJ-4	0.821	0.826	0.789	0.789	0.822	0.857
CB-PAJ-6	0.856	0.865	0.808	0.793	0.838	0.894
CB-PAJ-7	0.877	0.889	0.874	0.776	0.801	0.833
CB-PAJ-8	0.825	0.833	0.790	0.737	0.772	0.816
CB-PAJ-9	0.899	0.911	0.862	0.788	0.816	0.855
CB-PAJ-10	0.859	0.864	0.808	0.759	0.794	0.823
CB-PAJ-11	0.881	0.875	0.882	0.819	0.826	0.840
CB-PAJ-13	0.908	0.927	0.827	0.798	0.838	0.855
CB-PAJ-15	0.851	0.863	0.898	0.797	0.785	0.810
CB-PAJ-16	0.882	0.874	0.878	0.795	0.794	0.810
CB-PAJ-17	0.854	0.847	0.850	0.760	0.758	0.774

	CB-PAN-8	CB-PAN-9	CB-PAN-12	CB-PAN-13	CB-PAN-14	CB-PAN-15
CB-PAW-1	0.822	0.846	0.856	0.803	0.758	0.784
CB-PAW-2	0.761	0.789	0.806	0.758	0.681	0.732
CB-PAW-3	0.785	0.801	0.803	0.755	0.697	0.742
CB-PAW-4	0.779	0.792	0.800	0.753	0.689	0.732
CB-PAW-5	0.809	0.819	0.829	0.792	0.733	0.761
CB-PAW-6	0.807	0.803	0.810	0.766	0.728	0.751
CB-PAW-7	0.796	0.800	0.817	0.772	0.714	0.751
CB-PAW-8	0.798	0.810	0.833	0.789	0.718	0.757
CB-PAW-9	0.877	0.858	0.846	0.798	0.803	0.825
CB-PAW-10	0.841	0.829	0.819	0.766	0.759	0.788
CB-PAW-11	0.853	0.839	0.831	0.816	0.829	0.841
CB-PAW-12	0.860	0.844	0.810	0.790	0.838	0.826
CB-PAW-13	0.848	0.829	0.814	0.799	0.839	0.823
CB-PAW-14	0.847	0.828	0.815	0.797	0.848	0.824
CB-PAW-15	0.808	0.778	0.732	0.732	0.836	0.799
CB-PAW-16	0.747	0.714	0.666	0.684	0.794	0.754
CB-PAW-17	0.819	0.790	0.766	0.771	0.819	0.816
CB-PAW-18	0.776	0.732	0.679	0.698	0.823	0.782
CB-PAW-19	0.879	0.840	0.810	0.807	0.867	0.848
CB-PAW-20	0.886	0.844	0.806	0.805	0.883	0.844
CB-PAW-21	0.817	0.779	0.770	0.783	0.839	0.779
CB-PAN-5	0.833	0.870	0.884	0.878	0.792	0.840
CB-PAN-6	0.883	0.922	0.889	0.868	0.826	0.895
CB-PAN-7	0.947	0.902	0.832	0.841	0.877	0.916
CB-PAN-8	-	0.917	0.845	0.835	0.877	0.904
CB-PAN-9	0.917	-	0.885	0.871	0.809	0.899
CB-PAN-12	0.845	0.885	-	0.912	0.759	0.851
CB-PAN-13	0.835	0.871	0.912	-	0.772	0.856
CB-PAN-14	0.877	0.809	0.759	0.772	-	0.841
CB-PAN-15	0.904	0.899	0.851	0.856	0.841	-
CB-PAN-16	0.672	0.643	0.604	0.616	0.712	0.688
CB-PAN-17	0.854	0.892	0.893	0.910	0.796	0.863
CB-PAN-18	0.750	0.768	0.815	0.762	0.672	0.727
CB-PAN-19	0.881	0.923	0.893	0.843	0.775	0.871
CB-PAN-20	0.716	0.751	0.788	0.735	0.649	0.690
CB-PAN-21	0.764	0.800	0.816	0.764	0.689	0.740
CB-PAJ-2	0.819	0.789	0.735	0.745	0.845	0.832
CB-PAJ-4	0.840	0.804	0.747	0.757	0.858	0.849
CB-PAJ-6	0.894	0.847	0.809	0.810	0.893	0.870
CB-PAJ-7	0.837	0.790	0.753	0.767	0.864	0.791
CB-PAJ-8	0.804	0.762	0.697	0.708	0.830	0.790
CB-PAJ-9	0.857	0.810	0.772	0.775	0.859	0.812
CB-PAJ-10	0.823	0.778	0.722	0.733	0.850	0.803
CB-PAJ-11	0.845	0.818	0.816	0.795	0.831	0.793
CB-PAJ-13	0.854	0.818	0.776	0.767	0.842	0.820
CB-PAJ-15	0.810	0.769	0.737	0.766	0.865	0.782
CB-PAJ-16	0.813	0.786	0.794	0.780	0.816	0.763
CB-PAJ-17	0.773	0.743	0.744	0.738	0.785	0.734

	CB-PAN-16	CB-PAN-17	CB-PAN-18	CB-PAN-19	CB-PAN-20	CB-PAN-21
CB-PAW-1	0.584	0.793	0.847	0.866	0.838	0.887
CB-PAW-2	0.549	0.729	0.897	0.812	0.867	0.894
CB-PAW-3	0.562	0.742	0.890	0.826	0.846	0.891
CB-PAW-4	0.551	0.740	0.894	0.823	0.844	0.883
CB-PAW-5	0.583	0.759	0.866	0.834	0.830	0.861
CB-PAW-6	0.563	0.757	0.871	0.832	0.815	0.859
CB-PAW-7	0.564	0.751	0.884	0.832	0.844	0.879
CB-PAW-8	0.567	0.755	0.881	0.835	0.838	0.864
CB-PAW-9	0.637	0.801	0.796	0.879	0.767	0.809
CB-PAW-10	0.609	0.778	0.819	0.856	0.781	0.823
CB-PAW-11	0.695	0.823	0.716	0.826	0.683	0.726
CB-PAW-12	0.709	0.817	0.703	0.818	0.679	0.724
CB-PAW-13	0.714	0.824	0.697	0.806	0.674	0.718
CB-PAW-14	0.712	0.816	0.698	0.807	0.674	0.717
CB-PAW-15	0.764	0.760	0.646	0.771	0.628	0.670
CB-PAW-16	0.757	0.709	0.602	0.712	0.586	0.608
CB-PAW-17	0.709	0.796	0.651	0.788	0.643	0.672
CB-PAW-18	0.752	0.719	0.612	0.723	0.589	0.619
CB-PAW-19	0.664	0.840	0.723	0.836	0.691	0.730
CB-PAW-20	0.669	0.833	0.720	0.821	0.687	0.727
CB-PAW-21	0.656	0.795	0.719	0.768	0.672	0.717
CB-PAN-5	0.621	0.876	0.782	0.859	0.767	0.802
CB-PAN-6	0.645	0.893	0.764	0.898	0.734	0.788
CB-PAN-7	0.697	0.847	0.728	0.875	0.695	0.742
CB-PAN-8	0.672	0.854	0.750	0.881	0.716	0.764
CB-PAN-9	0.643	0.892	0.768	0.923	0.751	0.800
CB-PAN-12	0.604	0.893	0.815	0.893	0.788	0.816
CB-PAN-13	0.616	0.910	0.762	0.843	0.735	0.764
CB-PAN-14	0.712	0.796	0.672	0.775	0.649	0.689
CB-PAN-15	0.688	0.863	0.727	0.871	0.690	0.740
CB-PAN-16	-	0.621	0.528	0.636	0.516	0.542
CB-PAN-17	0.621	-	0.742	0.855	0.720	0.758
CB-PAN-18	0.528	0.742	-	0.794	0.876	0.871
CB-PAN-19	0.636	0.855	0.794	-	0.764	0.822
CB-PAN-20	0.516	0.720	0.876	0.764	-	0.917
CB-PAN-21	0.542	0.758	0.871	0.822	0.917	-
CB-PAJ-2	0.749	0.772	0.632	0.776	0.616	0.661
CB-PAJ-4	0.755	0.786	0.647	0.785	0.620	0.662
CB-PAJ-6	0.693	0.821	0.702	0.810	0.673	0.716
CB-PAJ-7	0.687	0.773	0.703	0.756	0.659	0.699
CB-PAJ-8	0.730	0.737	0.642	0.737	0.623	0.646
CB-PAJ-9	0.682	0.786	0.698	0.783	0.663	0.700
CB-PAJ-10	0.714	0.758	0.685	0.757	0.657	0.686
CB-PAJ-11	0.628	0.811	0.776	0.827	0.711	0.752
CB-PAJ-13	0.656	0.791	0.719	0.812	0.689	0.719
CB-PAJ-15	0.705	0.768	0.660	0.738	0.647	0.675
CB-PAJ-16	0.606	0.794	0.755	0.794	0.716	0.756
CB-PAJ-17	0.590	0.755	0.738	0.749	0.703	0.739

	CB-PAJ-2	CB-PAJ-4	CB-PAJ-6	CB-PAJ-7	CB-PAJ-8	CB-PAJ-9
CB-PAW-1	0.694	0.695	0.775	0.763	0.694	0.773
CB-PAW-2	0.636	0.650	0.715	0.718	0.653	0.716
CB-PAW-3	0.657	0.668	0.729	0.733	0.671	0.733
CB-PAW-4	0.651	0.663	0.720	0.726	0.667	0.726
CB-PAW-5	0.681	0.685	0.752	0.757	0.699	0.773
CB-PAW-6	0.681	0.692	0.754	0.765	0.700	0.770
CB-PAW-7	0.661	0.674	0.740	0.740	0.678	0.746
CB-PAW-8	0.663	0.677	0.745	0.737	0.685	0.753
CB-PAW-9	0.752	0.755	0.814	0.799	0.763	0.826
CB-PAW-10	0.729	0.732	0.776	0.778	0.760	0.805
CB-PAW-11	0.808	0.823	0.832	0.830	0.787	0.847
CB-PAW-12	0.802	0.812	0.834	0.833	0.786	0.853
CB-PAW-13	0.798	0.809	0.830	0.835	0.781	0.854
CB-PAW-14	0.795	0.805	0.838	0.849	0.786	0.866
CB-PAW-15	0.823	0.823	0.808	0.844	0.831	0.860
CB-PAW-16	0.818	0.814	0.767	0.834	0.866	0.837
CB-PAW-17	0.845	0.845	0.841	0.846	0.841	0.862
CB-PAW-18	0.820	0.820	0.786	0.865	0.887	0.859
CB-PAW-19	0.812	0.821	0.856	0.877	0.825	0.899
CB-PAW-20	0.808	0.826	0.865	0.889	0.833	0.911
CB-PAW-21	0.776	0.789	0.808	0.874	0.790	0.862
CB-PAN-5	0.775	0.789	0.793	0.776	0.737	0.788
CB-PAN-6	0.805	0.822	0.838	0.801	0.772	0.816
CB-PAN-7	0.840	0.857	0.894	0.833	0.816	0.855
CB-PAN-8	0.819	0.840	0.894	0.837	0.804	0.857
CB-PAN-9	0.789	0.804	0.847	0.790	0.762	0.810
CB-PAN-12	0.735	0.747	0.809	0.753	0.697	0.772
CB-PAN-13	0.745	0.757	0.810	0.767	0.708	0.775
CB-PAN-14	0.845	0.858	0.893	0.864	0.830	0.859
CB-PAN-15	0.832	0.849	0.870	0.791	0.790	0.812
CB-PAN-16	0.749	0.755	0.693	0.687	0.730	0.682
CB-PAN-17	0.772	0.786	0.821	0.773	0.737	0.786
CB-PAN-18	0.632	0.647	0.702	0.703	0.642	0.698
CB-PAN-19	0.776	0.785	0.810	0.756	0.737	0.783
CB-PAN-20	0.616	0.620	0.673	0.659	0.623	0.663
CB-PAN-21	0.661	0.662	0.716	0.699	0.646	0.700
CB-PAJ-2	-	0.955	0.854	0.807	0.818	0.798
CB-PAJ-4	0.955	-	0.869	0.805	0.824	0.798
CB-PAJ-6	0.854	0.869	-	0.845	0.811	0.854
CB-PAJ-7	0.807	0.805	0.845	-	0.879	0.937
CB-PAJ-8	0.818	0.824	0.811	0.879	-	0.889
CB-PAJ-9	0.798	0.798	0.854	0.937	0.889	-
CB-PAJ-10	0.831	0.837	0.839	0.902	0.909	0.894
CB-PAJ-11	0.777	0.789	0.815	0.878	0.789	0.864
CB-PAJ-13	0.785	0.801	0.829	0.870	0.850	0.906
CB-PAJ-15	0.797	0.804	0.809	0.888	0.843	0.865
CB-PAJ-16	0.750	0.755	0.793	0.850	0.761	0.838
CB-PAJ-17	0.728	0.731	0.765	0.847	0.780	0.850

	CB-PAJ-10	CB-PAJ-11	CB-PAJ-13	CB-PAJ-15	CB-PAJ-16	CB-PAJ-17
CB-PAW-1	0.722	0.822	0.793	0.725	0.817	0.768
CB-PAW-2	0.682	0.793	0.745	0.672	0.776	0.757
CB-PAW-3	0.703	0.813	0.762	0.689	0.793	0.776
CB-PAW-4	0.698	0.809	0.763	0.681	0.787	0.772
CB-PAW-5	0.735	0.828	0.806	0.728	0.807	0.776
CB-PAW-6	0.733	0.844	0.806	0.725	0.823	0.795
CB-PAW-7	0.710	0.824	0.782	0.701	0.805	0.797
CB-PAW-8	0.711	0.817	0.791	0.710	0.797	0.782
CB-PAW-9	0.781	0.853	0.868	0.776	0.847	0.797
CB-PAW-10	0.780	0.828	0.859	0.738	0.809	0.778
CB-PAW-11	0.799	0.850	0.847	0.858	0.830	0.799
CB-PAW-12	0.799	0.834	0.850	0.853	0.816	0.778
CB-PAW-13	0.793	0.832	0.839	0.856	0.813	0.787
CB-PAW-14	0.799	0.839	0.851	0.866	0.818	0.787
CB-PAW-15	0.841	0.802	0.829	0.870	0.784	0.767
CB-PAW-16	0.861	0.747	0.792	0.850	0.756	0.762
CB-PAW-17	0.821	0.811	0.842	0.867	0.823	0.804
CB-PAW-18	0.888	0.764	0.820	0.863	0.760	0.768
CB-PAW-19	0.859	0.881	0.908	0.851	0.882	0.854
CB-PAW-20	0.864	0.875	0.927	0.863	0.874	0.847
CB-PAW-21	0.808	0.882	0.827	0.898	0.878	0.850
CB-PAN-5	0.759	0.819	0.798	0.797	0.795	0.760
CB-PAN-6	0.794	0.826	0.838	0.785	0.794	0.758
CB-PAN-7	0.823	0.840	0.855	0.810	0.810	0.774
CB-PAN-8	0.823	0.845	0.854	0.810	0.813	0.773
CB-PAN-9	0.778	0.818	0.818	0.769	0.786	0.743
CB-PAN-12	0.722	0.816	0.776	0.737	0.794	0.744
CB-PAN-13	0.733	0.795	0.767	0.766	0.780	0.738
CB-PAN-14	0.850	0.831	0.842	0.865	0.816	0.785
CB-PAN-15	0.803	0.793	0.820	0.782	0.763	0.734
CB-PAN-16	0.714	0.628	0.656	0.705	0.606	0.590
CB-PAN-17	0.758	0.811	0.791	0.768	0.794	0.755
CB-PAN-18	0.685	0.776	0.719	0.660	0.755	0.738
CB-PAN-19	0.757	0.827	0.812	0.738	0.794	0.749
CB-PAN-20	0.657	0.711	0.689	0.647	0.716	0.703
CB-PAN-21	0.686	0.752	0.719	0.675	0.756	0.739
CB-PAJ-2	0.831	0.777	0.785	0.797	0.750	0.728
CB-PAJ-4	0.837	0.789	0.801	0.804	0.755	0.731
CB-PAJ-6	0.839	0.815	0.829	0.809	0.793	0.765
CB-PAJ-7	0.902	0.878	0.870	0.888	0.850	0.847
CB-PAJ-8	0.909	0.789	0.850	0.843	0.761	0.780
CB-PAJ-9	0.894	0.864	0.906	0.865	0.838	0.850
CB-PAJ-10	-	0.822	0.871	0.842	0.796	0.808
CB-PAJ-11	0.822	-	0.876	0.827	0.915	0.874
CB-PAJ-13	0.871	0.876	-	0.827	0.865	0.861
CB-PAJ-15	0.842	0.827	0.827	-	0.827	0.806
CB-PAJ-16	0.796	0.915	0.865	0.827	-	0.914
CB-PAJ-17	0.808	0.874	0.861	0.806	0.914	-

Appendix E - Alteration Filter

Samples from the Arbuckle Mountains exhibit some low-grade metamorphism, although many of the cuttings still exhibit primary mineral compositions and textures. Due to this, the samples were run though the "alteration filter" of Beswick and Soucie (1978). Figure 27 shows the diagrams used for the "alteration filter." These diagrams plot the molecular proportions of major element ratios on a logarithmic scale. Once plotted, unaltered samples display a linear array. Any variation from this linear array on multiple diagrams is indicative of significant alteration and those samples were removed from the final interpretations presented in this research.

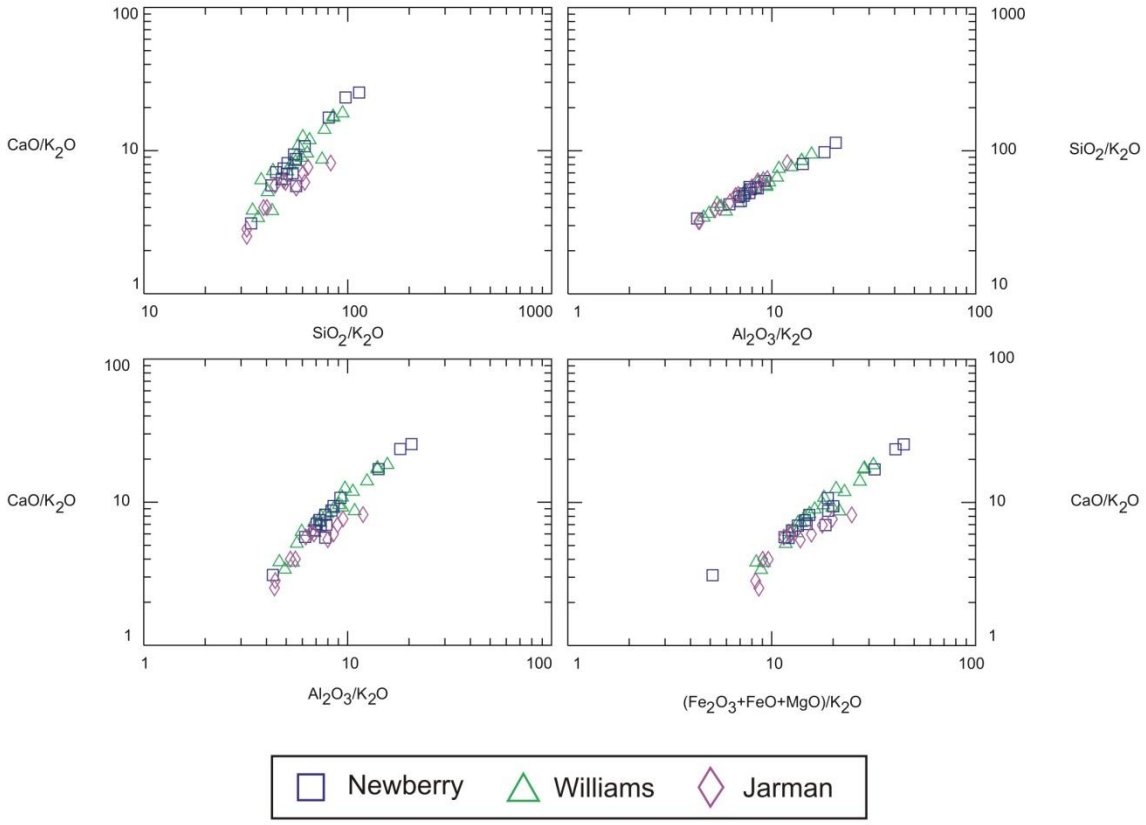

Figure 27: "Alteration filter" of Beswick and Soucie (1978) diagrams plotting molecular proportions of major and trace element ratios.